



## **Deliverable 7.5: Technical report on effect of temperature on far field properties**

Work Package 7

The project leading to this application has received funding from the European Union's Horizon 2020 research and innovation programme under grant agreement No 847593.



Document information

Project Acronym	<b>EURAD</b>
Project Title	<b>European Joint Programme on Radioactive Waste Management</b>
Project Type	<b>European Joint Programme (EJP)</b>
EC grant agreement No.	<b>847593</b>
Project starting / end date	<b>1<sup>st</sup> June 2019 – 30 May 2024</b>
Work Package No.	<b>7</b>
Work Package Title	<b>Influence of temperature on clay-based material behaviour</b>
Work Package Acronym	<b>HITEC</b>
Deliverable No.	<b>7.5</b>
Deliverable Title	<b>Technical report on effect of temperature on far field properties</b>
Lead Beneficiary	[CNRS (ULorraine)]
Contractual Delivery Date	<b>October 2023</b>
Actual Delivery Date	<b>May 2024</b>
Type	<b>Final report of WP7 Task 2.2</b>
Dissemination level	<b>Public</b>
Authors	Dragan GRGIC [CNRS (ULorraine)], Christophe IMBERT [CEA], Jon HARRINGTON [UKRI-BGS], Elena TAMAYO-MAS [UKRI-BGS]

To be cited as

Grgic, D., Imbert, C., Harrington, J. & Tamayo-Mas, E., 2023. Technical report on thermal effects on near field properties. Final version as of 01.11.2023 of deliverable D7.5 of the HORIZON 2020 project EURAD. EC Grant agreement no: 847593.

Disclaimer

All information in this document is provided "as is" and no guarantee or warranty is given that the information is fit for any particular purpose. The user, therefore, uses the information at its sole risk and liability. For the avoidance of all doubts, the European Commission has no liability in respect of this document, which is merely representing the authors' view.

Acknowledgement

This document is a deliverable of the European Joint Programme on Radioactive Waste Management (EURAD). EURAD has received funding from the European Union's Horizon 2020 research and innovation programme under grant agreement No 847593.

Status of deliverable		
	By	Date
Delivered (Lead Beneficiary)	Dragan Grgic [CNRS (ULorraine)]	1/11/2023
Verified (WP Leader)	Markus Olin [VTT]	15/05/2024
Reviewed (Reviewers)	Robert Charlier [ULiege]	3/04/2024
Approved (PMO)	Bharti Reddy	23/05/2024
Submitted to EC (Coordinator)	Andra (Coordinator)	23/05/2024

## Authors

Organisation	Name	E-mail
[CNRS (ULorraine)]	Dragan Grgic	dragan.grgic@univ-lorraine.fr
[CEA]	Christophe Imbert	christophe.imbert@cea.fr
[UKRI-BGS]	Jon Harrington and Elena Tamayo-Mas	jfha@bgs.ac.uk elena@bgs.ac.uk

## Table of content

Executive Summary.....	6
List of Figures .....	8
List of Tables .....	13
Glossary.....	16
1. Introduction .....	17
2. CNRS (ULorraine) .....	21
2.1 Introduction.....	21
2.2 Material and methods.....	21
2.2.1 Material and sampling.....	21
2.2.1.1 Description of the COx claystone.....	21
2.2.1.1 Sampling .....	22
2.2.2 Experimental device and procedures .....	25
2.2.2.1 Experimental device .....	25
2.2.2.1 Experimental procedures .....	26
2.2.3 Research plan.....	28
2.3 Results and discussion .....	30
2.3.1 Experimental results .....	30
2.3.1.1 Short-term compression tests .....	30
2.3.1.2 Long-term triaxial compression tests (multi-step creep tests) .....	37
2.3.2 Discussion.....	40
2.3.2.1 Influence of temperature (until 100 °C) on the mechanical behaviour of the COx claystone .....	40
2.3.2.2 Impact of water content decrease at very high temperature (150 °C) .....	43
2.3.2.3 Influence of the thermal loading path.....	44
2.4 Conclusion.....	45
3. CEA .....	48
3.1 Introduction.....	48
3.2 Material and methods.....	48
3.2.1 Material and sampling.....	48
3.2.2 Experimental devices and procedures.....	48
3.2.3 Research plan.....	50
3.3 Results and discussion .....	51
3.3.1 Creep tests realised with Boom Clay.....	51
3.3.1.1 Creep test at 40°C.....	51
3.3.1.1 Creep test at 60°C.....	54



3.3.1.1	Creep test at 80°C.....	56
3.3.2	Creep tests realised with Opalinus Clay .....	58
3.3.2.1	Creep test at 40°C.....	58
3.3.2.1	Creep test at 80°C.....	61
3.3.2.1	Comparison .....	64
3.4	Conclusion.....	64
4.	UKRI- BGS .....	66
4.1	Introduction.....	66
4.2	Material and methods.....	66
4.2.1	Experimental devices and procedures.....	66
4.2.2	Permeants.....	69
4.2.3	Material and sampling.....	70
4.3	Results and discussion .....	71
4.3.1	Test FPR-20-013 (COx taken from core barrel EST 60812, parallel to bedding) .....	72
4.3.2	Test FPR-21-017 (Boom Clay, taken from core 2.3 76/77D, perpendicular to bedding) .....	76
4.3.3	Test FPR-21-024 (OPA perpendicular to bedding) .....	76
4.3.4	Test FPR-21-026 (OPA taken from core barrel BH4 (4.1), parallel to bedding).....	77
4.3.5	Test FPR-21-027 (OPA taken from core barrel BF1-4 (4.3), parallel to bedding).....	77
4.3.6	Test FPR-21-051 (OPA taken from core barrel BF1-4 (5.7), parallel to bedding).....	80
4.3.7	Test FPR-21-052 (OPA taken from core barrel BF1-4 (5.8), parallel to bedding).....	84
4.3.8	Test FPR-22-025 (OPA taken from core barrel BF1-3 (8.4), perpendicular to bedding).....	90
4.3.9	Test FPR-22-067 (OPA taken from core barrel BF1-3 (4.3), perpendicular to bedding).....	95
4.3.10	Test FPR-22-098 (OPA taken from core barrel BF1-3 (4.3), perpendicular to bedding).....	97
4.4	Conclusion.....	101
4.4.1	New knowledge acquired.....	101
4.4.2	Impact of acquired knowledge .....	103
4.4.3	Remaining knowledge gaps.....	103
4.4.4	Recommendations for the future .....	103
4.5	Appendix .....	104
4.5.1	Drainage system’s influence on the thermally induced pressure response .....	104
4.5.2	Drainage system’s influence on the thermally induced pressure response .....	108
5.	General conclusions .....	110
	Acknowledgements .....	111
	References .....	111

## Executive Summary

The overall aim of the work package EURAD-WP7 HITEC (“Influence of temperature on clay-based material behaviour”) of the European Joint Programme on Radioactive Waste Management (EURAD) is to improve the Thermo-Hydro-Mechanical (THM) description of the clay-based materials – host clay rock and bentonite buffer - at elevated temperatures. Within this WP, Task 2 is focussing on the behaviour of the clay host rocks at temperatures of up to 120°C to help to optimise the repository design. Indeed, the heat generated by waste must not affect the favourable properties of the host rock, especially its transport properties, for containment. The overpressure generated by the difference between the thermal expansion coefficient of pore water and the solid rock skeleton may have deleterious consequences. In the near field (i.e., in the vicinity of the canister) characterised by a fractured zone, this could induce fracture opening or propagation in this fractured zone, altering the permeability. In far field, this could induce rock damage and reactivate fractures/faults. Laboratory experiments in subtask 2.2 were performed to provide answers about the impact of temperature on the short- and long-term (i.e., creep) mechanical properties of clay host rocks in the far-field. In addition, the magnitude and impact of thermally induced porewater pressures on the evolution of damage and intrinsic permeability in candidate clay host rocks was examined experimentally. Different testing cells (triaxial, oedometric) have been used by the different partners to achieve these goals. The materials used in this study were: Callovo Oxfordian claystone (COx), Opalinus clay (OPA) and Boom clay.

CNRS (ULorraine) analysed the effect of temperature on the mechanical behaviour of the Callovo-Oxfordian claystone in the context of deep geological disposal of radioactive waste in France. First, compression tests in a triaxial cell were performed under pseudo-drained condition with strains measurements, at different temperatures (20, 40, 60, 80, 100 and 150 °C), confining pressures (0, 4 and 12 MPa) and samples orientations (parallel and perpendicular to the bedding plane) to characterize the short-term mechanical behaviour. Second, multi-step creep tests in a triaxial cell with axial and lateral strains measurements were carried out at different temperatures (20, 40, 60, and 80 °C), for different confining pressures (2 and 12 MPa) and orientations (loading direction parallel and perpendicular to the bedding plane) to characterize the long-term mechanical behaviour. From the short-term compression tests, the analysis of elastic coefficients indicates that in all cases an anisotropic damage develops during the deviatoric loading due to the opening of axial microcracks. In addition, the peak deformation and strength increase when confining pressures increases. The initial heating stage generates a transitory pore water overpressure due to thermal expansion, which creates microcracks probably parallel to the bedding plane. Despite the scattering of some results, an overall decrease of the peak strength with increasing temperature (until 100 °C) is observed because of to the thermo-hydro-mechanical damage induced by the initial heating. For the parallel samples under uniaxial conditions, this decrease is the most important and volumetric dilatancy develops during the loading for the highest temperatures. For all other conditions, the decrease is more moderate and there is no dilatancy because confining pressure reduces the creation of initial thermo-induced microcracks which are also closed when the axial stress was increased during the compression tests when the orientation is perpendicular. There is no noticeable impact of temperature up to 100 °C on the evolutions of the elastic coefficients. The peak strength increases at the highest temperature (150 °C) in all cases due to the water vaporisation and then strong samples desaturation, which induces the development of a very significant capillary suction. So far, only multi-step creep tests at  $T = 20$  °C and  $P_c = 2$  and 12 MPa, and at  $T = 80$  °C and  $P_c = 12$  MPa, for both parallel and perpendicular samples, were performed on the COx claystone. These first results showed that creep deformations are larger at higher temperature (80 °C) and that long-term strength seems to decrease with temperature. This conclusion has obviously to be confirmed when all the creep tests at different temperatures will be finished.

CEA realised a series of triaxial creep tests with two different claystones, Boom Clay and Opalinus Clay. First confined under isotropic stress, the samples were saturated with the adequate synthetic water, specific to each kind of claystone, injected at a constant pressure. Then the samples were heated up to a precise level of temperature which was maintained constant up to the end of the

experiment. Then several successive deviatoric stress levels were applied to the sample to investigate their time dependent behaviour. There were a series of multi-steps triaxial creep tests. Each experiment is performed under a constant temperature. Two testing benches, each equipped with two companion triaxial HOEK-type cells, were operated. Each bench ran with a specific temperature, maintained constant during all the creep sequences. Note that during the heating phase and during the creep sequences the drainage between the sample and the pore pressure tank was allowed, which maintained a constant pressure. As such, the creep experiments were conducted under drained conditions. With Boom Clay, the time-dependent behaviours have been investigated under three levels of temperature: 40°C, 60°C and 80°C. At 40°C three sequences of creep have been made with a maximal deviatoric stress equal to 3.51 MPa. Four creep sequences were made at 60°C, the maximal deviatoric stress was equal to 5.97 MPa. At 80°C a maximal deviatoric stress of 2.60 MPa was reached at the second creep step. Both the magnitude and the evolution kinetics of the creep strain were greater when the temperature was higher. With Opalinus Clay, two levels of temperature have been investigated: 40°C and 80°C. For each value of temperature, five creep sequences have been realised, with the maximal values of the deviatoric stresses equal to 9.17 and 10.0 MPa, for 40 °C and 80 °C respectively. The comparison between the two series of tests shows clearly that the magnitude of the strain is increased when the temperature was higher. Moreover, the kinetics is accelerated with higher temperature, and the strain stabilisation occurred later. The results of that experimental campaign show clearly that several tests are necessary to correctly investigate the time-dependent behaviour of each claystone. The natural variability between the two samples over-cored inside the same initial core of claystone seems to have a great influence on the magnitude of the strains. The kinetics of the evolution of the strains seems to be less sensitive to this variability. Some samples failed too early, preventing the experiment to be continued.

BGS undertook a series of oedometric ( $K_0$ ) experiments on candidate host rocks measuring the spatial and temporal development of porewater pressure caused by its thermal expansion and its subsequent impact on the evolution of intrinsic permeability. Experiments were performed across a range of temperatures from 20 to 90°C. Results demonstrate that in all cases the permeability was observed to decrease on heating, with the rate of change linked to the initial permeability of the sample. In Opalinus Clay (OPA), heating to around 70°C resulted in the development of local porewater pressures exceeding the axial stress, with peak pressure increasing with temperature. Porewater pressures exhibited local anisotropy and possible heterogeneity effects on the length-scale of the experiments. The permeability of the Callovo-Oxfordian (COx) was shown to be considerably lower than that of OPA, leading to higher peak porewater pressures and possible evidence of thermally induced mechanical failure. However, in all experiments, no evidence for the degradation of hydraulic properties was observed once temperatures had dissipated. Hydraulic anisotropy was measured for flow parallel and perpendicular to bedding and the impact of possible sample damage was explored. This study identified important hydromechanical couplings between peak porewater pressure, temperature, permeability and confining stress. Using these relationships, and a knowledge of the heat output of the waste, it is possible to calculate a repository depth below which thermally induced porewater pressures could be managed and always remain lower than the in-situ stress. While  $K_0$  experiments allow the measurement of formation overpressures, they impose a slightly artificial boundary condition and, when testing indurated materials such as OPA and COx, can be difficult to seal. However, although achieving an adequate seal is a complex task, the hydromechanical couplings identified by this study provide important insight into the integrity of the host rock and ultimately, safety assessment.

## List of Figures

### CNRS (ULorraine)

Figure 1 - Strains gages and coordinate system oriented with respect to the bedding plane of the (transverse isotropic) COx claystone cylindrical sample for both sample orientations (parallel to the bedding plane at the left, perpendicular to the bedding plane at the right). .....	23
Figure 2 - Sketch and photo of the experimental apparatus. ....	26
Figure 3 – Thermo-mechanical path for the short-term compression tests ( $\sigma_3$ : confining pressure, $\sigma_1$ : axial stress) at the left and for the creep tests at the right. ....	27
Figure 4 - Stress-strain curves of uniaxial tests ( $P_c = 0$ MPa) at different temperatures of samples cored in the direction parallel to the bedding plane. ....	31
Figure 5 - Stress-strain curves of triaxial tests at $P_c = 4$ MPa, at different temperatures of samples cored in the direction parallel to the bedding plane. ....	31
Figure 6 - Stress-strain curves of triaxial tests at $P_c = 12$ MPa, at different temperatures of samples cored in the direction parallel to the bedding plane. ....	32
Figure 7 - Stress-strain curves of uniaxial tests ( $P_c = 0$ MPa) at different temperatures of samples cored in the direction perpendicular to the bedding plane. ....	32
Figure 8 - Stress-strain curves of triaxial tests at $P_c = 4$ MPa, at different temperatures of samples cored in the direction perpendicular to the bedding plane. ....	33
Figure 9 - Stress-strain curves of triaxial tests at $P_c = 12$ MPa, at different temperatures of samples cored in the direction perpendicular to the bedding plane. ....	33
Figure 10 - Evolution of the deviatoric stress at peak (peak strength) as a function of temperature for parallel (left) and perpendicular (right) orientations and for all confining pressures (0, 4 and 12 MPa), with polynomial (3rd order) fitting. ....	34
Figure 11 - Evolution of the axial Young's modulus $E_{11}$ as a function of the deviatoric stress (normalized with the deviatoric stress at peak) at different temperatures and for all confining pressures - samples cored in the direction parallel to the bedding plane. ....	35
Figure 12 - Evolution of the Poisson's coefficients $\nu_{13}$ and $\nu_{12}$ as a function of the deviatoric stress (normalized with the deviatoric stress at peak) at different temperatures and for all confining pressures - samples cored in the direction parallel to the bedding plane. ....	36
Figure 13 - Evolution of the elastic coefficients (axial Young's modulus $E_{33}$ and Poisson's coefficient $\nu_{31}$ ) as a function of the deviatoric stress (normalized with the deviatoric stress at peak) at different temperatures and for all confining pressures - samples cored in the direction perpendicular to the bedding plane. ....	37
Figure 14 – Creep curves (deformations vs time) for parallel (EST66728-6) and perpendicular (EST66728-16) samples at $P_c = 2$ MPa and $T = 20$ °C for the different deviatoric stress levels (25%, 50% and 75% of the reference short-term peak strengths). ....	38
Figure 15 – Creep curves (deformations vs time) for parallel (EST66728-1) and perpendicular (EST66728-11) samples at $P_c = 12$ MPa and $T = 20$ °C for the different deviatoric stress levels (25%, 50% and 75% of the reference short-term peak strengths). ....	39
Figure 16 – Creep curves (deformations vs time) for parallel (EST66728-5) and perpendicular (EST66728-13) samples at $P_c = 12$ MPa and $T = 80$ °C for the different deviatoric stress levels (25%, 50% and 75% of the reference short-term peak strengths). ....	40

Figure 17 - Evolution of the axial strain at peak (measured with the strain gages) as a function of temperature for parallel and perpendicular orientations and for all confining pressures (0, 4 and 12 MPa), with polynomial (3rd order) fitting curves. .... 42

**CEA**

Figure 1 - Over-coring of Boom Clay with special coring tool. .... 48

Figure 2 - HOEK-type triaxial cell used for the creep experiments. .... 49

Figure 3 - Testing bench with two HOEK-type triaxial cells and loadframe inside the oven. .... 49

Figure 4 - Swelling of the sample during hydration under isotropic confinement. .... 52

Figure 5 - Different creep steps for sample BOOM-40C-01. .... 52

Figure 6 - Different creep steps for companion sample BOOM-40C-02. .... 52

Figure 7 - Successive creep steps realised on sample BOOM-40C-01. .... 53

Figure 8 - Successive creep steps realised on companion sample BOOM-40C-02. .... 53

Figure 9 - Successive creep steps realised on samples BOOM-40C-01 and BOOM-40C-02. .... 53

Figure 10 - Swelling of the two samples during hydration under isotropic confinement. .... 54

Figure 11 - Comparison of the successive creep steps with sample BOOM-60C-03. .... 54

Figure 12 - Comparison of the successive creep steps with sample BOOM-60C-04. .... 55

Figure 13 - Successive creep steps with sample BOOM-60C-03. .... 55

Figure 14 - Successive creep steps with sample BOOM-60C-04. .... 56

Figure 15 - Comparison of the successive creep steps for the two samples BOOM-60C-03 and BOOM-60C-04. .... 56

Figure 16 - Successive creep steps for sample BOOM-80C-05. .... 57

Figure 17 - Successive creep steps for companion sample BOOM-80C-06. .... 57

Figure 18 - Successive creep steps for sample BOOM-80C-05. .... 57

Figure 19 - Successive creep steps for companion sample BOOM-80C-06. .... 58

Figure 20 - Successive creep steps for the two samples BOOM-80C-05 and BOOM-80C-06. .... 58

Figure 21 - Strain evolution during the re-saturation phase for the two samples OPA-40C-01 and OPA-40C-02. .... 59

Figure 22 - Comparison of the different creep steps for sample OPA-40C-01. .... 59

Figure 23 - Comparison of the different creep steps for companion sample OPA-40C-02. .... 60

Figure 24 - Comparison of the different creep steps for companion sample OPA-40C-02. .... 60

Figure 25 - Comparison of the different creep steps for companion sample OPA-40C-02. .... 60

Figure 26 - Successive creep steps for the two samples OPA-40C-01 and OPA-40C-02. .... 61

Figure 27 - Strain evolution during the re-saturation phase for the two samples OPA-80C-03 and OPA-80C-04. .... 62

Figure 28 - Comparison of the different creep steps for sample OPA-80C-03. .... 62

Figure 29 - Comparison of the different creep steps for companion sample OPA-80C-04. .... 62

Figure 30 - Successive creep steps for sample OPA-80C-03. .... 63



Figure 31 - Successive creep steps for companion sample OPA-80C-04. .... 63

Figure 32 - Successive creep steps for the two samples OPA-80C-03 and OPA-80C-04. .... 63

Figure 33 - Comparison between two samples of Opalinus Clay, one tested at 40°C, another tested at 80°C. .... 64

**UKRI- BGS**

Figure 1 - [A] shows a cut away of the pressure vessel, end-closures, load cells and filters. [B] shows a photograph of the apparatus, assembled and in the oven ready for testing. The radial filters are located at 12.5, 30 and 47.5 mm along the axis of the sample measured from the injection filter. Samples are subject to a  $K_0$  stress boundary condition so are radially constrained but can swell in the axial direction. .... 67

Figure 2 - A] Schematic showing the layout of the key apparatus components. [B] schematic showing the position of the pore pressure sensors around the periphery of the sample. The movement of fluids into and out of the sample is controlled through high-precision syringe pumps. Samples are radially constrained but free to axially swell. .... 68

Figure 3 - Pre-test imaging of sample FPR-20-013. [A] Orthogonal CT; [B] CT image of features XY orientation; [C] CT image of features XZ orientation; [D] CT image of features YZ orientation; [E] injection face of sample [F] side view of sample; [G] backpressure face of sample.; [H] sample emplaced in the rig. .... 73

Figure 4 - [A] Time evolution of water pressure during hydration phase in test FPR-20-013. Inset is a schematic image of sample FPR-20-013 showing the direction of flow and relative positions of the radial filters. [B] Time evolution of water pressure during hydration phase (averaging sensors). First plane =  $(LC1 + LC11)/2$ ; second plane =  $(LC2 + LC22)/2$ ; third plane =  $(LC3 + LC33)/2$ . .... 75

Figure 5 - FPR-20-013. The development of porewater pressure during constant head test, stage [4]. .... 75

Figure 6 - FPR-20-013. Time evolution of water pressure during heating phase, stage [6]. Abrupt breaks in slope are suggestive of localised fracturing as porewater pressures approach or exceed the axial stress. .... 76

Figure 7 - Pre-test imaging of sample FPR-21-017. [A] Orthogonal CT; [B] CT image of features XY orientation; [C] CT image of features XZ orientation; [D] CT image of features YZ orientation; [E] injection face of sample [F] side view of sample; [G] backpressure face of sample. .... 77

Figure 8 - Sample FPR-21-027 prior to testing. [A] to [C] backpressure, side view and injection end-face images of sample. [D] 3D macro x-ray CT image of sample showing mineralised bioturbation features (different colours represent connected features). [E] 2D x-ray image showing bedding plane fractures propagating into the sample. .... 78

Figure 9 - Sample FPR-21-027: [[A] pore pressure development during heating to 90°C, test stage [7]. [B] average pore pressure values for test stage [7]. .... 80

Figure 10 - Sample FPR-21-051 prior to testing. [A] Orthogonal CT; [B] CT image of features XY orientation; [C] CT image of features XZ orientation; [D] CT image of features YZ orientation; [E] injection face of sample [F] side view of sample; [G] backpressure face of sample; [H] an image of the sample installed in the confining vessel with sample bedding aligned to the apparatus measurement plane (denoted by the black line). .... 82

Figure 11 - Sample FPR-21-051: [A] pore pressure development during heating to 88°C, test stage [9]. [B] average pore pressure values for test stage [9]. .... 83

Figure 12 - Sample FPR-21-052 prior to testing. [A], [B] and [C] are optical images of the pre-test sample (the red dot marks the injection end of the core). [D] is an image of the sample partly installed in the confining vessel with sample bedding aligned to the apparatus measurement plane (denoted by the black line). [E] is an X-ray CT image of the entire core from which the test sample originated (location is for illustrative purposes only). [F] is an image of the sample fully installed into the confining vessel..... 84

Figure 13 - Permeability versus temperature for sample FPR-21-052 at effective stresses of 4 MPa (blue circles) and 12 MPa (red dots). ..... 88

Figure 14 - Sample FPR-21-052: pore pressure development during heating. [A], [B] and [C] show individual sensor values on heating to 89°C, test stage [7], 69°C, test stage [13] and 50°C, test stage [17] respectively. [D], [E] and [F] show average pressure data across each plane of measurement. .. 89

Figure 15 - Sample FPR-21-052: [A] average peak pressure data for test stages [7], [13] and [17] under an axial stress of 6 MPa. [B] average peak pressures for test stages [28], [34] and [40] following the increase in axial stress to 14 MPa. [C] comparing data from graphs [A] and [B] illustrates the impact of increasing axial stress on peak pressures, showing the difference becomes more pronounced at temperature increases..... 90

Figure 16 - Sample FPR-22-025 prior to testing. [A], [B] and [C] are optical images of the pre-test sample (the black cross marks the injection end of the core). [D] is an image of the sample partly installed in the confining vessel with black line aligned to the apparatus measurement plane. [E] is an X-ray CT image of the sample highlighting some of the higher density features. .... 91

Figure 17 - Sample FPR-22-025 showing loading of the sample, the application of an accidental porewater pressure pulse and the subsequent step in porewater pressure. Values in parentheses represent test stage numbers..... 93

Figure 18 - Sample FPR-22-25: pore pressure development during heating. [A], [B] and [C] show individual sensor values on heating to 84°C, test stage [10], 66°C, test stage [16] and 49°C, test stage [22] respectively. [D], [E] and [F] show average pressure data across each plane of measurement. .. 93

Figure 19 - Sample FPR-22-025: permeability as a function of temperature..... 94

Figure 20 - Post-test imaging of sample FPR-22-067. [A] Orthogonal CT; [B] CT image of features XY orientation; [C] CT image of features XZ orientation; [D] CT image of features YZ orientation. [E], [F] and [G] pre-test optical images of sample showing side view (with injection end marked with a cross), backpressure face and injection face respectively. .... 95

Figure 21 - FPR-22-067 showing the initial loading and hydration of the sample. The fact radial porewater pressures match that of the injection/backpressure systems indicates sideways flow..... 96

Figure 22 - FPR-22-067. Plot of permeability against test duration. Data shows that swelling on OPA (subject to Pearson water) under oedometric testing is very slow and bypass flow can continue for many days. .... 97

Figure 23 - Post-test imaging of sample FPR-22-098. [A] Orthogonal CT, with evidence of lens features; [B] CT image of features XY orientation; [C] CT image of features XZ orientation; [D] CT image of features YZ orientation; [E] photo of backpressure end of core showing chip missing from the sample; [F] side view of core (black crosses mark injection end) adjacent to the vessel bore. .... 98

Figure 24 - FPR-22-098 showing the initial loading of the sample, stages [1] and [3], hydration, stage [4], and constant head testing, stage [5]. The fact radial porewater pressures match that of the injection/backpressure systems indicates sideways flow. Also apparent is that the radial sensors, even after an offset was applied to each device, begin to drift as the test progresses..... 100

Figure 25 - FPR-22-098. Plot of permeability against temperature. As with previous tests, sample FPR-22-098 exhibits a general trend of decreasing permeability with increasing temperature..... 100

Figure 26 - Summary of permeability against temperature data for tests undertaken in this study. ... 102

Figure 27 - Cross-plot of values taken from all four tests when temperature was initially increased to 90°C. While limited data is available, a crude trend between peak porewater pressure and permeability emerges. .... 103

Figure 28 - Cross-plot of values taken from all four tests when temperature was initially increased to 90°C. While limited data is available, a crude trend between peak porewater pressure and permeability emerges. .... 106

Figure 29 - Pressure evolution as a function of temperature in each sensor (corresponding to day 19.15 to 19.45). .... 106

Figure 30 - Sensitivity analysis of the change (in %) of the maximum corrected pressure with respect the maximum measured pressure when varying [a] the volume of the drainage system, [b] the thermal expansion coefficient of water for both the sample and the drainage system and [c] the compressibility of water in the drainage system and the compressibility of the drainage system. .... 108

Figure 31 - Net change in length as a function of temperature for days 19.15 to 19.45. Black-dotted line represents the temperature at which peak pressures are observed (in average). .... 109

Figure 32 - Axial strain as a function of temperature..... 109



## List of Tables

### CNRS (ULorraine)

Table 1 - References of the different boreholes and core samples used for the short-term compression tests and physical parameters.....	24
Table 2 - References of the different boreholes and core samples used for the triaxial creep tests and physical parameters. ....	25
Table 3 - References of the different samples for short-term compression tests, experimental conditions (the thermal loading corresponds to the rate of temperature increase + the waiting time before the mechanical test), peak strength (deviatoric stress at peak), post-mortem water content w and test duration at failure (i.e., at peak stress). ....	29
Table 4 - References of the different samples used for triaxial creep tests, experimental conditions (temperature, thermal loading confining pressure Pc), peak strength (deviatoric stress at peak) and test duration. ....	30

### CEA

Table 1 - Chemical composition of the pore water used for Boom Clay. ....	50
Table 2 - Chemical composition of the pore water used for Opalinus Clay. ....	50
Table 3 - Research plan for the multi-steps creep experiments.....	51
Table 4 - Features of the two Boom Clay samples tested at 40°C. ....	51
Table 5 - Features of the Boom Clay samples tested at 60°C. ....	54
Table 6 - Features of the Boom Clay samples tested at 80°C. ....	56
Table 7 - Features of the Opalinus Clay samples tested at 40°C. ....	58
Table 8 - Features of the Opalinus Clay samples tested at 80°C. ....	61

### UKRI- BGS

Table 1 - Location of radial porewater pressure filters which were 8 mm in diameter. ....	68
Table 2 - Chemical composition of the synthetic COx solution used to test FPR-20-013.....	69
Table 3 - Chemical composition and properties of the synthetic Boom Clay solution used for the natural samples in this study. ....	69
Table 4 - Chemical composition of the synthetic OPA solution (often referred to as Pearson porewater) used for the test of all Opalinus Clay samples. ....	70
Table 5 - Density and viscosity values used to correct permeability values during heating tests.....	70
Table 6 - Pre- and post-test sample dimensions. All samples slightly increase in volume, indicating swelling has taken place – a necessity for K0 testing. ....	71
Table 7 - BGS test matrix. Tests FPR-21-017, -024, -026 and 22-067 failed for various reasons listed in the table. Test FPR-21-052 included measurement of pore pressure development and permeability values at multiple temperatures and two stress states. COx = Callovo-Oxfordian Claystone, OPA = Opalinus Clay, BC = Boom Clay. Para = parallel to bedding, perp = perpendicular to bedding.....	72
Table 8 - Experimental stages for test FPR-20-013. Stages denoted by EQ = equilibration, CHT = constant head test; TI = temperature increase and TD = temperature decrease. ....	74



Table 9 - FPR-20-013. Intrinsic permeability (k) data from ambient and elevated temperature testing where  $k_{in}$  = permeability based on inflow,  $k_{out}$  = permeability based on outflow and  $k_{ave}$  = the average permeability based on inflow and outflow values. Inflow data from the around 88 °C was not available due to leakage from the pipework during that phase of testing..... 75

Table 10 - Experimental stages for test FPR-21-017. Stages denoted by EQ = equilibration, CHT = constant head test; TI = temperature increase and TD = temperature decrease. .... 76

Table 11 - Test FPR-21-027 – showing the type of experimental stage and boundary conditions for the test. Note Ramp = an increase in stress and/or porewater pressure; EQ = equilibration stage; CHT = constant head test and TI = temperature increase..... 79

Table 12 - Test FPR-21-027. Intrinsic permeability (k) data from ambient and elevated temperature testing where  $k_{in}$  = permeability based on inflow,  $k_{out}$  = permeability based on outflow and  $k_{ave}$  = the average permeability based on inflow and outflow values. .... 79

Table 13 - Test FPR-21-051 showing the type of experimental stage and boundary conditions for the test. Note Ramp = an increase in stress and/or porewater pressure; EQ = equilibration stage; CHT = constant head test; TI = temperature increase and TD = temperature decrease. .... 81

Table 14 - Test FPR-21-051. Intrinsic permeability (k) data from ambient and elevated temperature testing where  $k_{in}$  = permeability based on inflow,  $k_{out}$  = permeability based on outflow and  $k_{ave}$  = the average permeability based on inflow and outflow values. .... 81

Table 15 - Test FPR-21-052 (stages 1 to 30) showing the type of experimental stage and boundary conditions for the test. Note Ramp = an increase in stress and/or porewater pressure; EQ = equilibration stage; CHT = constant head test; TI = temperature increase and TD = temperature decrease. Test remains on-going. .... 85

Table 16 - Test FPR-21-052 (stages 30 to 45) showing the type of experimental stage and boundary conditions for the test. Note Ramp = an increase in stress and/or porewater pressure; EQ = equilibration stage; CHT = constant head test; TI = temperature increase and TD = temperature decrease. Test remains on-going. .... 86

Table 17 - Test FPR-21-052 – Intrinsic permeability (k) data from ambient and elevated temperature testing where  $k_{in}$  = permeability based on inflow,  $k_{out}$  = permeability based on outflow and  $k_{ave}$  = the average permeability based on inflow and outflow values. Inflow data from stage [5] was not available due to a to leakage from the pipework during that phase of testing..... 87

Table 18 - Test FPR-22-025 showing the type of experimental stage and boundary conditions for the test. Note Ramp = an increase in stress and/or porewater pressure; EQ = equilibration stage; CHT = constant head test; TI = temperature increase and TD = temperature decrease. Test remains on-going. .... 92

Table 19 - Test FPR-22-025. Intrinsic permeability (k) data from ambient and elevated temperature testing where  $k_{in}$  = permeability based on inflow,  $k_{out}$  = permeability based on outflow and  $k_{ave}$  = the average permeability based on inflow and outflow values. .... 94

Table 20 - Test FPR-22-067 showing the type of experimental stage and boundary conditions for the test. Note Ramp = an increase in stress and/or porewater pressure; EQ = equilibration stage; CHT = constant head test; TI = temperature increase and TD = temperature decrease. .... 96

Table 21 - Test FPR-22-067. Intrinsic permeability (k) data from ambient and elevated temperature testing where  $k_{in}$  = permeability based on inflow,  $k_{out}$  = permeability based on outflow and  $k_{ave}$  = the average permeability based on inflow and outflow values. .... 97

Table 22 - Test FPR-22-098 showing the type of experimental stage and boundary conditions for the test. Note Ramp = an increase in stress and/or porewater pressure; EQ = equilibration stage; CHT = constant head test; TI = temperature increase and TD = temperature decrease. Test remains on-going. .... 99



Table 23 - Test FPR-22-067. Intrinsic permeability (k) data from ambient and elevated temperature testing where $k_{in}$ = permeability based on inflow, $k_{out}$ = permeability based on outflow and $k_{ave}$ = the average permeability based on inflow and outflow values. ....	100
Table 24 - Measured thermal pressurisation coefficients.....	106
Table 25 - Corrected thermal pressurisation values and their effect on maximum pressured observed in each sensor. ....	107
Table 26 - Time (in days) and temperature (in °C) at which the linear relationship between $\Delta u$ and $\Delta T$ is no longer valid.....	108



## Glossary

HLW	High-Level Waste
WP	Work Package
HHGW	High-Heat-Generating-Waste
BC	Boom Clay
COx	Callovo-Oxfordian claystone
OPA	Opalinus Clay
EDZ	Excavation Damaged Zone



## 1. Introduction

The WP7 “Influence of Temperature on Clay-based Material Behaviour” of the EURAD Project aims to develop and document an improved thermo-hydro-mechanical (THM) understanding of clay-based materials (host rocks and buffers) exposed at high temperatures ( $>100^{\circ}\text{C}$ ) or having experienced high temperature transients for extended durations. The heat generated by waste must not affect the favourable properties of the host rock, especially its transport properties, for containment. The overpressure generated by the difference between thermal expansion coefficient of pore water and the solid rock skeleton may have deleterious consequences. In far field (subtasks 2.2), this could induce rock damage and reactivate fractures/faults. In the near field (subtasks 2.1), i.e., in the vicinity of the cell, characterised by a fractured zone, this could induce fracture opening or propagation, altering the permeability. Laboratory experiments in subtasks 2.1 and 2.2 investigate the near-field and far-field effects of heating on the properties and behaviour of the host rocks and in subtask 2.3 several THM models are developed and improved.

Thus, the main objective is to increase knowledge of the THM behaviour of clay host rock to help to optimise the repository design. More specifically, from experiments (for both near and far fields), modelling and benchmarking, the following questions will be addressed:

- Do we sufficiently understand the processes leading to the observed overpressures and changes in the stress state? How can experiments be best designed to characterise the most sensitive parameters?
- How good are the current THM models in representing the stress changes at repository-relevant conditions?
- What are the THM criteria that can act as credible site-specific design criteria? The basic assumption is that no irreversible or long-term damage to the rock should occur. How can one best demonstrate that these design criteria can be met?
- In the very unlikely case of damaging (fracturing) the rock, what will be the consequences and can we expect self-sealing in clay rich rock to occur as soon as the energy is released?

The characterisation of in-situ THM behaviour of the clay host rock is significant for the design of the underground nuclear waste disposal facility and to provide long-term safety. When temperature increases in a low-permeability medium, the pore water is compressed because of the difference between its thermal expansion coefficient and that of the solid skeleton of the rock, which leads to an overpressure. An improved knowledge of the THM behaviour will help to optimise repository design (spacing in between HLW cells, load on casing/canister).

The temperature rise in a low permeability porous medium, such as Callovo-Oxfordian and Opalinus claystones, generates a pore pressure increase essentially due to the difference between the thermal expansion coefficients of water ( $\sim 10^{-4}\text{K}^{-1}$ ) and the argillaceous rock skeleton ( $\sim 1.28 \times 10^{-5}\text{K}^{-1}$  for COx). Thermal pressurisation is the key mechanism for the potential damage induced by the heat emitted from the waste. There is a competition between excess pore pressure due to thermal pressurisation and drainage due to pore pressure gradient increase. With the periodic distribution of an important number of similar parallel tunnels/micro tunnels and their lengths, it can be expected that the induced pore pressure between tunnels/micro tunnels could not be dissipated in the horizontal direction. Due to the symmetry conditions, horizontal displacement, thermal flow and fluid flow are set to zero on the lateral boundaries of the model. The periodic distribution of parallel cells prevents lateral expansion of the rock and thus provokes compression of the thermal stresses in the horizontal direction. The decrease of the total stress sets off the effect of the pore pressure build-up on the horizontal components of the effective stress tensor. However, in the far field (**subtask 2.2**), the vertical effective stress decreases and can reach the tensile strength of the rock and cause damage (i.e., potential appearance of sub-horizontal cracks) or possibly fault reactivation. An extension of the excavation damaged zone (EDZ) in the near-field is also possible.

The present report - D7.5 - Technical report on effect of temperature on far field properties - is the final deliverable for **subtask 2.2**. It is based on laboratory experiments on clay host rocks to provide answers about the effects of increased temperature on the short and long-term mechanical behaviours

(deformations, elastic properties, failure strength) and on evolution of damage and intrinsic permeability due to porewater overpressures. Laboratory experiments will be performed for this purpose on core samples of candidate clay host rocks using triaxial and oedometric testing cells.

Excavation of underground galleries (such as radioactive waste repository) in rocks creates generally a network of cracks near the excavation zone called an Excavation Damaged Zone (EDZ). In France (Meuse/Haute-Marne), the Callovo-Oxfordian (COx) Claystone is the selected host rock for the underground disposal of radioactive waste by Andra, due to its radionuclide retention properties, its low permeability (Grgic et al. 2023; Escoffier et al. 2005; Homand et al. 2004), and its self-sealing properties (Agboli et al. 2023; Giot et al. 2019). In the current design of the disposal project of Andra (Cigéo), the radioactive waste will be emplaced in horizontal micro-tunnels excavated in the rock located at a depth of 500 m under the village of Bure, and around which EDZs have been observed. The high-heat-generating-waste (HHGW) will lead to heating of the clay host rock in the areas located near the excavations, whose effects should be known to help optimize the design of the disposal. The heat generated by the waste must not affect the favourable properties of the host rock, more precisely its mechanical and transport properties. Indeed, the evolution of the effective stresses field in the vicinity of the cells due to the temperature increase can induce opening or propagation of fractures in this EDZ. Then, the knowledge of the impact of temperature on the mechanical properties of clay host rocks is of great importance.

The Table below presents a synthesis of experiments to be performed by the different partners for subtask 2.1.

Table - Synthesis of partners experimental program in subtask 2.2.

Partner Material	[CNRS (ULorraine)]	[CEA]	[UKRI- BGS]
<b>COx</b>	- Short-term triaxial compression tests - Triaxial creep tests	- Triaxial creep tests on OPA and Boom	Effect of porewater overpressure on THM behaviour and permeability in load cell
<b>OPA</b>		- Triaxial extension tests on COx and OPA	
<b>Boom clay</b>			

The materials used in this subtask 2.2 are:

- **Callovo Oxfordian claystone (COx)** taken in the clayey unit. Origin: The Industrial Centre for Geological Disposal (Cigeo) located at Bure (Meuse/Haute-Marne, France).

Callovo-Oxfordian (COx) claystone is the host rock chosen in France for the storage of radioactive waste, more precisely in Meuse/ Haute-Marne (Bure, France). It is 160 million years old and, with a thickness of about 130 m, and located under Bure at a depth of 400 to 600 m. The COx claystone is a very low permeability rock. Its mineral composition varies as a function of depth mainly due to geological sedimentary cycles (Lefranc et al. 2008) and the clay mineral content is roughly anti-correlated with the carbonate content. It corresponds to (Mohajerani 2011; Montes et al. 2004; Robinet et al. 2012, 2015; Sammartino et al. 2003): 20–60% of phyllosilicates (illite, interstratified illite/smectite, kaolinite, mica, chlorite), 10–40% of tectosilicates (quartz, feldspars), 15–80% of carbonates (calcite, dolomite), 0–3% of pyrite, iron oxides with less than one percent organic matter. The three main

phases are clay minerals, quartz, and calcite (Yven *et al.* 2007). It is worth emphasizing that this argillite contains a high content of swelling clay minerals (smectites).

From the base to the top of the layer, the COx formation was divided into four lithostratigraphic units (C2a to C2d) and several petrophysical units (UA1, RIO, UA2, UA3, UT, USC1, RSO, and USC2) defined for the Andra project (Pellenard *et al.* 2014). The COx claystone consists mainly of three different layers to be more precise (Giot *et al.* 2019). There is the silto-carbonated unit (USC) which is on the top of the COx layer and is the most carbonated one. Its mineralogical composition is contrasted and variable; its porosity is about 15%. Then, there is the transition unit (UT), which is more homogeneous and with a clay content between 30 and 40%. The carbonate content increases from the bottom (20%) to the top (30%). Finally, there is the clay unit (UA), which is the most clayey unit, with clays, carbonate and quartz contents of about 45–50%, 27% and 24%, respectively. Armand *et al.* (2017) report that the UA unit makes up two-thirds of the total geological layer thickness.

The work of Andra (Andra 2005) showed that the pore space of the COx claystone represents about 18%. This porosity is made up of approximately 10% macropores ( $> 1 \mu\text{m}$ ), 86% (0.1  $\mu\text{m}$  to 1  $\mu\text{m}$ ) mesopores and 4% ( $< 1 \mu\text{m}$ ) micropores according to the three classes listed in the work of Coll (2005). Initial stresses within the claystone are about 12 MPa at the level of the radioactive waste storage which corresponds to the lithostatic pressure at a depth of 500 m (Gratier *et al.* 2004). Water permeability tests (Andra 2005; Escoffier 2002) give values between  $5.10^{-20}$  and  $5.10^{-21} \text{ m}^2$ .

- **Opalinus clay (OPA)**. Origin: Mont Terri underground laboratory (Mont Terri, Switzerland).

The Opalinus Clay (OPA) is a Jurassic (Aalenian, ~180 Ma) shallow marine clayshale found in Switzerland. The formation, named after the ammonite *Leioceras opalinum*, consists of indurated dark grey micaceous claystones (shales) that are subdivided into several lithostratigraphic units. Some of them contain thin sandy lenses, limestone concretions, or siderite nodules. The clay-mineral content ranges from 40 – 80 wt% (9 – 29 % illite, 3 – 10 % chlorite, 6 – 20% kaolinite, and 4 – 12 % illite/smectite mixed layers in the ratio 70/30). Other minerals are quartz (15 – 30 %), calcite (6 – 40 %), siderite (2 – 3 %), ankerite (0 – 3 %), feldspars (1 – 7 %), pyrite (1 – 3 %), and organic carbon (<1 %). The total water content ranges from 4 – 19 % (Gautschi, 2001). At the Mont Terri underground research laboratory, three facies can be distinguished: a shaly facies in the lower half of the sequence, a 15 metre thick sandy, carbonate-rich facies in the middle of the sequence and a sandy facies interstratified with the shaly facies in the upper part. For the current study, samples from the shaly facies were used. The OPA at Mont Terri is an over-consolidated shale with a maximum burial depth of 1,200m and is presently around 280m depth.

- **Boom clay**. Origin: HADES Underground Research Laboratory (Mol, Belgium).

The geological and hydrogeological setting of the Boom Clay in northern Belgium has been summarised by Beerten & Leterme (2012) and in the Netherlands by Vis & Verweij (2014). The Boom Clay (usually referred to as the Rupel Clay in the Netherlands) is of lower Oligocene (ca 28 to 34 Ma) age and forms part of the Rupel Formation. In the Netherlands the Rupel Formation has been subdivided into the Vessem, Rupel Clay and Steensel members (Wong *et al.*, 2007). These members are diachronous, with both the basal Vessem and the overlying Steensel members being sandy marine deposits (Vis & Verweij; 2014) laid down close to the palaeo-shorelines. The Boom Clay is a pyritic, grey to dark brown marine clay with septarian (carbonate rich) concretions. Towards the basin margins the clays grade into sands. The formation reaches a maximum thickness of up to 250 m, with a mean thickness of around 65 m, and dips gently towards the north-east at between 1 and 2°.

The core material used in the current study was taken from the HADES underground research laboratory at Mol in Belgium. Here, the Boom Clay consists mainly of mixed clay and silt, with additional minor sand (Bernier & Bastiaens, 2007). Mineralogical composition of the Boom Clay is widely reported, predominantly assessed using XRD. The clay content is generally reported to vary

from between 23 and 60 % of the bulk material composition and is predominantly made up of illite, smectite, and kaolinite, which is often seen in interlaminated zones (Blanchart *et al.*, 2012; Dehandschutter *et al.*, 2004; Wemaere *et al.*, 2008; Yu *et al.*, 2012). The non-clay fraction of the Boom Clay primarily consists of quartz, again widely reported to vary between 23 and 60 %. The remaining percentage of the non-clay fraction consists of feldspars, calcite, and pyrite. Honty & De Craen (2011) report the composition to be 22-77 % quartz, 0-6.3% albite, 0.4-17.3% k-feldspar, 0-1.5% siderite, 0-4.6% calcite, 0-2% apatite, 0.3-5% pyrite, 5-37% illite/muscovite, 6.8-35% smectite + illite/smectite, 2-16% kaolinite, and 14-4% chlorite. This demonstrates the variability of Boom Clay.

## 2. CNRS (ULorraine)

### 2.1 Introduction

In recent years, various studies on the Thermo-Hydro-Mechanical (THM) behaviour of the COx claystone have been performed in the laboratory, in different environments and with various experimental methods. Thermal pressurization tests in drained and undrained conditions in hollow cylinders and in isotropic cells (Masri et al. 2014; Blaise et al. 2014; Mohajerani et al. 2012; Mohajerani et al. 2013) allowed the determination of the thermal pressurization coefficient, drained and undrained thermal expansion coefficient of the rock subjected to heating. Heating tests of the COx claystone on cylinders at temperatures ranging from 27 °C to 150 °C in drained and undrained conditions (Zhang et al. 2013) also revealed an expansion of the material from 27 to 100 °C, and a contraction of the material between 100 and 150 °C. Therefore, it seemed obvious to study the effect of temperature on the mechanical properties of the COx claystone. Thus, Liu et al. (2019) performed triaxial tests with lateral decompression from 20 to 90 °C and showed that the increase in temperature induces a degradation of the shear strength as well as the elastic properties of the COx argillite. Lateral decompression tests were also performed by Zhang (2021) on cylindrical samples cored in the direction perpendicular to the bedding plane for confining stresses of 10 and 12.5 MPa and for temperatures ranging from 20 and 90 °C. These tests showed also a slight decrease in the failure strength with increasing temperature. It seems therefore important to study the influence of temperature on the mechanical behaviour of the COx claystone.

This study focuses on the effect of temperature on the short and long-term mechanical properties of the COx claystone. Thus, short-term compression tests in a triaxial cell with axial and lateral strains measurements are carried out at different temperatures (20, 40, 60, 80, 100 and 150 °C), for different confining pressures (0, 4 and 12 MPa) and orientations (loading direction parallel and perpendicular to the bedding plane). The underground disposal of radioactive waste is designed for a maximum temperature of 90 °C in the host rock in France, but it is still interesting, from a scientific point of view, and useful, for safety purpose, to investigate higher temperatures. In addition, multi-step creep tests in a triaxial cell with axial and lateral strains measurements are carried out at different temperatures (20, 40, 60, and 80 °C), for different confining pressures (2 and 12 MPa) and orientations (loading direction parallel and perpendicular to the bedding plane) to characterize the long-term mechanical behaviour. The confining pressures were chosen to be representative of the stress conditions in the near and far fields of the underground galleries for deep geological disposal of radioactive waste at a depth of 500 m. Results will be analysed in terms of sample orientation, confining pressure, mechanical properties (deformations, elastic coefficients and failure strength), thermal loading rate and water saturation degree.

## 2.2 Material and methods

### 2.2.1 Material and sampling

#### 2.2.1.1 Description of the COx claystone

The Callovo-Oxfordian (COx) claystone, which is the host rock chosen in France for the deep geological disposal of radioactive waste, was used for the purpose of this study. The material comes from Andra's Meuse/Haute Marne underground research laboratory located at Bure which is excavated at two levels of 445 m and 490 m below the surface, in the middle of the sub-horizontal layer of COx claystone that is 160 million years old, with a thickness of about 130 meters under Bure. The mineral composition of the COx argillite has been widely studied in the past by many researchers (e.g., Robinet et al. 2015; Montes et al. 2004; Bauer-Plaindoux et al. 1998; Wright 2001). It consists in: 20-60% of phyllosilicates (illite, interstratified illite/smectite, kaolinite, mica, chlorite), 10-40% of tectosilicates (quartz, feldspars), 15-80% of carbonates (calcite, dolomite), 0-3% of pyrite, iron oxides

and a small proportion of organic components. The relative proportions of clay and carbonates phases vary with depth. From a simplified microstructural point of view, the COx claystone is composed of a homogeneous clay matrix surrounding solid inclusions/grains of silicates and carbonates (mainly quartz and calcite) of diameter lower than 200 µm (Gasc-Barbier 2002).

Four different forms of water are present in claystones such as the COx claystone (Revil et Glover 1998): i) structural water contained in the mineral network ; ii) interfoliar water present between the clay minerals (physiosorbed), notably in the swelling phase of the clay; iii) the adsorbed water on the surface of the particles linked to the Van der Waals and dipole-dipole forces, which attract the water molecules against the surface of the minerals and which represents a layer of water of approximately 1 nm thickness; iv) the free water present mainly in the macropores and circulating freely in the rock, which is not subjected to any force except the capillary forces in the case of water-gas presence.

Yven et al. (2007) defined three kinds of porosities from laboratory measurements by combining mercury porosity and gas-adsorption techniques: a macro-porosity at the interface between the clay matrix and the other minerals (characterized by micrometric and sub-micrometric pore sizes) representing between 20 to 40% of the total connected porosity, a meso-porosity internal to the clay matrix (characterised by infra-micrometric to nanometric pore sizes) representing approximately 60 to 80% of the total connected porosity, and a small (less than 2%) intraparticle micro-porosity determined by nitrogen adsorption. According to several authors, the total porosity of the rock varies between a minimum of 9% in carbonated layers and a maximum of 20% in most argillaceous layers (Wright 2001; Gasc-Barbier et Marsily 2002; Esteban 2006; Yven et al. 2007).

Numerous laboratory studies have been conducted to assess the water permeability of COx claystone using several types of water: site water, synthetic water, or pure water. Thus, the permeability to site water on intact samples (M'Jahad 2012) is about  $10^{-20}$ - $10^{-21}$  m<sup>2</sup>, the permeability to pure water is about  $10^{-20}$ - $10^{-21}$  m<sup>2</sup> on intact material (Song 2014) and about  $10^{-18}$ - $10^{-21}$  m<sup>2</sup> on fractured material (Davy et al. 2007). Finally, the synthetic water permeability on the intact material (Homand et al. 2004) is about  $5 \cdot 10^{-20}$ - $5 \cdot 10^{-21}$  m<sup>2</sup>.

#### 2.2.1.1 Sampling

COx claystone cylindrical samples of 20 mm diameter and 40 mm height approximately were obtained from drill cores (plugs or cells) extracted from two different horizontal boreholes coming from the underground research laboratory of Andra: OHZ3010 (drilled in January 2022) and PGZ3004 (drilled in March 2022). Both boreholes were drilled in the clayey facies of the COx claystone. The laboratory experimental campaign to characterize the short-term mechanical behaviour started as soon as the in-situ boreholes were extracted and it lasted about one year. The laboratory experimental campaign to characterize the long-term mechanical behaviour (creep tests) started in 2023 and is still in progress. The references of the different boreholes, drill cores (plugs or cells) and samples used for the short-term experiments (compression tests) and for the long-term experiments (triaxial creep tests) are summarized in Tables 1 and 2, respectively. All cylindrical core samples with axis perpendicular to the bedding plane were extracted from the same borehole PGZ3004. The samples with axis parallel to the bedding plane were extracted from both boreholes (PGZ3004 and OHZ3010). Unfortunately, it was not possible to carry out the whole laboratory experimental campaign on the same borehole, due to the large number of experiments. In addition, it is worth emphasizing that drill cores of the borehole OHZ3010 were put in T1 type cells, which means that they are wrapped in a rubber membrane and confined under pressure, axially (with a spring) and radially (with expansive mortar). This allows the rock sample to be kept as close as possible to its original state (stress state and water content), thus preserving it from any significant damage during the storage stage (between the in-situ drilling and the laboratory mechanical test). However, drill cores of the borehole PGZ3004 were only wrapped with an aluminium foil under vacuum, which allows a very good preservation of the initial water content but not the stress state. Therefore, the long-term conservation of the initial mechanical properties is better with

the T1 cells (borehole OHZ3010) than the cells aluminium foil under vacuum, which may have an impact (very difficult to estimate) on the reliability and the representativity of the experimental results.

Due to the presence of bedding planes, the COx claystone exhibits structural anisotropy (transverse isotropy). The mechanical behaviour depends then on the loading direction with respect to the bedding plane. Two orientations of the cylindrical sample axis were then considered, namely perpendicular and parallel to the bedding plane. During the mechanical tests, samples deformations ( $\epsilon_{11}$ ,  $\epsilon_{22}$  and  $\epsilon_{33}$ ) are measured with strain gages. Considering that the COx claystone is a transversely isotropic material, the reference frame (1, 2, 3) is defined in Figure 1 for a cylindrical sample, (1, 2) being the bedding plane. For each main deformation, two strain gages, facing each other on the cylindrical sample, are glued (with an epoxy resin) on the sample surface at half height. For samples cored perpendicularly to the bedding plane ( $\theta = 0^\circ$ ), one axial deformation and one lateral deformation are measured, while one axial deformation and two lateral deformations are measured for samples cored parallel to the bedding plane ( $\theta = 90^\circ$ ), as illustrated in Figure 1. The convention of positive compressions for stresses and strains will be used.

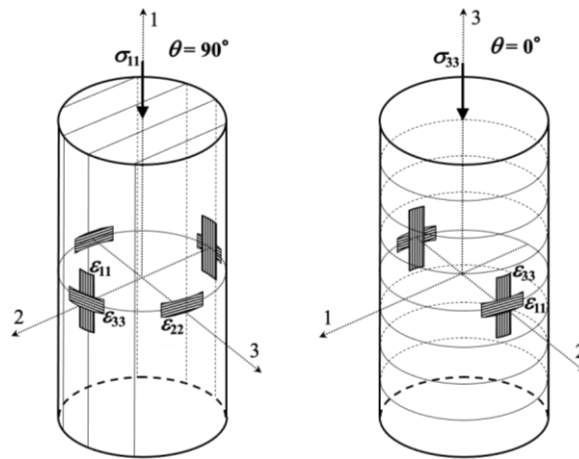


Figure 1 - Strains gages and coordinate system oriented with respect to the bedding plane of the (transverse isotropic) COx claystone cylindrical sample for both sample orientations (parallel to the bedding plane at the left, perpendicular to the bedding plane at the right).

Measurements of calcium carbonate content and solid matrix density  $\rho_s$  (obtained with the Helium pycnometer) were carried out on each drill core from a rock powder (made from a fragment of the drill core). The control of the calcium carbonate content is very important to verify the material homogeneity. The natural mass water content  $w$  (after passing through the oven at  $105^\circ\text{C}$  during 48 hours at least) and the natural density  $\rho_{nat}$  were determined for each tested core sample. The water content  $w$  is measured on a fragment taken near the core specimen in the core off-cuts. The bulk dry density  $\rho_d$  can then be obtained for each tested core sample from:

$$\rho_d = \frac{\rho_{nat}}{1+w} \quad (1)$$

Then, the total porosity  $n_t$  can be calculated for each core sample as follows:

$$n_t = 1 - \frac{\rho_d}{\rho_s} \quad (2)$$

Finally, the initial liquid saturation degree  $S_l$  can be obtained for all tested samples:

$$S_l = \frac{w\rho_d}{n_t\rho_w} \quad (3)$$

Where  $\rho_w$  is the water density.

It is worth emphasizing that the uncertainty on the total porosity  $n_t$  and the liquid saturation degree  $S_l$  is significant since they are calculated from many other parameters some of whom ( $w$ ,  $\rho_s$ ) were not directly measured on the considered sample. The physical parameters of all core samples are summarized in Tables 1 and 2. We can see that the physical properties of the different samples, taken from different drill core of the clayey facies of the COx claystone, are very homogeneous. Also, in order to ensure that all samples are initially healthy/intact, all of those presenting visible cracks were not selected for the mechanical experiments. These two points are very important in order to make relevant comparisons between them.

The mechanical properties of the COx claystone have been shown to be very sensitive to water saturation and the microstructure is damaged during the water desaturation or resaturation processes (Auvray et al. 2015; Liu et al. 2017; Zhang 2015; 2017; Bemmer et al. 2004; Montes et al. 2004; Conil et al. 2018; Grgic et al. 2023). Therefore, special attention was taken in this study to minimize samples damage due to variation in water saturation. First, the samples were carefully stored after core drilling and preparation to avoid a significant decrease in water content during the waiting time before the mechanical test and keep the water saturation degree of the samples as close as possible to that of the original drill core (i.e., close to 100%). Second, according to the recommendations of Andra, the samples were not resaturated before the mechanical tests to avoid a significant damage of the material (decrease of the peak strength up to 50% according to Grgic et al. 2023), which would complicate the interpretation of the experimental results presented here. The initial liquid saturation degree of all tested samples is given in Tables 1 and 2. The little desaturation ( $90\% < S_l < 97\%$ ), due to core drilling and sample preparation, is within an acceptable limit fixed at  $\sim 90\%$  by Andra for mechanical testing (Conil et al. 2018). This water saturation range of all samples (is not that wide and has also to be relativized considering the significant experimental uncertainty on this parameter, as said above. Therefore, one can reasonably consider that all samples are a little desaturated with almost the same initial liquid saturation degree. This reasonable assumption allows us to consider that the initial capillary suction is almost the same in all samples, which will facilitate the interpretation of the experimental results. And obviously, the mechanical results will be interpreted in terms of total stresses since the effective stresses are unknown.

Table 1 - References of the different boreholes and core samples used for the short-term compression tests and physical parameters.

Borehole	Core sample	Orientation	w (%)	$S_l$ (%)	$\rho_{nat}$ (g/cm <sup>3</sup> )	$\rho_d$ (g/cm <sup>3</sup> )	$\rho_s$ (g/cm <sup>3</sup> )	$n_t$ (%)	CaCO <sub>3</sub> (%)
OHZ3010 T1 cell	EST66420-1	Parallel	6.6	90.3	2.39	2.25	2.69	16.4	25.9
	EST66420-2	Parallel	6.6	90.1	2.39	2.24	2.69	16.4	25.9
	EST66420-3	Parallel	6.6	90.5	2.39	2.25	2.69	16.4	25.9
	EST66420-4	Parallel	6.7	90.2	2.39	2.24	2.69	16.6	25.9
	EST66420-5	Parallel	6.7	90.9	2.39	2.24	2.69	16.5	25.9
	EST66420-7	Parallel	6.7	90.5	2.39	2.24	2.69	16.6	25.9
	EST66420-8	Parallel	6.7	90.8	2.39	2.24	2.69	16.5	25.9
	EST66421-1	Parallel	6.7	92.7	2.40	2.25	2.68	16.3	25.8
	EST66421-2	Parallel	6.7	93.1	2.40	2.25	2.68	16.2	25.8
	EST66421-3	Parallel	6.7	92.7	2.40	2.25	2.68	16.3	25.8
	EST66421-4	Parallel	6.7	92.6	2.40	2.25	2.68	16.3	25.8
	EST66421-6	Parallel	6.7	93.9	2.40	2.25	2.68	16.1	25.8
	EST66421-8	Parallel	6.7	92.0	2.40	2.25	2.68	16.4	25.8
	EST66418-4	Parallel	6.3	91.1	2.41	2.25	2.69	15.7	25.4
EST66418-9	Parallel	6.3	90.9	2.41	2.27	2.69	15.7	25.4	
PGZ3004 Cells with vacuum aluminium	EST66721-1	Parallel	7.0	95.2	2.39	2.23	2.67	16.3	22.3
	EST66721-2	Parallel	7.0	94.7	2.39	2.23	2.67	16.4	22.3
	EST66721-3	Parallel	7.0	94.9	2.39	2.23	2.67	16.3	22.3
	EST66721-4	Parallel	7.0	93.3	2.38	2.23	2.67	16.6	22.3

foil	EST66723-1	Parallel	7.0	91.7	2.37	2.21	2.66	16.9	20.8
	EST66723-2	Parallel	7.0	91.0	2.37	2.21	2.66	17.0	20.8
	EST66723-3	Parallel	7.0	91.1	2.37	2.21	2.66	17.0	20.8
	EST66723-4	Parallel	7.0	91.3	2.37	2.21	2.66	17.0	20.8
	EST66723-6	Parallel	7.0	91.6	2.37	2.21	2.66	16.9	20.8
	EST66723-7	Parallel	7.0	90.9	2.37	2.21	2.66	17.0	20.8
	EST66723-8	Parallel	6.9	90.6	2.37	2.21	2.66	16.9	20.8
	EST66723-9	Parallel	6.9	90.7	2.37	2.21	2.66	16.8	20.8
	EST66723-10	Parallel	6.9	91.2	2.37	2.22	2.66	16.8	20.8
	EST66760-11	Perpendicular	7.2	94.8	2.37	2.21	2.66	16.8	20.8
	EST66760-12	Perpendicular	7.2	95.0	2.37	2.21	2.66	16.8	20.8
	EST66760-13	Perpendicular	7.2	94.1	2.37	2.21	2.66	16.9	20.8
	EST66760-14	Perpendicular	7.2	94.6	2.37	2.21	2.66	16.8	20.8
	EST66760-15	Perpendicular	7.2	94.7	2.37	2.21	2.66	16.8	20.8
	EST66760-16	Perpendicular	7.2	93.4	2.37	2.21	2.66	17.0	20.8
	EST66762-11	Perpendicular	7.2	94.9	2.37	2.21	2.66	16.8	20.8
	EST66762-13	Perpendicular	7.2	93.5	2.37	2.21	2.66	17.0	20.8
	EST66762-14	Perpendicular	7.2	93.2	2.37	2.21	2.66	17.0	20.8
	EST66762-15	Perpendicular	7.2	95.2	2.37	2.21	2.66	16.8	20.8
	EST66764-11	Perpendicular	7.1	95.2	2.37	2.21	2.65	16.5	20.9
	EST66764-12	Perpendicular	7.1	96.6	2.37	2.21	2.65	16.3	20.9
	EST66764-14	Perpendicular	7.1	95.5	2.37	2.21	2.65	16.4	20.9
	EST66723-11	Perpendicular	7.0	91.2	2.37	2.21	2.66	17.0	20.8
	EST66723-12	Perpendicular	7.0	91.6	2.37	2.21	2.66	16.9	20.8
	EST66723-15	Perpendicular	7.0	91.4	2.37	2.21	2.66	17.0	20.8
	EST66723-16	Perpendicular	7.0	91.1	2.37	2.21	2.66	17.0	20.8
	EST66723-17	Perpendicular	7.0	91.7	2.37	2.21	2.66	16.9	20.8
	EST66723-18	Perpendicular	6.9	91.9	2.37	2.22	2.66	16.7	20.8

w = water content,  $S_i$  = initial liquid saturation degree,  $\rho_{nat.}$  = natural density,  $\rho_d$  = dry density,  $\rho_s$  = density of solid grains,  $n_t$  = total porosity,  $CaCO_3$  = calcium carbonate content

Table 2 - References of the different boreholes and core samples used for the triaxial creep tests and physical parameters.

Borehole	Core sample	Orientation	w (%)	$S_i$ (%)	$\rho_{nat.}$ (g/cm <sup>3</sup> )	$\rho_d$ (g/cm <sup>3</sup> )	$\rho_s$ (g/cm <sup>3</sup> )	$n_t$ (%)	CaCO <sub>3</sub> (%)
PGZ3004 Cells with vacuum aluminium foil	EST66728-7	Parallel	7.3	88.9	2.37	2.21	2.70	18.1	22.5
	EST66728-3	Parallel	7.3	82.6	2.34	2.18	2.70	19.3	22.5
	EST66728-6	Parallel	7.3	88.9	2.38	2.21	2.70	18.1	22.5
	EST66728-1	Parallel	7.3	84.6	2.35	2.19	2.70	18.9	22.5
	EST66728-15	Perpendicular	7.3	84.6	2.35	2.19	2.70	18.9	22.5
	EST66728-14	Perpendicular	7.3	84.6	2.35	2.19	2.70	18.9	22.5
	EST66728-16	Perpendicular	7.3	88.9	2.37	2.21	2.70	18.1	22.5
	EST66728-11	Perpendicular	7.3	84.6	2.35	2.19	2.70	18.9	22.5

w = water content,  $S_i$  = initial liquid saturation degree,  $\rho_{nat.}$  = natural density,  $\rho_d$  = dry density,  $\rho_s$  = density of solid grains,  $n_t$  = total porosity,  $CaCO_3$  = calcium carbonate content

## 2.2.2 Experimental device and procedures

### 2.2.2.1 Experimental device

Conventional triaxial cells equipped with heating collars were used for the tests. The experimental device is shown in Figure 2. This device is composed of a pump for the application of the confinement

pressure and a 100 kN mechanical press for the application of the axial stress. Both are controlled by a dedicated system. The temperature is applied with heating collars around the triaxial cell and controlled by a regulator and a thermo-couple placed inside the cell. It is worth emphasizing that this thermocouple measures the temperature of the confining oil, not of the sample. Therefore, it is not possible to verify if the temperature is equilibrated in the sample.

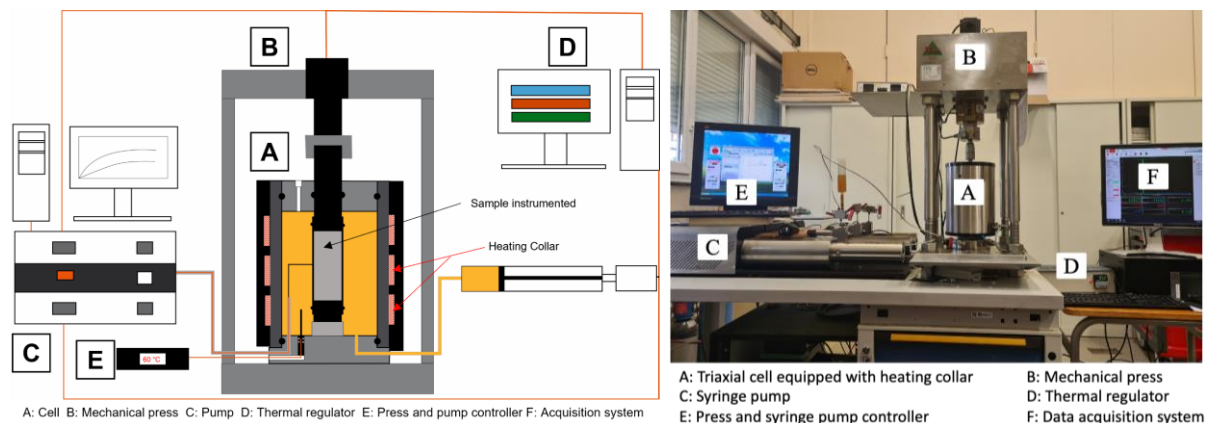


Figure 2 - Sketch and photo of the experimental apparatus.

### 2.2.2.1 Experimental procedures

#### Short-term compression tests

The specimens were tested under uniaxial and triaxial conditions. In the latter case, the confining pressure  $P_c$  is equal to 4 or 12 MPa and is applied with oil pressure at a rate of 0.1 MPa/min. In both cases (uniaxial and triaxial conditions), the samples are put in a Viton<sup>®</sup> jacket and placed in the triaxial cell. First, the selected confining pressure is applied (0, 4 or 12 MPa). Then, the entire test cell is heated until the desired temperature is reached at a constant heating rate of 50 °C/h. The tested temperatures for the two samples orientations (parallel and perpendicular to the bedding plane) are  $T = 20$  (room temperature), 40, 60, 80, 100 and 150 °C. Once the selected temperature is reached, a waiting time of 14 hours is imposed to allow temperature equilibrium inside the sample and dissipation of pore water overpressure (due to thermal expansion) before the deviatoric loading. Indeed, the coefficient of thermal expansion of water is an order of magnitude greater than that of solid grains in the CO<sub>x</sub> claystone (Mohajerani 2011), which can induce water overpressure during heating. Water overpressure can dissipate in the pores filled by air (samples are a little unsaturated initially as shown in Tab. 1) and then in the drainage holes designed in the center of the pistons (steel plates) at both sample ends. Then, the deviatoric loading is applied under controlled displacement at a speed of 0.2 μm/s ( $5 \cdot 10^{-6}$ /s considering the sample height) for the axial displacement of the mechanical press platens. Unloading-reloading cycles are performed during each test to follow the evolution of the elastic coefficients of the samples during the deviatoric loading with a relaxation time of 15 minutes before each unloading. At least one compression test is performed for each sample orientation, confining pressure and temperature.

In addition, to study the impact of the thermal loading rate and the waiting time (before the mechanical compression) on pore water overpressure in the samples and then mechanical results, the uniaxial compression test and the triaxial compression test at  $P_c = 4$  MPa with parallel orientation and a temperature of 80 °C were performed under three different conditions:

- thermal loading rate at 50 °C/hour until 80 °C, waiting time of 14 hours,
- thermal loading rate at 50 °C/hour until 80 °C, waiting time of only 1 hour,

- thermal loading rate at only 1 °C/hour until 80 °C, waiting time of 1 hour.

The thermo-mechanical path for the short-term compression tests is illustrated in the figure 3.

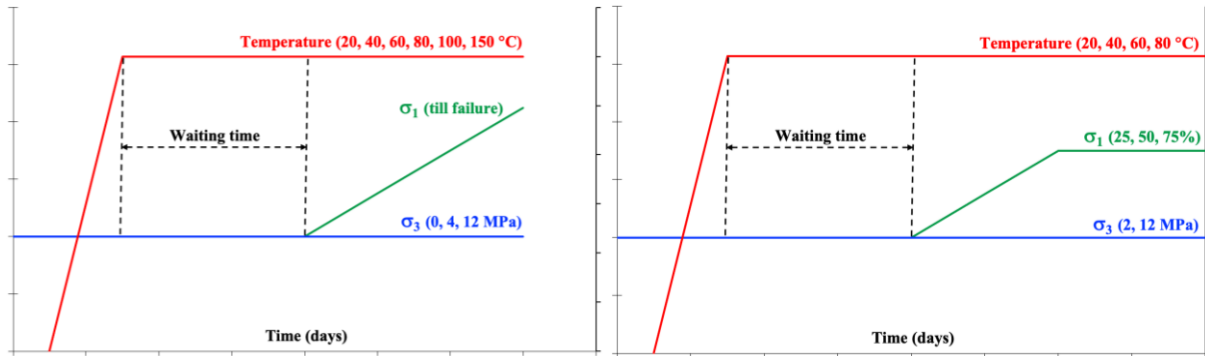


Figure 3 – Thermo-mechanical path for the short-term compression tests ( $\sigma_3$ : confining pressure,  $\sigma_1$ : axial stress) at the left and for the creep tests at the right.

To verify if conditions are drained or undrained during the deviatoric compression tests, one can use the solution given by Coussy (2004) or Cheng (2016) for this quasistatic problem of poroelasticity. It is worth emphasizing that this solution applies for the saturated case, which is not our case. The over-pressurization of the saturating fluid due to an extra loading vanishes, due to the diffusion process of the fluid towards the sample boundaries which remain drained. The characteristic time  $t_c$  for the dissipation of the pore pressure throughout the specimen writes as a function of the consolidation coefficient  $c$ :

$$t_c = \frac{L_c^2}{c} \quad c = \kappa M \frac{\lambda + 2\mu}{\lambda + 2\mu + b^2 M} \quad \kappa = \frac{k}{\eta} \quad b = 1 - \frac{K}{K_s} \quad M = \frac{K_u - K}{b^2} \quad (4)$$

Where  $L_c$  the characteristic length, is the largest distance that the pore pressure diffusion front needs to travel,  $k$  is the intrinsic permeability of the tested claystone =  $10^{-20}$  m<sup>2</sup> (mean value obtained from M’Jahad 2012; Homand et al. 2004; Grgic et al. 2023),  $\kappa$  is the permeability coefficient (or mobility coefficient),  $\eta$  is the fluid dynamic viscosity =  $1 \times 10^{-3}$  kg.m<sup>-1</sup>.s<sup>-1</sup>,  $K$  is the drained bulk modulus =  $3.2 \times 10^9$  Pa (mean value obtained from Escoffier 2002),  $K_u$  is the undrained bulk modulus =  $11.4 \times 10^9$  Pa (mean value obtained from Escoffier 2002),  $b$  is the Biot’s coefficient = 0.9 (mean value obtained from Belmokhtar et al. 2016; Wang et al. 2022),  $M$  is the Biot’s modulus =  $10.1 \times 10^9$  Pa (obtained from Eq. 4),  $\lambda$  and  $\mu$  are the drained Lamé coefficients  $\sim 6.6 \times 10^9$  Pa (mean values obtained from our mechanical tests at 20 °C).

Then, the consolidation coefficient  $c$  is equal to  $\sim 7 \times 10^{-8}$  m<sup>2</sup>.s<sup>-1</sup>. For uniaxial conditions, the characteristic length  $L_c$  is equal to the cylindrical core radius (0.01 m) and the characteristic time of diffusion  $t_c$  is equal to  $\sim 25$  min. For triaxial conditions, the characteristic length  $L_c$  is equal to half length of the core (0.02 m) and the characteristic time of diffusion  $t_c$  is equal to  $\sim 95$  min. The duration of the experiments, measured at the peak stress, depends on the confining pressure and the temperature: 0.8h for the uniaxial compression test with the shortest duration and 6h for the triaxial compression test with confining pressure  $P_c = 12$  MPa with the longest duration (Tab. 3). In analytic poroelastic solutions, the fluid flow is close to the stationary state when  $t = t_c$  (see among others Coussy 2004; Cheng 2016), which corresponds to the drained case (= asymptotic solution of the fluid pressure). Therefore, since  $t_c$  is not significantly lower than the duration of the experiments, one cannot consider that conditions are perfectly drained during the compression tests, especially since a ramp loading is continuously applied on the samples from the beginning of the test till the end. Actually, our compression tests are performed on unsaturated samples under the so-called pseudo-drained condition with the drainage circuit of pore fluid open and connected to the atmospheric pressure, as

for the similar study on the same claystone of Liu et al. (2019). Indeed, with respect to the small size of samples, the selected strain rate ( $5 \cdot 10^{-6}/s$ ) is considered as slow enough to avoid significant over-pressurization of the pore fluid, especially since samples are unsaturated (cf. Tab. 1) and contain therefore compressible gas.

#### Long-term compression tests (multi-step triaxial creep tests)

The specimens were tested under triaxial conditions, with a confining pressure  $P_c$  equal to 2 or 12 MPa applied with oil pressure at a rate of 0.1 MPa/min. The samples are put in a Viton® jacket and placed in the triaxial cell. First, the selected confining pressure is applied (2 or 12 MPa). Then, the entire test cell is heated until the desired temperature is reached at a constant heating rate of 50 °C/h. The tested temperatures for the two samples orientations (parallel and perpendicular to the bedding plane) are  $T = 20$  (room temperature), 40, 60, and 80°C. Once the selected temperature is reached, a waiting time of one day approximately is imposed to allow temperature equilibrium inside the sample and dissipation of pore water overpressure (due to thermal expansion) before the deviatoric loading. Then, the deviatoric loading is applied under controlled force at a speed of 0.002MPa/s.

For each multi-step creep test, 3 deviatoric stress levels will be applied successively on the sample and each creep stage will last one month (at least). The 3 deviatoric stress levels correspond to 25%, 50% and 75% of the short-term peak strength. The short-term peak strength is determined at 20 °C for each orientation (parallel and perpendicular to the bedding plane) and each confining pressure (2 and 12 MPa), from cylindrical core samples taken in the same drill core used to obtain the cylindrical core samples for the creep tests. These tests are called reference triaxial compression tests. The short-term peak strengths values obtained from these reference triaxial compression tests (at 20 °C) and the corresponding deviatoric stress levels are:

Parallel orientation,  $P_c = 2$  MPa: 19.8 MPa → 25% ~5 MPa ; 50% ~10 MPa ; 75% ~15 MPa

Parallel orientation,  $P_c = 12$  MPa: 53.2 MPa → 25% ~13.5 MPa ; 50% ~26.5 MPa ; 75% ~40 MPa

Perpendicular orientation,  $P_c = 2$  MPa: 22.2 MPa → 25% ~5.5 MPa ; 50% ~11 MPa ; 75% ~16.5 MPa

Perpendicular orientation,  $P_c = 12$  MPa: 46.0 MPa → 25% ~11.5 MPa ; 50% ~23 MPa ; 75% ~34.5 MPa

The thermo-mechanical path for creep tests is illustrated in the figure 3.

In order to follow the evolution of the elastic coefficients of the samples, an unloading-reloading cycle is performed before and after each deviatoric stress level and at the end of the last (third) stress level if the sample hasn't reach long-term failure (accelerated or tertiary creep).

### 2.2.3 Research plan

The experimental conditions for all short-term compression tests and triaxial creep tests are summarized in Tables 3 and 4 respectively.

Table 3 - References of the different samples for short-term compression tests, experimental conditions (the thermal loading corresponds to the rate of temperature increase + the waiting time before the mechanical test), peak strength (deviatoric stress at peak), post-mortem water content *w* and test duration at failure (i.e., at peak stress).

Sample	Orientation	T (°C)	Thermal loading	Pc (MPa)	Peak strength (MPa)	Post-mortem <i>w</i> (%)	Test duration (h)
EST66420-3	Parallel	20	50 °C/h +14 h	0	19.9		1.6
EST66421-1	Parallel	40	50 °C/h +14 h	0	9.4		1.0
EST66420-1	Parallel	60	50 °C/h +14 h	0	7.9		0.8
EST66421-3	Parallel	80	50 °C/h +14 h	0	6.9		1.1
EST66421-8	Parallel	80	1 °C/h +1 h	0	8.3		0.8
EST66421-2	Parallel	80	50 °C/h +1 h	0	10.4		1.3
EST66420-2	Parallel	100	50 °C/h +14 h	0	7.6		1.1
EST66418-4	Parallel	150	50 °C/h +14 h	0	22.8	1.3	2.3
EST66420-4	Parallel	20	50 °C/h +14 h	4	28.0		2.2
EST66721-4	Parallel	20	50 °C/h +14 h	4	29.1	6.7	3.1
EST66421-4	Parallel	40	50 °C/h +14 h	4	28.4		3.3
EST66420-5	Parallel	60	50 °C/h +14 h	4	27.0		2.3
EST66421-6	Parallel	80	50 °C/h +14 h	4	27.8		3.6
EST66721-1	Parallel	80	50 °C/h +14 h	4	27.9	6.6	3.1
EST66721-3	Parallel	80	1 °C/h +1 h	4	29.1	6.6	3.0
EST66721-2	Parallel	80	50 °C/h +1 h	4	26.5	6.2	3.0
EST66420-7	Parallel	100	50 °C/h +14 h	4	28.8		2.7
EST66420-8	Parallel	150	50 °C/h +14 h	4	44.7		2.7
EST66418-9	Parallel	150	50 °C/h +14 h	4	55.2	1.5	3.5
EST66723-1	Parallel	20	50 °C/h +14 h	12	49.5	6.4	5.6
EST66723-10	Parallel	20	50 °C/h +14 h	12	43.0	6.3	5.2
EST66723-2	Parallel	40	50 °C/h +14 h	12	46.0	6.4	6.0
EST66723-3	Parallel	60	50 °C/h +14 h	12	43.2	6.7	5.5
EST66723-4	Parallel	80	50 °C/h +14 h	12	38.2	6.2	4.9
EST66723-8	Parallel	80	50 °C/h +14 h	12	38.9	6.2	4.9
EST66723-6	Parallel	100	50 °C/h +14 h	12	32.5	6.0	3.8
EST66723-9	Parallel	100	50 °C/h +14 h	12	34.8	6.0	3.8
EST66723-7	Parallel	150	50 °C/h +14 h	12	49.9	2.0	5.4
EST66760-11	Perpendicular	20	50 °C/h +14 h	0	16.7		3.6
EST66762-11	Perpendicular	40	50 °C/h +14 h	0	14.4	6.5	2.8
EST66760-12	Perpendicular	60	50 °C/h +14 h	0	14.9		1.9
EST66762-13	Perpendicular	80	50 °C/h +14 h	0	13.3	6.7	2.4
EST66760-13	Perpendicular	100	50 °C/h +14 h	0	12.0		2.1
EST66764-11	Perpendicular	150	50 °C/h +14 h	0	16.4	1.2	2.4
EST66760-14	Perpendicular	20	50 °C/h +14 h	4	25.0		3.3
EST66762-14	Perpendicular	40	50 °C/h +14 h	4	23.6	6.9	3.8
EST66760-16	Perpendicular	60	50 °C/h +14 h	4	24.3		2.8
EST66762-15	Perpendicular	80	C +14 h	4	21.6	6.6	2.8
EST66760-15	Perpendicular	100	50 °C/h +14 h	4	19.4		1.7
EST66764-12	Perpendicular	150	50 °C/h +14 h	4	24.5	2.4	2.7
EST66764-14	Perpendicular	20	50 °C/h +14 h	12	28.6	6.9	3.7
EST66723-18	Perpendicular	20	50 °C/h +14 h	12	33.4	6.7	4.6
EST66723-12	Perpendicular	40	50 °C/h +14 h	12	31.0	6.7	4.6
EST66723-11	Perpendicular	60	50 °C/h +14 h	12	28.8	6.8	3.6
EST66723-17	Perpendicular	80	50 °C/h +14 h	12	27.1	6.4	4.0
EST66723-15	Perpendicular	100	50 °C/h +14 h	12	24.2	6.1	3.2
EST66723-16	Perpendicular	150	50 °C/h +14 h	12	36.9	2.4	4.1

Table 4 - References of the different samples used for triaxial creep tests, experimental conditions (temperature, thermal loading confining pressure  $P_c$ ), peak strength (deviatoric stress at peak) and test duration.

Sample	Orientation	T (°C)	Thermal loading	$P_c$ (MPa)	Peak strength (MPa)	Test duration (d)
<b>Reference (short-term) triaxial compression tests</b>						
EST66728-7	Parallel	20	-	2	19.8	-
EST66728-3	Parallel	20	-	12	53.2	-
EST66728-15	Perpendicular	20	-	2	22.2	-
EST66728-14	Perpendicular	20	-	12	46.0	-
<b>Multi-step triaxial creep tests</b>						
EST66728-6	Parallel	20	-	2		88.4
EST66728-16	Perpendicular	20	-	2	16.5 (75%)	70.1
EST66728-1	Parallel	20	-	12		113.8
EST66728-11	Perpendicular	20	-	12	23 (50%)	39.4
EST66728-5	Parallel	80	150 °C/h + 24 h	12		96.6
EST66728-13	Perpendicular	80	150 °C/h + 24 h	12	11.5 (25%)	33.8

## 2.3 Results and discussion

### 2.3.1 Experimental results

#### 2.3.1.1 Short-term compression tests

##### Stress-strains curves

The stress-strain curves of uniaxial and triaxial ( $P_c = 4$  and 12 MPa) tests for parallel orientation under different temperatures are presented in Figs 4, 5 and 6: axial ( $\epsilon_{11}$ ), lateral ( $\epsilon_{22}$  and  $\epsilon_{33}$ ) and volumetric ( $\epsilon_v$ ) strains measured by the strain gages. In the same way, Figs. 7, 8 and 9 represent the results of uniaxial and triaxial ( $P_c = 4$  and 12 MPa) tests for perpendicular orientation under different temperatures. Unfortunately, sometimes strain gages didn't work and deformation data are missing for some samples.

First, we observe that for the uniaxial tests performed in the parallel direction (Fig. 4), the volumetric deformation is contractant at 20 °C and becomes progressively dilatant at higher temperatures. This is well illustrated in a graph of this Figure that represents only the volumetric deformations of these samples. Concerning the triaxial tests with a confining pressure of 4 MPa and 12 MPa in the parallel direction (Figs. 5 and 6), the behaviour remains overall contractant whatever the temperature, which is probably due to the action of the confining pressure.

Second, concerning the uniaxial tests performed in the perpendicular direction (Fig. 7), the volumetric deformation is always very contractant, whatever the temperature. Also, the axial deformations are more significant than for the parallel direction and the axial strain curves are very curved at the beginning of the loading. Concerning the triaxial tests with a confining pressure of 4 MPa and 12 MPa in the perpendicular direction (Figs. 8 and 9), the volumetric deformation is still very contractant, whatever the temperature. The axial strain curves are not curved at the beginning of the loading, compared to the uniaxial tests.

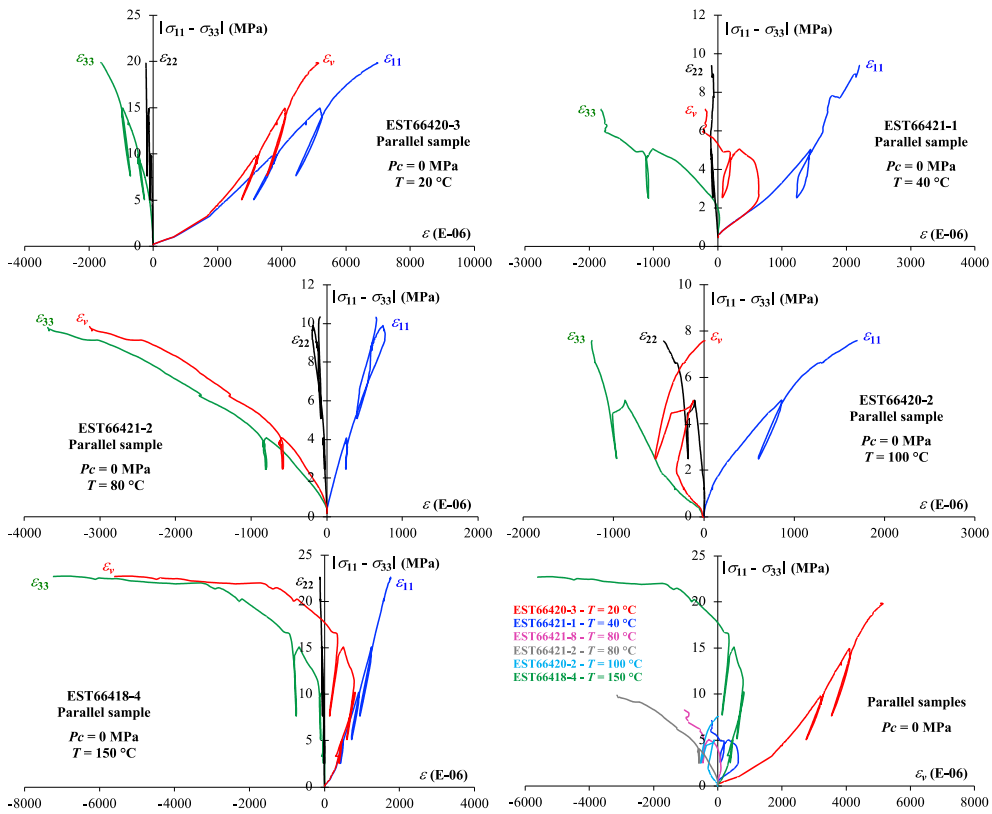


Figure 4 - Stress-strain curves of uniaxial tests ( $P_c = 0$  MPa) at different temperatures of samples cored in the direction parallel to the bedding plane.

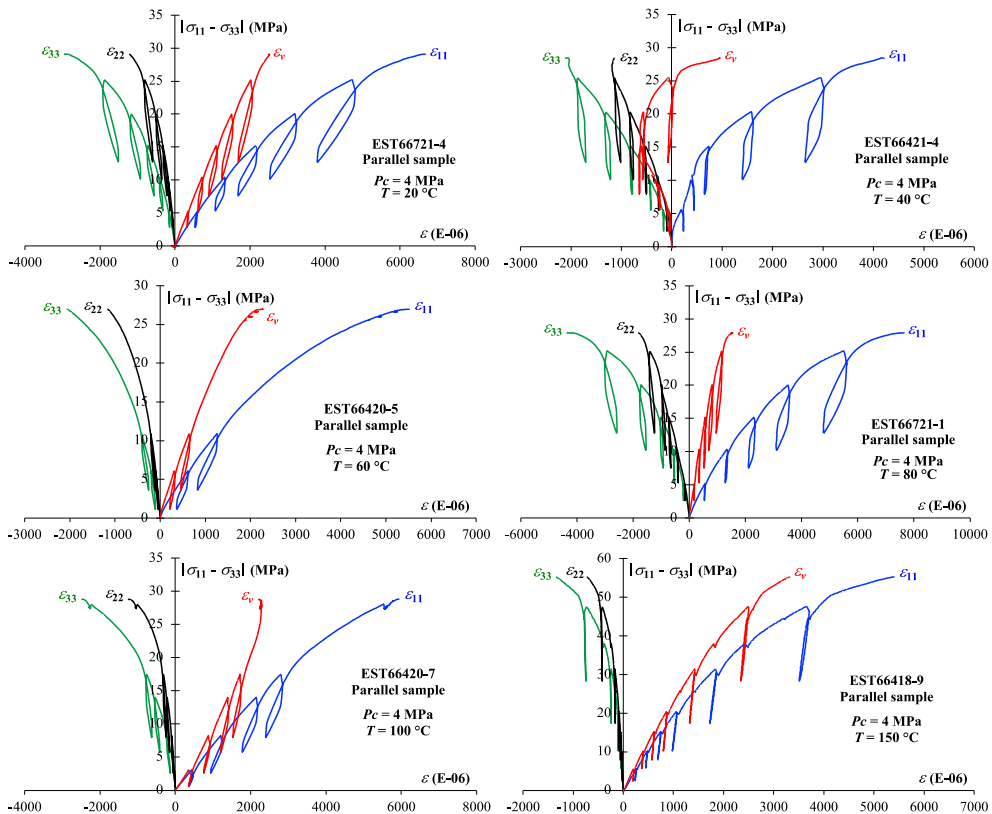


Figure 5 - Stress-strain curves of triaxial tests at  $P_c = 4$  MPa, at different temperatures of samples cored in the direction parallel to the bedding plane.

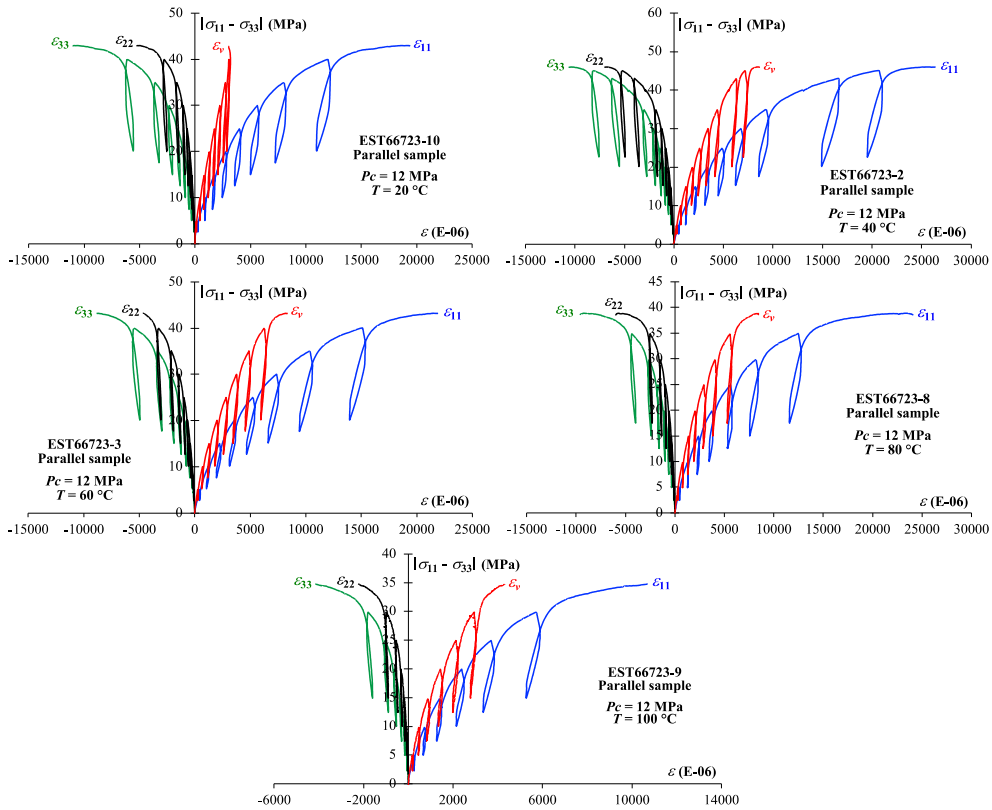


Figure 6 - Stress-strain curves of triaxial tests at  $P_c = 12$  MPa, at different temperatures of samples cored in the direction parallel to the bedding plane.

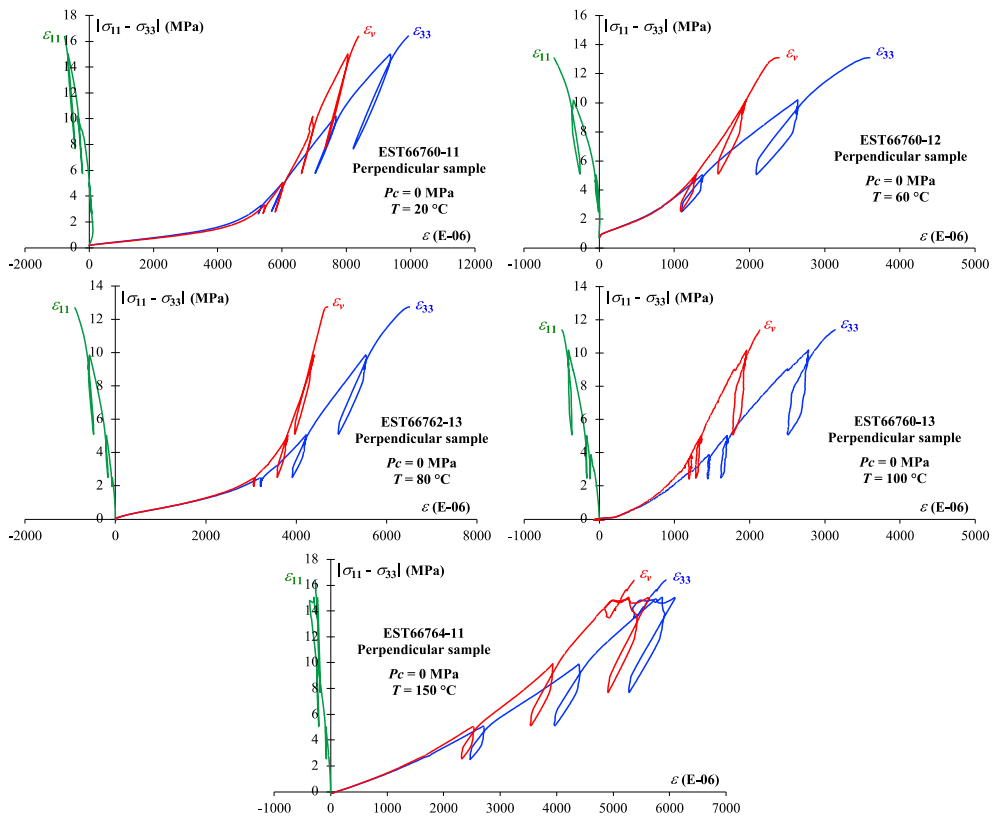


Figure 7 - Stress-strain curves of uniaxial tests ( $P_c = 0$  MPa) at different temperatures of samples cored in the direction perpendicular to the bedding plane.

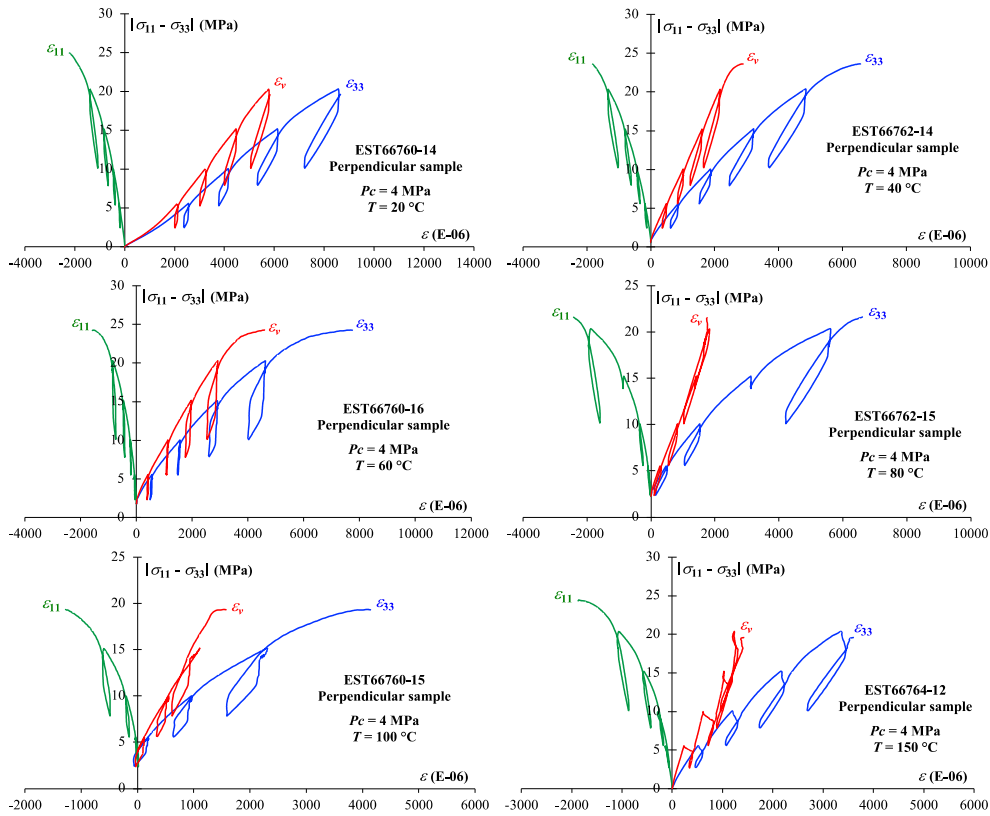


Figure 8 - Stress-strain curves of triaxial tests at  $P_c = 4$  MPa, at different temperatures of samples cored in the direction perpendicular to the bedding plane.

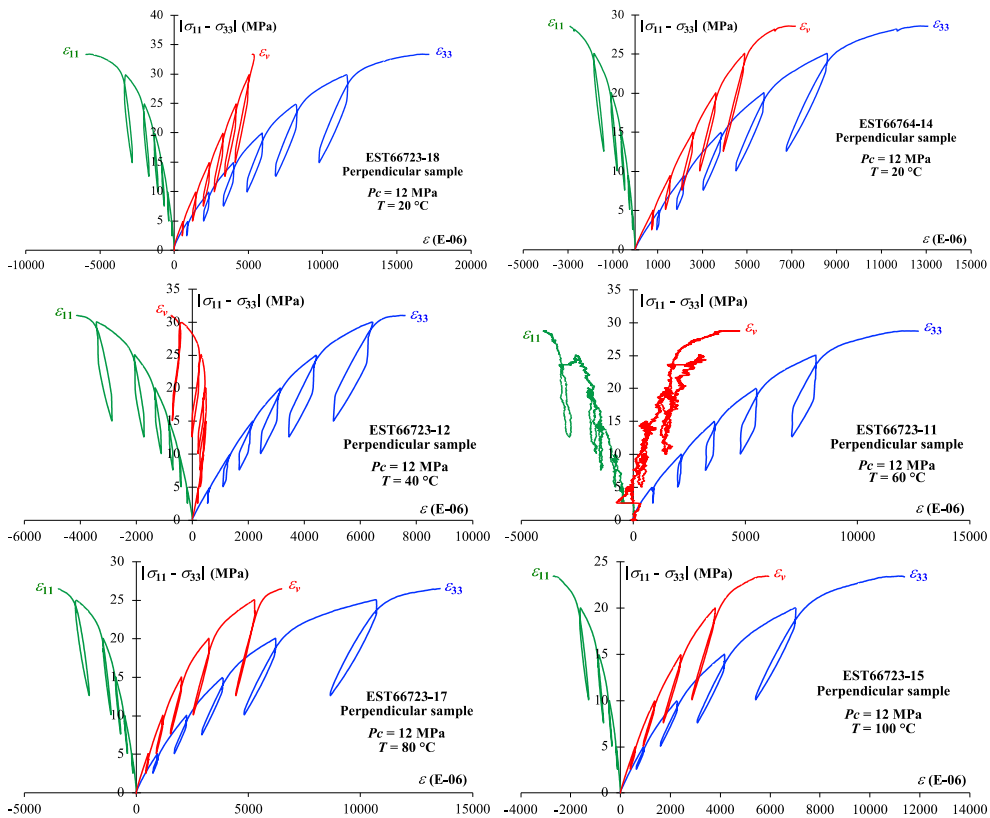


Figure 9 - Stress-strain curves of triaxial tests at  $P_c = 12$  MPa, at different temperatures of samples cored in the direction perpendicular to the bedding plane.

### Mechanical properties

The deviatoric stress at peak (peak strength) is given in the Table 2 for all tested sample. The Figure 10 represents the evolution of the deviatoric stress at peak (peak strength) as a function of temperature for parallel and perpendicular orientations and for all confining pressures (0, 4 and 12 MPa), with polynomial (3rd order) fitting curves. Only the tests with a thermal loading rate at 50 °C/hour and a waiting time of 14 hours were represented in this Figure in order to make comparisons more relevant. It is worth emphasizing that reliability and representativity of the experimental results can be affected by the material heterogeneity (due to the variations in the minerals proportions between the different drill cores and the presence of bedding planes) and the sampling (conservation of drill cores). Then, the focus will be put here on the tendencies.

For the parallel direction, uniaxial tests showed an overall significant decrease in the peak strength until 80-100 °C (mainly between 20 °C and 40 °C) and then a very significant increase for 150 °C. Under triaxial condition with  $P_c = 4$  MPa, the peak strength barely changes until 100 °C but there is a significant increase for 150 °C. Under triaxial condition with  $P_c = 12$  MPa, the peak strength shows a decreasing trend until 100 °C (mainly between 40 °C and 100 °C) despite the scattering of some experimental results (mainly at 20 °C) due to the material heterogeneity, and then also increases significantly for 150 °C. For the perpendicular direction, one can observe for uniaxial and triaxial conditions ( $P_c = 4$  and 12 MPa) a moderate and progressive decrease in the peak strength with the increase in temperature until 100 °C, and then a significant increase for 150 °C. Therefore, temperature has globally a negative impact on the resistance to failure of the COx claystone, and this impact depends on both confining pressure and sample orientation (parallel or perpendicular to the bedding plane).

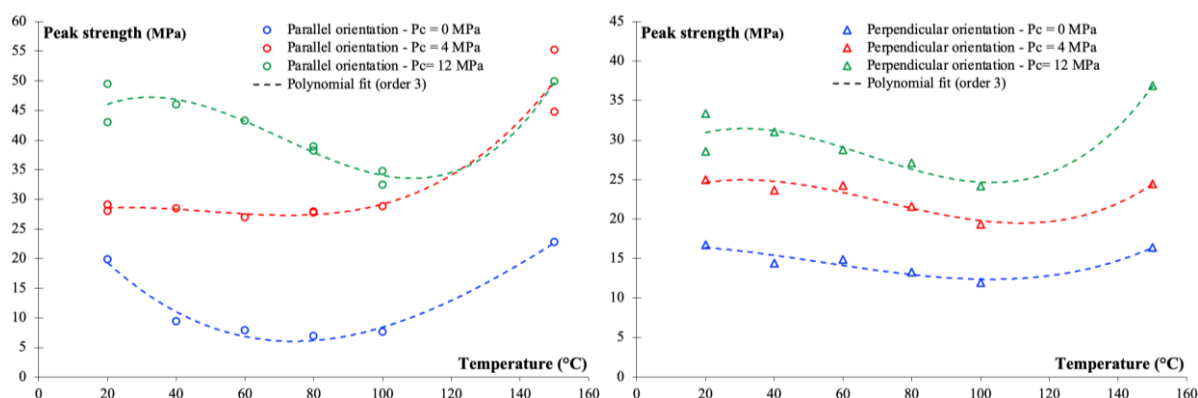


Figure 10 - Evolution of the deviatoric stress at peak (peak strength) as a function of temperature for parallel (left) and perpendicular (right) orientations and for all confining pressures (0, 4 and 12 MPa), with polynomial (3rd order) fitting.

Thanks to the unloading-reloading cycles, we were able to calculate the elastic coefficients at different stress levels. Unfortunately, sometimes strain gages didn't work and it wasn't always possible to do that; then some data are missing for some samples. Moreover, for uniaxial conditions, due to the low peak strength for some samples, it was not possible to always perform a lot of unloading-reloading cycles. Elastic coefficients were determined from the slope of unloading-reloading curves (with the secant method), which was not always easy due to the fact that these curves are not always linear. Then, the uncertainty of the coefficients values is sometimes significant and the emphasize will be more on the trends.

Figures 11 and 12 represent the evolution of the elastic coefficients (axial Young's modulus  $E_{11}$  and Poisson coefficients  $\nu_{13}$  and  $\nu_{12}$ ) as a function of the deviatoric stress (normalized with the deviatoric stress at peak) for the parallel orientation and for all confining pressures (0, 4 and 12 MPa). When the deviatoric stress increases, the axial Young's modulus  $E_{11}$  decreases overall. Both Poisson's coefficients  $\nu_{13}$  (3 being the direction perpendicular to the surface of the clay minerals aligned along the bedding planes) and  $\nu_{12}$  increase overall with the deviatoric stress.  $\nu_{13}$  is systematically higher than  $\nu_{12}$ , which is a classical result for a transverse isotropic material. The axial Young's modulus  $E_{11}$  increases globally with the increase in confining pressure, which is a classical result for rocks. For uniaxial condition and triaxial condition at  $P_c = 4$  MPa (data for  $P_c = 12$  MPa are missing), there is a very significant increase in the axial Young's modulus  $E_{11}$  for the highest temperature (150 °C).

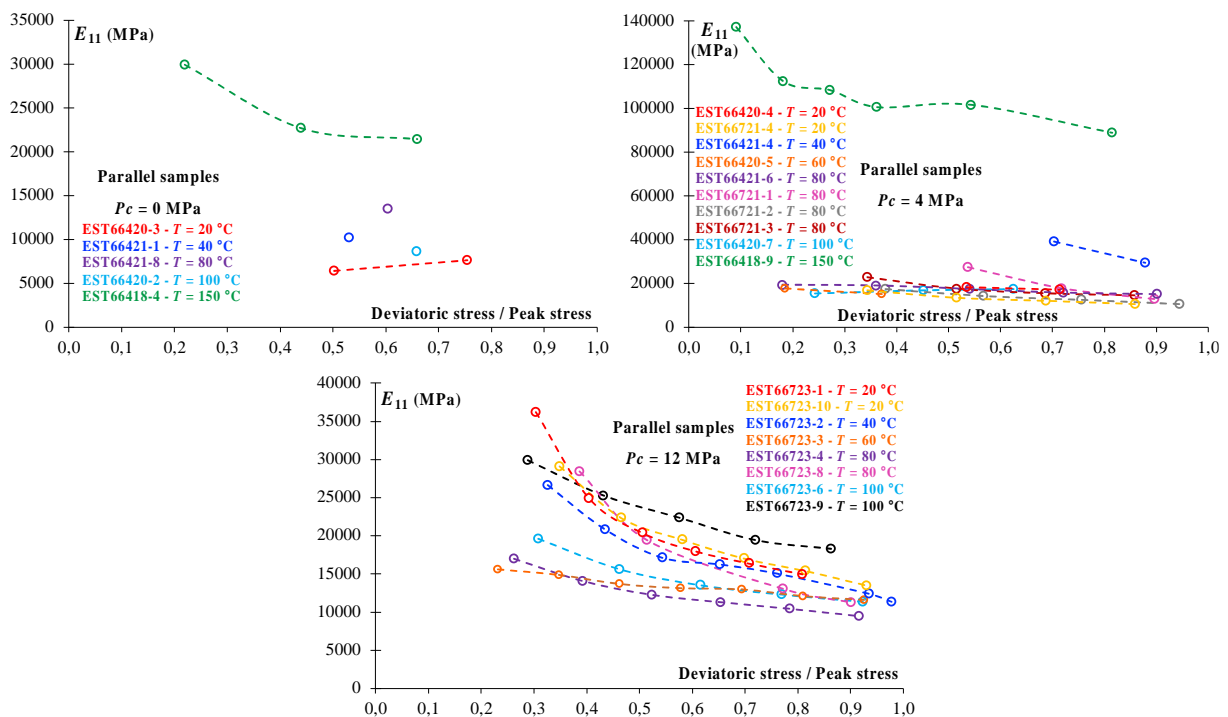


Figure 11 - Evolution of the axial Young's modulus  $E_{11}$  as a function of the deviatoric stress (normalized with the deviatoric stress at peak) at different temperatures and for all confining pressures - samples cored in the direction parallel to the bedding plane.

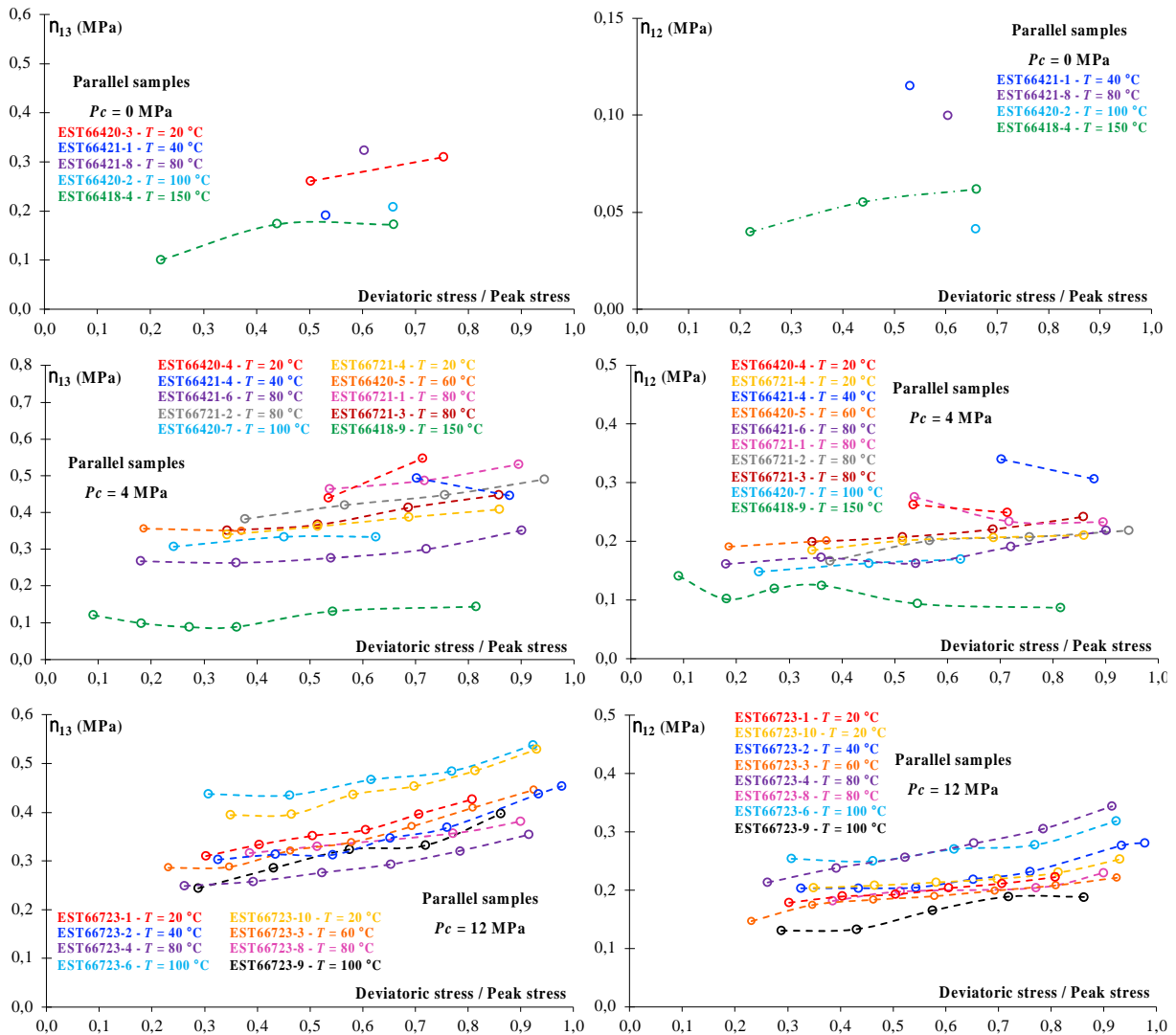


Figure 12 - Evolution of the Poisson's coefficients  $\nu_{13}$  and  $\nu_{12}$  as a function of the deviatoric stress (normalized with the deviatoric stress at peak) at different temperatures and for all confining pressures - samples cored in the direction parallel to the bedding plane.

The Figure 13 represents the evolution of the elastic coefficients (axial Young's modulus  $E_{33}$  and Poisson's coefficient  $\nu_{31}$ ) as a function of the deviatoric stress (normalized with the deviatoric stress at peak) for the perpendicular orientation and for all confining pressures (0, 4 and 12 MPa). When the deviatoric stress increases, the axial Young's modulus  $E_{33}$  decreases overall, whereas the Poisson's coefficient  $\nu_{31}$  (3 being the direction perpendicular to the bedding planes) increases. The axial Young's modulus  $E_{33}$  increases globally with the increase in confining pressure, as for the parallel orientation. There is no noticeable influence of temperature on the axial Young's modulus  $E_{33}$ .

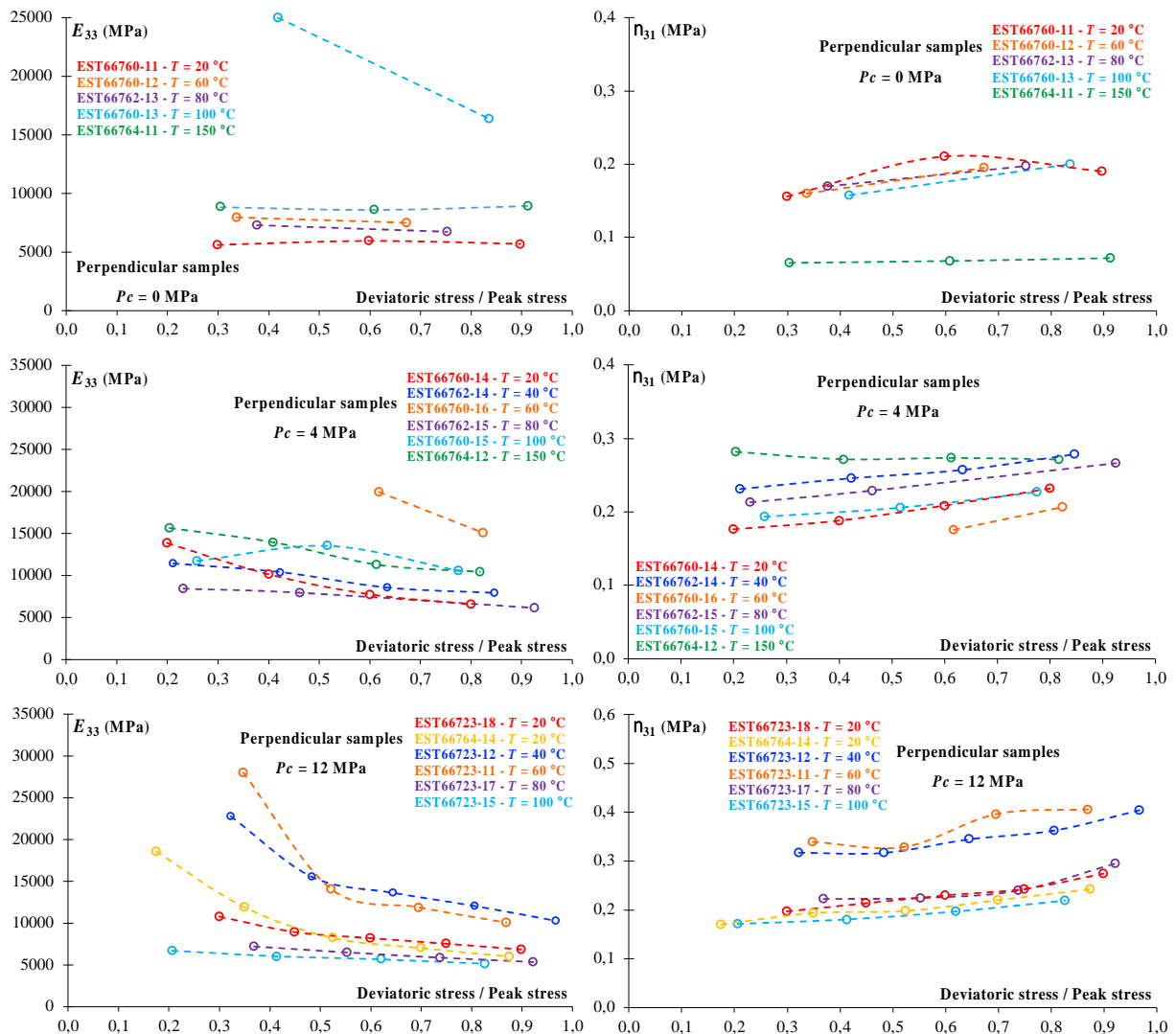


Figure 13 - Evolution of the elastic coefficients (axial Young's modulus  $E_{33}$  and Poisson's coefficient  $\nu_{31}$ ) as a function of the deviatoric stress (normalized with the deviatoric stress at peak) at different temperatures and for all confining pressures - samples cored in the direction perpendicular to the bedding plane.

### 2.3.1.2 Long-term triaxial compression tests (multi-step creep tests)

#### Creep curves (deformations vs time)

So far, only multi-step creep tests at  $T = 20\text{ °C}$  and  $P_c = 2$  and  $12\text{ MPa}$ , and at  $T = 80\text{ °C}$  and  $P_c = 12\text{ MPa}$ , for both parallel and perpendicular samples, were performed. Therefore, the impact of temperature on the creep properties and long-term strength of the COx claystone can be analysed only partially. The remaining multi-step creep tests are in progress.

Figures 14 and 15 represent the creep curves (axial, lateral and volumetric deformations vs time) for parallel and perpendicular samples for the different deviatoric stress levels (25%, 50% and 75% of the reference short-term peak strengths), at  $T = 20\text{ °C}$  and  $P_c = 2$  and  $12\text{ MPa}$ , respectively. Peak strength (deviatoric stress at peak) and test duration of each sample are indicated in Table 4.

For  $P_c = 2\text{ MPa}$ , the axial creep deformations are generally more important for the perpendicular sample orientation, probably due to the long-term closure of the bedding planes when the applied axial stress is perpendicular to the bedding planes. In addition, for the parallel sample orientation, the lateral

creep deformations  $\epsilon_{33}$  (3 being the direction perpendicular to the surface of the clay minerals aligned along the bedding planes) are generally much larger than the lateral creep deformations  $\epsilon_{11}$  of the perpendicular samples, probably due to the preferential opening of the bedding planes when the applied axial stress is parallel to the bedding planes. For the parallel sample orientation,  $\epsilon_{33}$  is much larger than  $\epsilon_{22}$ , which is also due to the preferential opening of the bedding planes. The consequence of these features is that the volumetric creep deformation is globally dilatant for the parallel sample orientation and contractant for the perpendicular sample orientation. The perpendicular sample reached the long-term failure (accelerated or tertiary creep) 12.5 days after the beginning of the last creep stress level (16.5 MPa, 75% of the reference short-term peak strength).

For  $P_c = 12$  MPa, the axial creep deformations are not more important for the perpendicular sample orientation, contrary to  $P_c = 2$  MPa, because the initial application of this high confining pressure (12 MPa) closed the bedding planes before the application of the first creep stress level. For the parallel sample orientation,  $\epsilon_{33}$  (3 being the direction perpendicular to the surface of the clay minerals aligned along the bedding planes) is much larger than  $\epsilon_{22}$ , which is due to the preferential opening of the bedding planes. Contrary to  $P_c = 2$  MPa, the lateral creep deformations  $\epsilon_{33}$  of the parallel samples are not that larger than the lateral creep deformations  $\epsilon_{11}$  of the perpendicular samples because of the action of the high confining pressure (12 MPa) which reduces the preferential opening of the bedding planes when the applied axial stress is parallel to the bedding planes. Then, the volumetric dilatation remains contractant for all stress levels and for both parallel and perpendicular sample orientations because of the action of the high confining pressure (12 MPa).

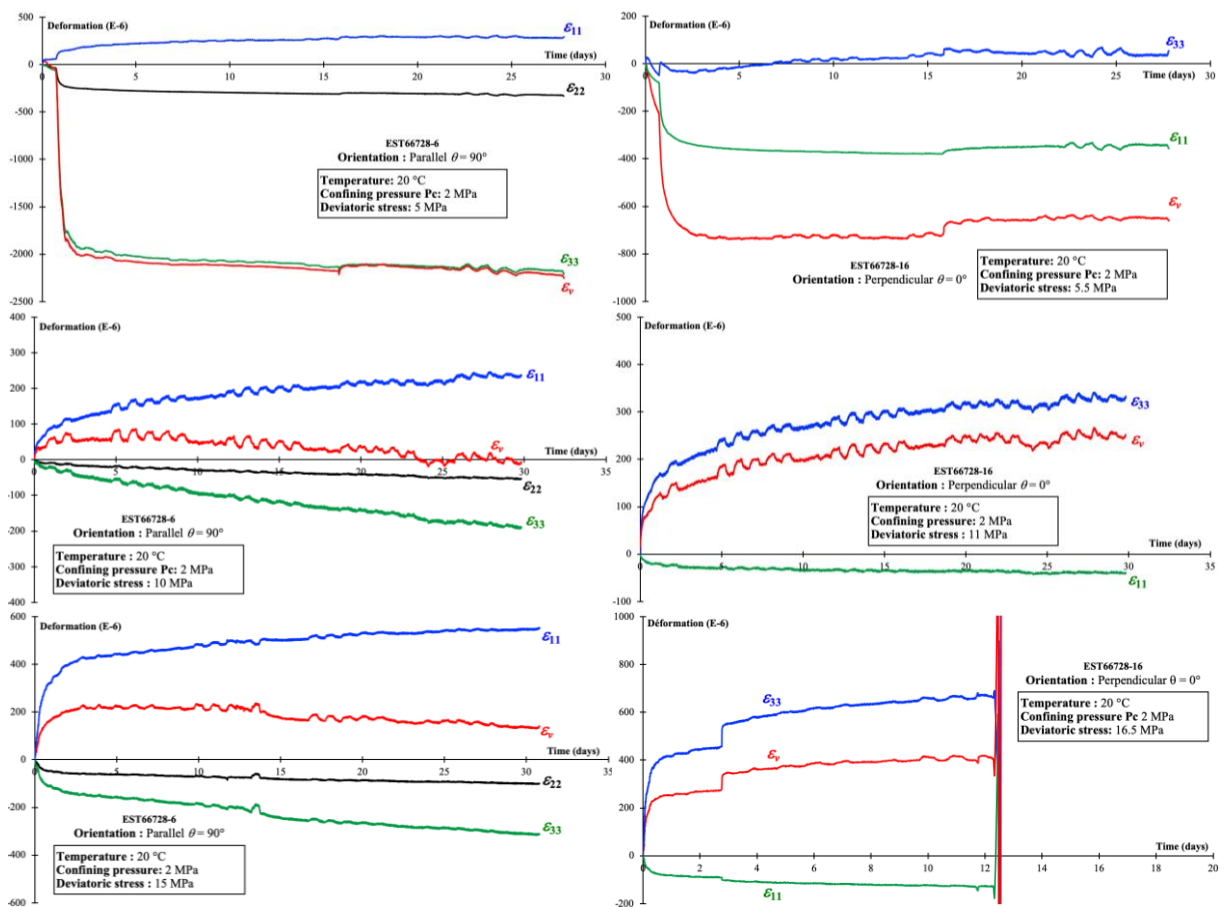


Figure 14 – Creep curves (deformations vs time) for parallel (EST66728-6) and perpendicular (EST66728-16) samples at  $P_c = 2$  MPa and  $T = 20$  °C for the different deviatoric stress levels (25%, 50% and 75% of the reference short-term peak strengths).

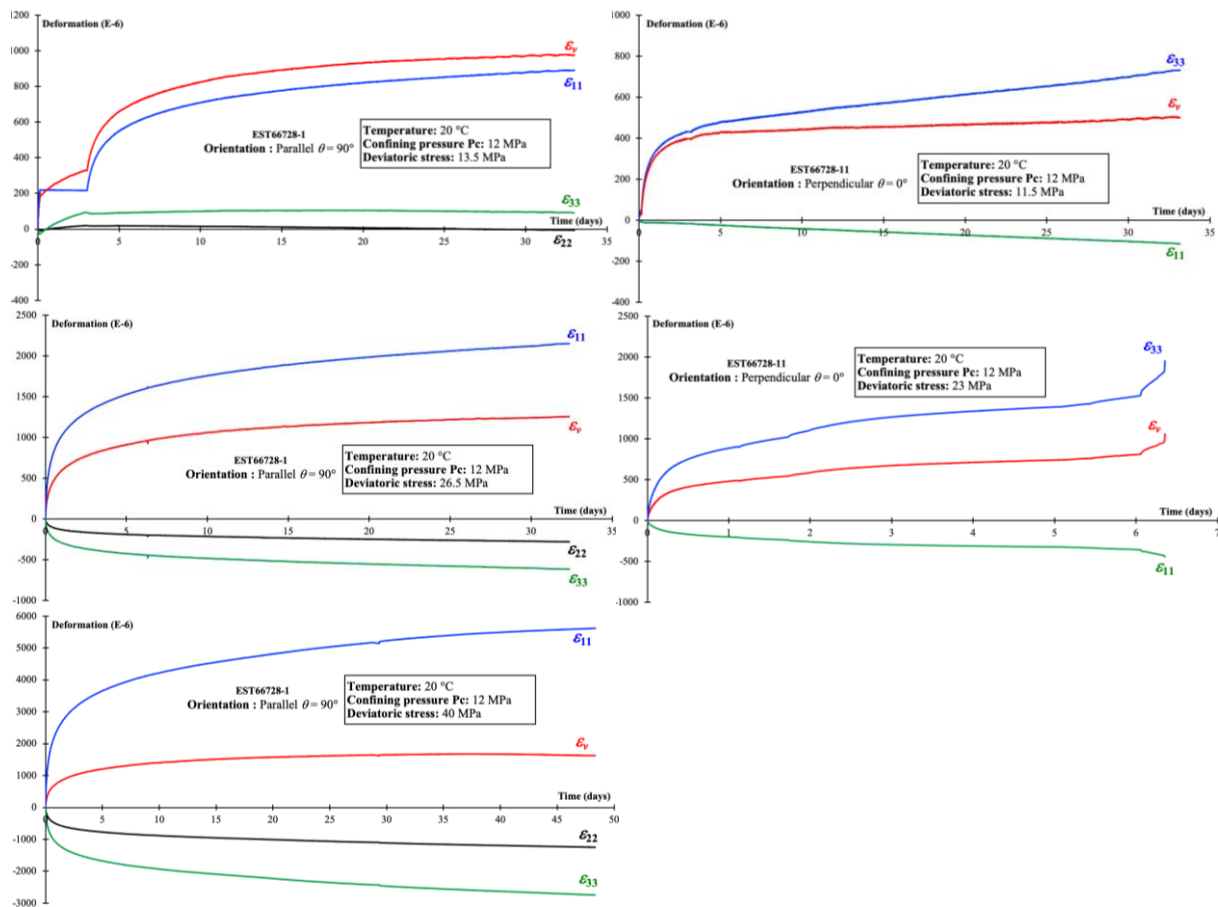


Figure 15 – Creep curves (deformations vs time) for parallel (EST66728-1) and perpendicular (EST66728-11) samples at  $P_c = 12 \text{ MPa}$  and  $T = 20 \text{ °C}$  for the different deviatoric stress levels (25%, 50% and 75% of the reference short-term peak strengths).

Figure 16 represents the creep curves (axial, lateral and volumetric deformations vs time) for parallel and perpendicular samples for the different deviatoric stress levels (25%, 50% and 75% of the reference short-term peak strengths), at  $T = 80 \text{ °C}$  and  $P_c = 12 \text{ MPa}$ . Peak strength (deviatoric stress at peak) and test duration of each sample are indicated in Table 4. These first results obtained at high temperature show an impact of temperature on the creep properties of the COx claystone. For the parallel orientation, creep deformations are larger for  $80 \text{ °C}$  than for  $20 \text{ °C}$  for all deviatoric stress levels. For the perpendicular orientation, creep deformations are also larger for  $80 \text{ °C}$  than for  $20 \text{ °C}$ . In addition, for  $T = 80 \text{ °C}$ , the failure was obtained at the 1<sup>st</sup> deviatoric stress level corresponding to only 25% of the short-term peak strength whereas the failure occurred at 50% of the short-term peak strength for  $T = 20 \text{ °C}$ . Therefore, long-term strength of COx claystone seems to decrease with temperature. This first result has obviously to be confirmed when all the creep tests at different temperatures will be finished.

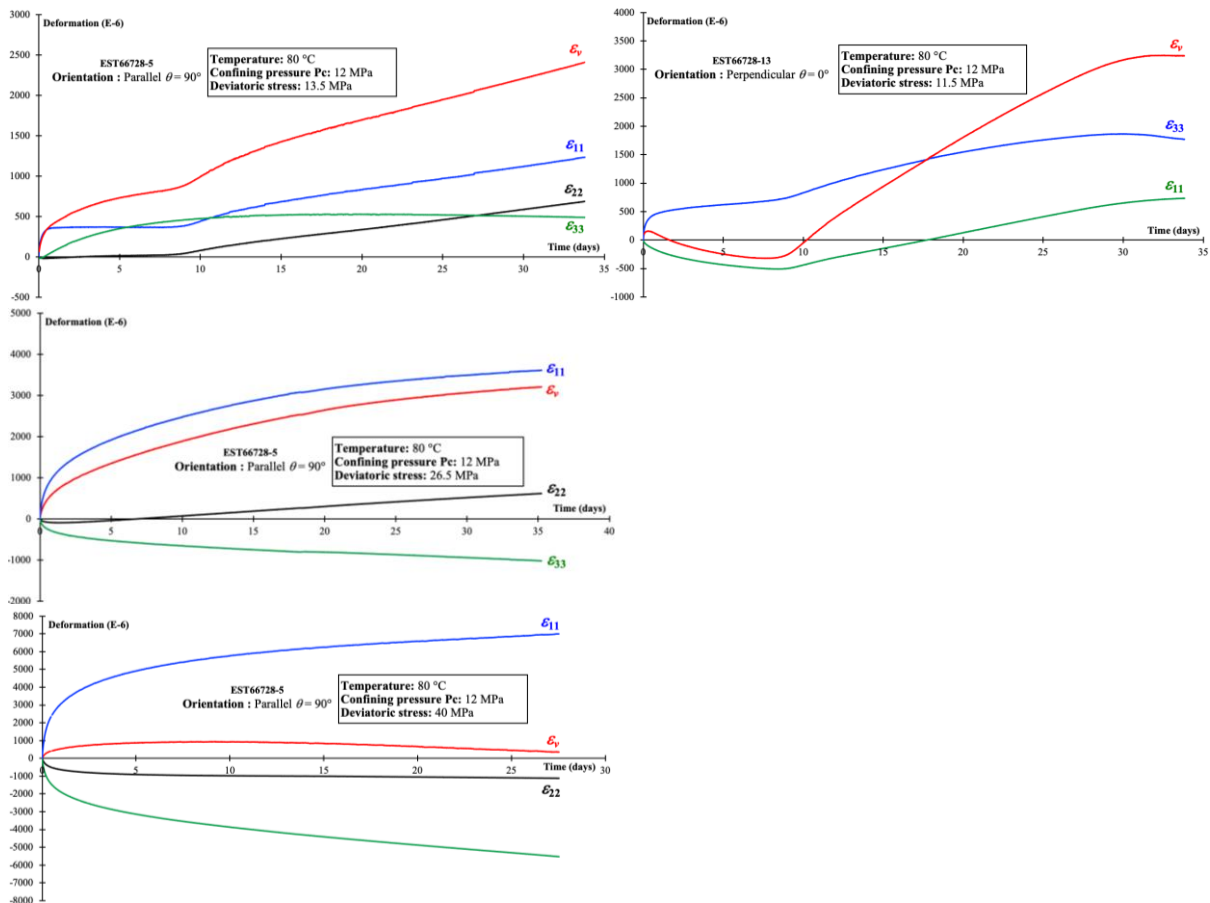


Figure 16 – Creep curves (deformations vs time) for parallel (EST66728-5) and perpendicular (EST66728-13) samples at  $P_c = 12$  MPa and  $T = 80$  °C for the different deviatoric stress levels (25%, 50% and 75% of the reference short-term peak strengths).

## 2.3.2 Discussion

So far, only multi-step creep tests at  $T = 20$  °C and  $P_c = 2$  and 12 MPa, and at  $T = 80$  °C and  $P_c = 12$  MPa, for both parallel and perpendicular samples, were performed. Therefore, the impact of temperature on the creep properties and long-term strength of the COx claystone can be analysed only partially, which has been done in the results section (2.3.1.2).

In this “Discussion” section, only results obtained short-term compression tests will be discussed.

### 2.3.2.1 Influence of temperature (until 100 °C) on the mechanical behaviour of the COx claystone

#### Material deformation and elastic coefficients

For the parallel orientation and all confining pressures (0, 4 and 12 MPa), there is an overall decrease in the axial Young’s modulus  $E_{11}$  and an increase in the Poisson’s coefficients  $\nu_{13}$  and  $\nu_{12}$  when the deviatoric stress increases, even though a lot of data are missing for the uniaxial conditions (Figs. 11 and 12). There is no noticeable impact of temperature up to 100 °C on these evolutions. This result is consistent with that of Menaceur et al. (2015) who also showed little changes of the elastic parameters (Young’s modulus and Poisson coefficient) with temperature (80 °C) from shear tests on the COx claystone in a hollow cylinder triaxial apparatus under fully drained conditions. Liu et al. (2019)

performed triaxial tests with lateral decompression at temperatures up to 90 °C and also did not clearly demonstrate an effect of temperature increase on the elastic properties of the COx claystone.  $\nu_{13}$  is systematically higher than  $\nu_{12}$  and the deformation  $\varepsilon_{33}$  increases systematically much more than  $\varepsilon_{22}$  during the deviatoric loading. Therefore, an anisotropic micro-cracking damage develops during the deviatoric loading and this damage corresponds probably to the opening of microcracks mainly axial (vertical) and oriented in parallel to the bedding plane and to the applied axial stress, with opening direction mainly parallel to the axis 3 and thus perpendicular to the bedding plane (Fig. 1). For the parallel orientation, microcracking damage induces therefore the opening of the bedding planes, which has already been proposed by Grgic et al. (2019) from uniaxial compression tests on another claystone with strains and ultrasonic wave velocities measurements. Under uniaxial conditions ( $P_c = 0$  MPa), the volumetric deformation is contractant at 20 °C and becomes dilatant at higher temperatures (Fig. 4). Volumetric dilatancy is the consequence of the opening of tensile microcracks (parallel to bedding) and also oblique sliding microcracks during the deviatoric loading. In addition, the rapid initial heating induced probably micro-cracking damage because of the transitory pore water overpressure due to thermal expansion, which is therefore more significant at higher temperatures. With a confining pressure of 4 MPa (Fig. 5) or 12 MPa (Fig. 6), the behaviour remains overall contractant whatever the temperature, due to the action of the confining pressure, which reduces the micro-cracking damage (induced during the initial heating and the deviatoric loading) and therefore the dilatancy.

For the perpendicular orientation and all confining pressures (0, 4 and 12 MPa), there is an overall decrease in the axial Young's modulus  $E_{33}$  and an increase in the Poisson's coefficient  $\nu_{31}$  when the deviatoric stress increases (Fig. 13). For the uniaxial conditions, this trend is less obvious for the axial Young's modulus  $E_{33}$  because some data are missing and because the decrease is hidden by the significant axial compaction visible in the deformation curves (Fig. 7). For the perpendicular orientation and uniaxial condition, this significant axial compaction is due to the stiffening of the rock structure corresponding to the closure of phyllosilicate sheets aligned with the bedding planes which are perpendicular to the axial stress direction. There is no noticeable impact of temperature up to 100 °C on these evolutions. Because of these evolutions of the elastic coefficients, an anisotropic damage develops during the deviatoric loading (the material becomes softer in the lateral direction), which is mainly due to the opening of axial (vertical) microcracks perpendicular to the direction of the bedding plane. This interpretation has already been proposed by Grgic et al. (2019) from uniaxial compression tests on another claystone and by Sarout et al. (2006) from triaxial compression tests on the COx claystone, both with strains and ultrasonic wave velocities measurements. Under uniaxial conditions ( $P_c = 0$  MPa), the volumetric deformation is always contractant, whatever the temperature (Fig. 7), and the axial deformation is more significant than for the parallel direction. This significant axial compaction is due to the stiffening of the rock structure, which is responsible for curvature of the axial strain curves at the beginning of the loading. This behaviour (significant axial compaction) coexists with the anisotropic micro-cracking damage. These features correspond to a classical behaviour of clayey rocks and have already been highlighted by Grgic et al. (2019) from uniaxial compression tests on a claystone with strains and ultrasonic wave velocities measurements. Contrary to the parallel case, the behaviour is still contractant at high temperatures because microcracks created during initial heating are closed as soon as the axial stress is increased during the compression tests. With a confining pressure of 4 MPa (Fig. 8) or 12 MPa (Fig. 9), the volumetric deformation is still contractant whatever the temperature. The axial strain curves are not curved at the beginning of the mechanical loading, compared to the uniaxial tests, because of the initial action of the confining pressure that closed the bedding planes and pre-existing microcracks and penny-shaped pores aligned with the bedding plane before the application of the deviatoric stress.

Moreover, whatever the orientation (parallel or perpendicular), deformations are generally larger and larger with the increase in confining pressure. This could easily be explained by the fact that the material becomes more ductile and the peak strength increases with the confining pressure. This is well illustrated in Figure 17, which represents the evolution of the axial strain at peak (measured with the strain gages) as a function of temperature for all samples (except those for which strain gages

didn't work), with polynomial (3rd order) fitting curves. Despite the data scattering due to the material heterogeneity, this trend is globally verified for all temperatures except sometimes for the uniaxial compression tests with perpendicular orientation whose axial strain at peak is overestimated because of the axial compaction due to the closure of the bedding planes (perpendicular to the axial stress direction). In addition, the influence of temperature on the peak deformation is not always obvious and no conclusions can be drawn at this stage.

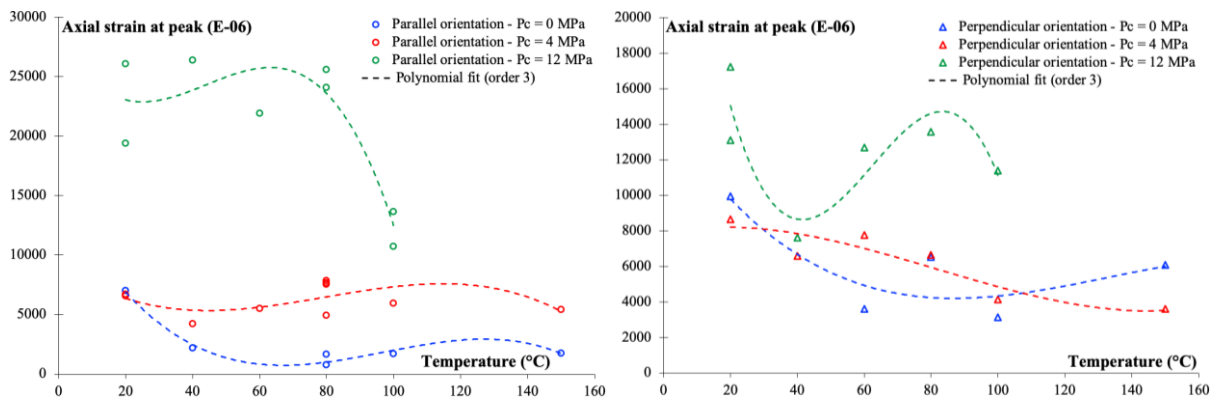


Figure 17 - Evolution of the axial strain at peak (measured with the strain gages) as a function of temperature for parallel and perpendicular orientations and for all confining pressures (0, 4 and 12 MPa), with polynomial (3rd order) fitting curves.

### Peak strength

During the initial rapid heating stage (at a constant heating rate of 50 °C/h), which generated probably pore water overpressure due to thermal expansion and very low permeability of the COx claystone, some microstructural modifications could have occurred in the samples. The thermal expansion of the rock has been analysed in recent studies (Mohajerani 2011; Zhang et al. 2017). The coefficient of thermal expansion of water ( $2.6 \times 10^{-4} \text{ (}^\circ\text{C)}^{-1}$  at 25 °C and  $5.8 \times 10^{-4} \text{ (}^\circ\text{C)}^{-1}$  at 80 °C) is an order of magnitude greater than that of solid grains in the COx claystone ( $2.6 \times 10^{-5} \text{ (}^\circ\text{C)}^{-1}$  at 25 °C and  $11 \times 10^{-5} \text{ (}^\circ\text{C)}^{-1}$  at 80 °C). This differential thermal expansion induced therefore pore water overpressure, which had probably enough time to dissipate during the waiting time of 14 hours that was imposed to each sample before the mechanical loading. However, this transitory overpressure was probably enough to generate microcracks, mainly under uniaxial condition (i.e., without confining pressure). These initial thermo-induced microcracks are probably parallel to the bedding planes which correspond to the weakness planes, as it is the case when the desaturation of a COx sample creates microcracks (hydro-induced microcracks) parallel to the bedding planes. The action of the confining pressure ( $P_c = 4$  or 12 MPa) reduces the creation and opening of these microcracks induced during the initial heating.

This initial thermo-hydro-mechanical damage could probably explain why for the parallel orientation under uniaxial conditions, the peak deviatoric stress decreases very significantly (-62% about from 20 °C to 100 °C) and volumetric dilatancy appears with the temperature increase (Fig. 10); the material was initially damaged by the rapid heating and this damage was more significant the higher the temperature. Under triaxial conditions, the decrease of the peak strength is less significant for  $P_c = 12$  MPa (-27% from 20 °C to 100 °C) and not noticeable for  $P_c = 4$  MPa. Parallel orientation and  $P_c = 4$  MPa is the only case where there is no decrease in the peak strength with increasing temperature. This is difficult to explain but it could be due to the heterogeneity of the mechanical results which could be more reliable if more tests were carried out. It is worth emphasizing that previous studies (Armand et al. 2017b; Zhang et Rothfuchs 2004) have already shown that the COx claystone exhibits an important variability of its peak strength. For the perpendicular orientation, there is also a decrease in the peak strength with temperature (until 100 °C) for both uniaxial and triaxial ( $P_c = 4$  and 12 MPa)

conditions but this decrease is more moderate (from 20 °C to 100 °C: -29% for  $P_c = 0$  MPa, -23% for  $P_c = 4$  MPa, -22% for  $P_c = 12$  MPa). As for the parallel orientation, the transitory overpressure induced by the initial heating was probably enough to create and open microcracks, which are probably parallel to the bedding plane and more significant under uniaxial conditions. However, for cylindrical samples cored perpendicularly to the bedding plane, these microcracks are closed as soon as the axial stress is increased during the compression tests. This could explain why the impact of these microcracks on the peak strength is less important for the perpendicular orientation than for the parallel orientation, especially for uniaxial conditions, and why dilatancy didn't appear. It is worth emphasizing that the peak strength of perpendicular samples is in general significantly lower than for the parallel samples (except for the parallel samples that were initially thermo-damaged), which is not common for transverse isotropic rocks such as claystones, shales... This could be explained by the material heterogeneity and the sampling (conservation and origin of drill cores).

Previous laboratory experimental studies on the impact of temperature on the COx claystone mechanical behaviour can be found in the literature. Zhang (2021) and Liu et al. (2019) performed triaxial tests with lateral decompression (i.e., a more representative loading path of stress evolution around an underground cavity) at temperatures up to 90 °C and showed a degradation of the failure strength with the increase in temperature. This result is therefore in agreement with the main result of our study (overall decrease of the triaxial compression strength of the COx claystone with the increase of temperature up to 80-100 °C). It is worth emphasizing that in these works, as in our work presented here, the samples were not fully saturated (saturation degree was about 90%) when tested mechanically due to water evaporation during sampling, storage and preparation. Furthermore, all these tests were performed under the so-called pseudo-drained condition. With respect to the small size of their samples, 20 mm in diameter and 40 mm in height as in our case, Liu et al. (2019) considered that their axial strain rate ( $2 \cdot 10^{-6}$ /s) during the deviatoric loading, which is not that different from our loading rate ( $5 \cdot 10^{-6}$ /s), is as slow enough to avoid the over-pressurization of pore fluid. Moreover, Menaceur et al. (2015) carried out fully saturated and fully drained triaxial thermal tests on COx specimens by using a hollow cylinder thermal triaxial device with short drainage length specially developed for low permeability geomaterials. Their experimental program was aimed at further investigate the effects of temperature on the shear strength response of the COx claystone by comparing tests carried out at 80 °C with tests run at 25 °C. They observed only a slight reduction in shear strength due to temperature and concluded that this slight difference observed is actually in the range of the dispersion observed when testing COx specimens. They acknowledged that their preliminary observation is to be confirmed by further fully saturated and drained tests (only 2 tests at 80 °C were compared to only one test at 20 °C). However, Zhang et al. (2007) performed triaxial compression tests on classical cylindrical core samples of the Opalinus clay at elevated temperatures between 20 °C and 115 °C and under undrained conditions to investigate the temperature influence on the strength. They found a significant reduction of the strength (and an increase in material ductility) with increasing temperature and proposed that this reduction is probably caused by thermally-induced pore overpressure which reduces the effective mean stress. Therefore, it is difficult to compare these different studies carried out under different experimental conditions. Indeed, thermal impact on the strength of a claystone differs from saturated to unsaturated states and from drained to undrained conditions, as already noticed by Zhang et al. (2017). Our experimental conditions (unsaturated state and pseudo-drained condition) are similar to only those of Liu et al. (2019).

#### 2.3.2.2 Impact of water content decrease at very high temperature (150 °C)

For both orientations (parallel and perpendicular) and all confining pressures (0, 4 and 12 MPa), there is a significant increase in the peak strength for the highest temperature (150 °C), as shown in the Figure 10 and the Table 2. This increase is more significant for the parallel samples (+200% for  $P_c = 0$  MPa, +75% for  $P_c = 4$  MPa, +50% for  $P_c = 12$  MPa, compared to 100 °C) than for the perpendicular samples (+40% for  $P_c = 0$  MPa, +25% for  $P_c = 4$  MPa, +50% for  $P_c = 12$  MPa, compared to 100 °C). In addition, for the parallel samples under uniaxial condition and triaxial condition at  $P_c = 4$  MPa (data

for  $P_c = 12$  MPa are missing), there is also a significant increase of the axial Young's modulus  $E_{11}$  for 150 °C (Fig. 11). But there is no noticeable influence of temperature on the axial Young's modulus  $E_{33}$  for the perpendicular samples. Finally, the influence of temperature is not always obvious but the post-peak behaviour seems to be more brittle at the highest temperature (150 °C) for the parallel orientation (Figs. 4-6). This increase in the material strength, as well as the material stiffening of the elastic and post-peak behaviours, can be explained by analysing the water content of the samples. Indeed, as shown in the Table 1, the initial water content of the samples is homogeneous and varies from 6.3 to 7.2 %. After the tests, the post-mortem water content was measured on some samples (Tab. 2). Samples that were tested at temperatures lower or equal to 100 °C didn't lose much water during the experiment. Generally, the higher the temperature, the lower the water content but it never fell under 6.0%. However, for the samples tested at 150 °C, the water content decreased drastically post-mortem, until 1.2.4% for the more desaturated sample (EST66764-11, perpendicular orientation,  $P_c = 0$  MPa).

Actually, at temperatures higher than 100 °C, water is in a gaseous state (vaporisation) and can escape from the samples. Under uniaxial conditions (i.e., without lateral confining pressure), water can escape through the drainage holes designed in the center of both steel plates at sample ends (at the top and bottom) and also laterally even if samples are sealed in a Viton® jacket. Under triaxial conditions (i.e., with a confining pressure), water can only escape through the drainage holes at both sample ends because the confining pressure prevents the lateral drainage of water. This can explain why for the samples tested at 150 °C, the water content decrease is greater under uniaxial conditions than under triaxial conditions (Tab. 2). Different studies have already shown a sensitivity of claystones to water content with an increase in mechanical strength with desaturation of the material (Chiarelli et al. 2003; Valès et al. 2004; Yang et al. 2013; Zhang et Rothfuchs 2004; Pham et al. 2007). The effect of water content on the compression strength of other rocks types has also been shown in the past, i.e., Grgic et al. (2005) on iron ore rock, Hawkins and McConnell (1992) on sandstone. Grgic et al. (2005) and West (1994) analysed the effect of capillary suction rather than the water content on the compressive strength, especially in the high suction domain (i.e., low water content). In the case of experiments on the COx claystone presented here, samples are strongly desaturated at 150 °C because of the water vaporisation, which induces the development of a very significant capillary suction and then an increase of the effective mean stress. It is usually suggested that at low water contents, suction contributes to rock strength and stiffness in a similar way to its well-known contribution to soil strength. In the case of the COx claystone, the suction phenomenon is probably not the only phenomenon that causes the evolution of the compressive strength. In such clayey rocks, the modification of the mechanical properties of some hydrated minerals (e.g., phyllosilicates) could also be implied.

### 2.3.2.3 Influence of the thermal loading path

To study the impact of thermal loading path (loading rate and waiting time), triaxial compression tests at  $P_c = 4$  MPa with parallel orientation and for a temperature of 80 °C were performed under three different conditions:

- 1- EST66421-6, EST66721-1: thermal loading rate at 50 °C/hour until 80 °C, waiting time of 14 hours.
- 2- EST66721-2: thermal loading rate at 50 °C/hour until 80 °C, waiting time of only 1 hour.
- 3- EST66721-3: thermal loading rate at only 1 °C/hour until 80 °C, waiting time of 1 hour.

The peak strengths are 27.8 MPa, 27.9, 26.5 and 29.1 (Tab. 2), respectively. First, it is worth noting again that the action of the confining pressure probably reduced the microcracking damage during the heating and that the peak strengths of these 4 samples tested at 80 °C are not that lower than the peak strength at 20 °C (Tab. 2, Fig. 10). Second, as said previously, transitory pore water overpressure due to thermal expansion developed probably inside the samples during the initial heating stage, thus inducing micro-cracking damage. It was expected that these overpressure and

damage were greater in the first two cases and that the dissipation of this overpressure before the mechanical test was better in the first and third cases (especially in the third case for which the thermal loading rate was the slowest). Since there is no significant difference in the peak strengths of the four tests, it means that there was no impact of the thermal loading rate and the waiting time; the water overpressure induced the same amount of damage and dissipated equally efficiently (without modifying significantly the effective mean stress) in all cases.

The impact of the thermal loading path before the mechanical test was also studied under uniaxial condition on parallel samples and a temperature of 80 °C:

- 1- EST66421-3: thermal loading rate at 50 °C/hour until 80 °C, waiting time of 14 hours.
- 2- EST66421-2: thermal loading rate at 50 °C/hour until 80 °C, waiting time of only 1 hour.
- 3- EST66421-8: thermal loading rate at only 1 °C/hour until 80 °C, waiting time of 1 hour.

The peak strengths are 6.9 MPa, 10.4 MPa and 8.3 MPa (Tab. 2), respectively. First, these three peak strengths are much lower than for 20 °C (EST66420-3: 19.9 MPa), which means that pore water overpressure induced very significant micro-cracking damage inside the samples in the absence of confining pressure, whatever the thermal loading path. Second, as for the previous analysis with  $P_c = 4$  MPa, there is no sufficiently significant difference in the peak strengths of the three tests to explain this with the differences in the thermal loading paths. This means again that there was no significant impact of the thermal loading rate and the waiting time; the water overpressure induced almost the same amount of damage and dissipated equally efficiently in all cases before the deviatoric loading. These results show that the choice of the thermal loading rate had no influence on the interpretation of experimental results. Obviously, this has to be confirmed with additional tests.

## 2.4 Conclusion

To study the effect of temperature on the mechanical properties of the Callovo-Oxfordian (COx) claystone from Bure (Meuse/Haute-Marne, France), short-term compression tests in a triaxial cell under pseudo-drained condition with axial and lateral strains measurements were performed at different temperatures (20, 40, 60, 80, 100 and 150 °C), for different confining pressures (0, 4 and 12 MPa) and samples orientations (parallel and perpendicular to the bedding plane). In addition, multi-step creep tests in a triaxial cell with axial and lateral strains measurements were carried out at different temperatures (20, 40, 60, and 80 °C), for different confining pressures (2 and 12 MPa) and orientations (loading direction parallel and perpendicular to the bedding plane) to characterize the long-term mechanical behaviour.

From the short-term compression tests, the following conclusions can be made based on the identifiable tendencies despite the scattering of some experimental results due to the material heterogeneity and sampling (conservation of drill cores):

- For both parallel and perpendicular orientations, under both uniaxial and triaxial conditions, when the deviatoric stress increases, there is an overall decrease in the Young's modulus and an increase in the Poisson's coefficients. This anisotropic damage is due to the opening of axial microcracks. Moreover, for both orientations, when the confining pressures increases, the peak deformation and strength increase.
- During the initial heating, transitory pore water overpressure (due to thermal expansion) induces microcracks probably parallel to the bedding planes. This explains why volumetric dilatancy, which is the consequence of the opening of axial microcracks during the deviatoric loading, is only observed for the parallel samples under uniaxial conditions and high temperatures. Indeed, confining pressure reduces these initial thermo-induced microcracks, which are also closed when the axial stress increases during the compression tests when the orientation is perpendicular.

- Despite the data dispersion, temperature has globally a negative impact on the peak strength of the COx claystone until 100 °C due to the initial thermo-hydro-mechanical damage (induced by the initial heating) which is all the greater as the temperature is high. The decrease in the peak strength is the most significant for the parallel samples under uniaxial conditions for which volumetric dilatancy appears with the temperature increase. For all other conditions, the decrease of the peak strength with the temperature increase is more moderate and there is no dilatancy. For parallel orientation and  $P_c = 4$  MPa, no decrease in peak strength with increasing temperature was observed, which could be explained by the material heterogeneity.
- The peak strength of perpendicular samples is in general significantly lower than for the parallel samples (except for the parallel samples that were initially thermo-damaged), which is not common for transverse isotropic clay rocks. This could be explained by the material heterogeneity and the sampling process.
- There is no significant impact of the thermal loading path (loading rate and waiting time before the compression test) on the mechanical results; the water overpressure induced almost the same amount of damage and decreased the peak strength almost identically in the three tested thermal loading paths.
- There is no noticeable impact of temperature up to 100 °C on the evolutions of the elastic coefficients.
- For all orientations and confining pressures, there is a significant increase in the peak strength for the highest temperature (150 °C), which can be explained by the very significant decrease of the water content of the samples. Indeed, at such high temperature, pore water is vaporized and escapes from the sample, which induces the development of a very significant capillary suction. At low water contents, suction contributes to the strength of the COx claystone.

In-situ, there is a competition between the excess pore pressure due to the thermal loading induced by the radioactive waste and the drainage due to pore pressure gradient increase. Considering the periodic distribution of an important number of similar parallel disposal cells and their lengths, the thermally induced overpressure between cells will occur under quasi-undrained conditions (it could not be dissipated in the horizontal direction). Then, the knowledge of the impact of temperature and induced pore water overpressure on the mechanical properties of the COx claystone is of great importance. According to these experimental results obtained in laboratory under specific conditions (unsaturated samples, pseudo-drained condition), temperature has a likely negative impact on the claystone resistance to failure. But if this thermo-hydro-mechanical damage is induced, it would probably be limited to the very near field of the excavation damaged zone, where the confining pressure is the lowest. Moreover, as predicted by Andra (Armand et al. 2017a), before the heating by the radioactive waste, the creep of the clay host rock will put into contact the wall of micro-tunnels with the grout and the steel canisters containing the radioactive waste packages, thus inducing a confining pressure at the wall (a couple of MPa is expected). Thus, even at the very near field (i.e., at the wall of micro-tunnels), the confining pressure will never be equal to zero, which will limit the damage induced by the heating.

This first experimental study gave interesting results but additional similar tests (and also another stress paths such as lateral decompression) would be welcome to reduce data scattering and confirm the trends identified concerning the impacts of temperature on the mechanical behaviour of the COx claystone with different confining pressures and sample orientations. In addition, other experimental conditions, such as fully drained conditions (on resaturated and slightly desaturated samples), should also be considered to get a better estimation of the strength reduction induced by the initial heating since there is no pore pressure increase that modifies the mean effective stress during the mechanical loading under fully drained conditions. Finally, such a study (with a very large amount of thermo-mechanical tests) would require to be performed on the same borehole and the drill cores extracted from this borehole should be kept in T1 type cells which allow a better long-term conservation of the initial mechanical properties (T1 cell allow to confine the drill core of COx claystone under pressure).

Finally, after core drilling in laboratory, all cylindrical should be scanned under X-ray tomography to better select the less initially damaged samples. Following all these recommendations should allow a better reliability and representativity of such laboratory experimental results.

So far, only multi-step creep tests at  $T = 20$  °C and  $P_c = 2$  and 12 MPa, and at  $T = 80$  °C and  $P_c = 12$  MPa, for both parallel and perpendicular samples, were performed on the COx claystone. The remaining multi-step creep tests are in progress. These first results showed that creep deformations are larger at higher temperature (80 °C) and that long-term strength seems to decrease with temperature. This conclusion has obviously to be confirmed when all the creep tests at different temperatures will be finished.



## 3. CEA

### 3.1 Introduction

The main objective of this work is to investigate the time-dependent behaviour of the claystone under moderate temperature level. To do that, several creep tests have been realised. The basic principle of the experiment consists in increasing first the temperature, then applying successive increasing levels of deviatoric stress. Different creep experiments are realised, each test is realised with its particular level of temperature. Note that the temperature is kept constant during all the experiment, so the measured time-dependent strains are only due to mechanical loading. Another important point is the fact that before starting the creep, the sample is saturated with synthetic site water, under confinement, in order to mimic as well as possible the initial conditions observed in-situ.

### 3.2 Material and methods

#### 3.2.1 Material and sampling

The samples are carefully over-cored using special tools, one equipped with cutting teeth for Boom clay (Figure 1), the other equipped with a diamond ring. The coring is made rapidly, without water to avoid any modification of the moisture content. During coring the main part of the core is protected against drying. Then the cored is machined with a lathe to obtain a perfect cylinder with a diameter equal to 30.8 mm and a height comprised between 60 and 65 mm. Moisture content and bulk density are measured. After machining the sample is immediately introduced into the triaxial cell.



Figure 1 - Over-coring of Boom Clay with special coring tool.

#### 3.2.2 Experimental devices and procedures

The main equipment consist in a triaxial HOEK-type cell designed to allow the confinement of the sample with radial stress ( $\sigma_2=\sigma_3$ ) and axial stress ( $\sigma_1$ ) controlled independently (Figure 2). The sample is confined into a neoprene rubber sleeve. The lateral confinement is ensured with hydraulic fluid under pressure. The upper piston and the bottom piston are equipped with a drainage circuitry with small stainless steel pipes connected with the injection pump situated near the oven. So the cell makes possible the re-saturation of the sample and the control of the pressure of the pore solution. The cell is equipped with two LVDT sensors that measure the length variation of the sample during the test, allowing the survey of the axial strain. The advantages of that cell are the following: the cost is moderate, the device is simple and reliable. The main drawback is the impossibility to measure the lateral strain of the sample.

The cell is placed inside a special loadframe equipped with a hydraulic jack that controls the vertical load leading to the axial stress. The frame and the cell are placed into an oven that allows a good control of the temperature along the test (Figure 3). Specific devices are used to control three parameters: the confining pressure, the axial load, and the pore pressure. In the oven, two frames are operated at the same time, and consequently at the same temperature. Two similar tests are made at the same time in order to get two results, with similar conditions. During the experiments the following parameters have been measured and recorded: the temperature, the confining pressure, the axial load (leading to the axial stress), the pore pressure, and the axial strain. Note that a careful calibration of the LVDT sensors was made at the different temperature levels planned for the tests. The pressure sensors placed out of the oven run at room temperature and do not need specific calibration.

Two experimental benches (each with two cells into an oven) are implemented. So four samples can be tested at the same time.



*Figure 2 - HOEK-type triaxial cell used for the creep experiments.*



*Figure 3 - Testing bench with two HOEK-type triaxial cells and loadframe inside the oven.*

The synthetic site water is specific for each claystone. For Boom Clay (Table T1) the composition is adapted from Cui et al., *Géotechnique* (2009). For Opalinus Clay (Table T2) the chemical composition comes from Delage and Belmokhtar, *Acta Geotechnica* (2022). The pore water is prepared from de-ionised water and pure chemicals components from Sigma-Aldrich©.

Table 1 - Chemical composition of the pore water used for Boom Clay.

Salt	CaCO <sub>3</sub>	NaHCO <sub>3</sub>	KCl	MgCl <sub>2</sub> 6H <sub>2</sub> O	NaF	NaCl	Na <sub>2</sub> SO <sub>4</sub>
Concentration (mg/L)	5000.0	1170.0	25.0	22.0	11.0	10.0	0.30

Table 2 - Chemical composition of the pore water used for Opalinus Clay.

Salt	NaCl	NaHCO <sub>3</sub>	CaCl <sub>2</sub> 2H <sub>2</sub> O	KCl	MgCl <sub>2</sub> 6H <sub>2</sub> O	Na <sub>2</sub> SO <sub>4</sub>
Concentration (mg/L)	2.25	0.01	0.58	0.06	0.62	1.14

The procedure designed to implement the solicitations during the creep test is explained hereafter. The different phases are the following:

- Phase 1: Confinement under isotropic stress state.
- Phase 2: Re-saturation (under isotropic confinement) with synthetic site water. The water is injected into the samples under constant pressure.
- Phase 3: Heating up to the chosen temperature level. During the heating phase the pore pressure is kept constant and the confining pressure is maintained. During heating the drainage is allowed.
- Phase 4: Multi-steps creep experiment. The axial stress is increased in order to generate a deviatoric stress while the other conditions do not vary. The deviator is constant during the creep step. The step ends when we decide to move to another level of deviator. During all the creep phases the drainage is allowed, the pore pressure is constant.

A multi-steps creep experiment, realised under constant temperature, provides interesting results with only one sample. It adds value to both the preparation process and to the long re-saturation phase. Because the temperature is constant along the whole test, the effects of the increasing deviator steps (only) are investigated.

### 3.2.3 Research plan

For each of the two claystones different temperatures need an investigation. The research plan is given in Table 3. After a discussion with the partners, we decided that the maximal temperature for Boom clay would be equal to 80°C. As mentioned previously, two samples are tested at the same time (with the same deviator, the same confining pressure, the same pore pressure and the same temperature). The heating rate is 0.5°C per minute for all the tests.

Table 3 - Research plan for the multi-steps creep experiments.

Claystone	Temperature for creep test (°C)	Orientation of the sample	Number of samples	Number of deviatoric steps (planned)
Boom Clay	40	Perpendicular to bedding	2	4
Boom Clay	60	Perpendicular to bedding	2	4
Boom Clay	80	Perpendicular to bedding	2	4
Opalinus Clay	40	Perpendicular to bedding	2	4
Opalinus Clay	60	Perpendicular to bedding	2	4
Opalinus Clay	80	Perpendicular to bedding	2	4
Opalinus Clay	100	Perpendicular to bedding	2	4

### 3.3 Results and discussion

#### 3.3.1 Creep tests realised with Boom Clay

##### 3.3.1.1 Creep test at 40°C

Two samples have been prepared and machined. Table 4 gives the main features. The re-saturation under isotropic stress state ( $p = 4.7$  MPa) gives a swelling of the samples. The heating phase (from 25°C to 40°C) give an axial dilation strain equal to  $-4715 \mu\text{m/m}$  (Figure 4).

Then the different creep steps are realised. Figure 5 and Figure 6 show the time-dependent behaviours of two similar samples, tested at 40°C. The succession of the creep steps is plotted on the Figure 7 and the Figure 8. Note that the confining pressure and the axial stress are the same for the two samples. These two parameters are controlled at the same time.

The two samples show similar time-dependent behaviours as shown by the figure 9. The variation between the strains can be explained by the variability between the two samples.

Table 4 - Features of the two Boom Clay samples tested at 40°C.

Name	Diameter (mm)	Height (mm)	Mass (g)	Moisture content (%)	Bulk density
Boom-40C-01 (3707c)	31.00	63.26	96.816	22.01	2,028
Boom-40C-02 (3708c)	31.00	69.29	108.258	22.01	2,070

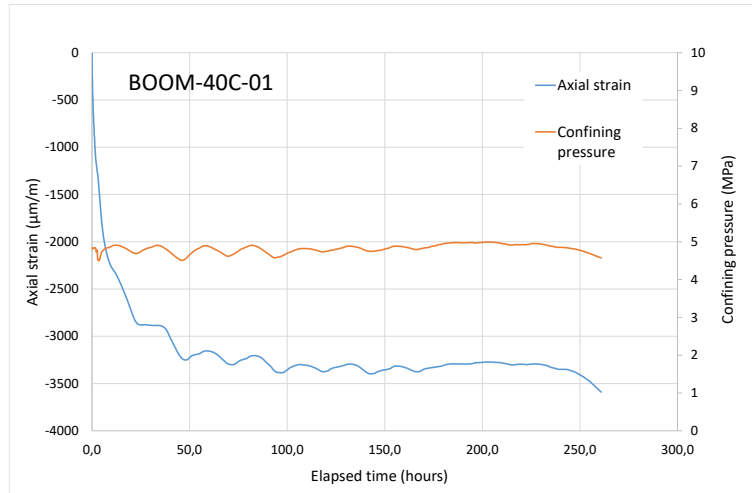


Figure 4 - Swelling of the sample during hydration under isotropic confinement.

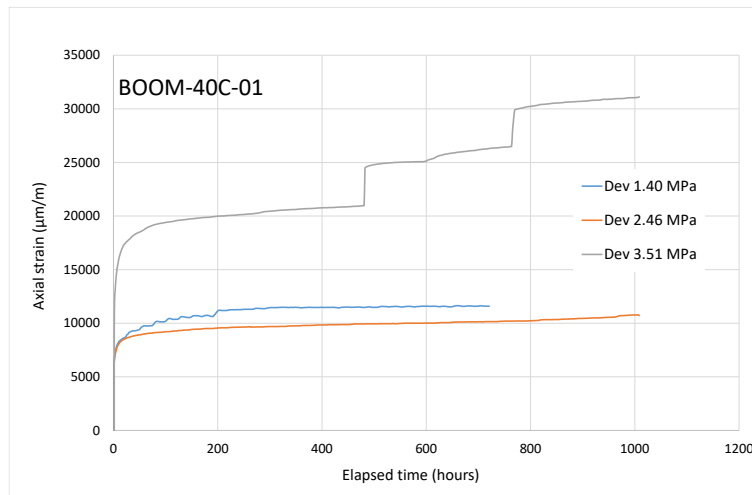


Figure 5 - Different creep steps for sample BOOM-40C-01.

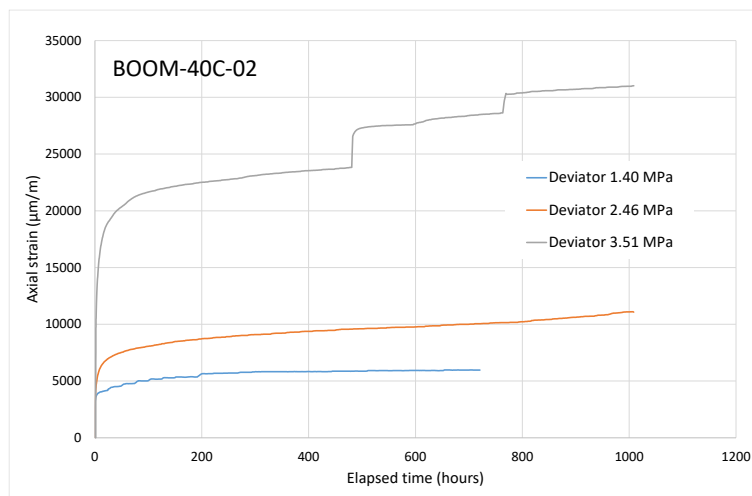


Figure 6 - Different creep steps for companion sample BOOM-40C-02.

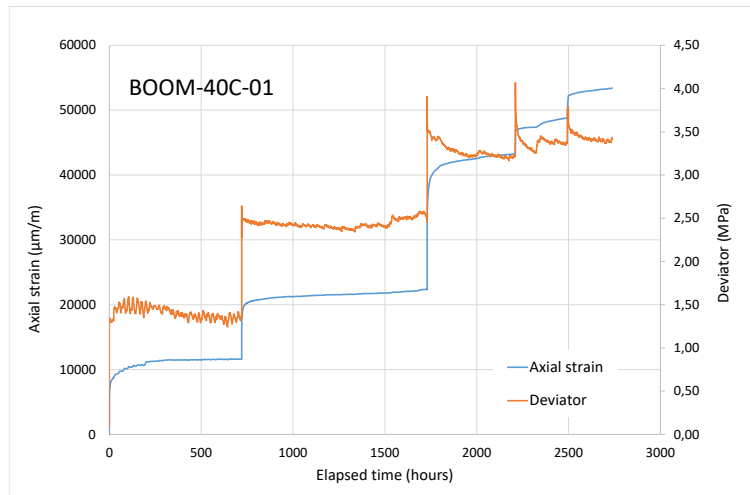


Figure 7 - Successive creep steps realised on sample BOOM-40C-01.

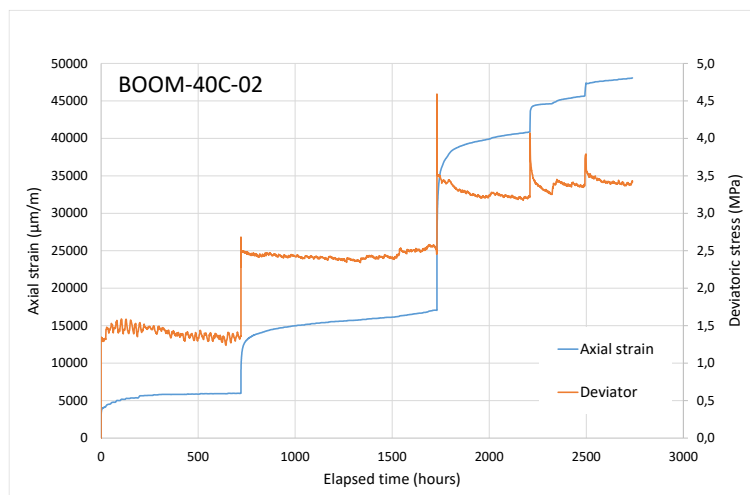


Figure 8 - Successive creep steps realised on companion sample BOOM-40C-02.

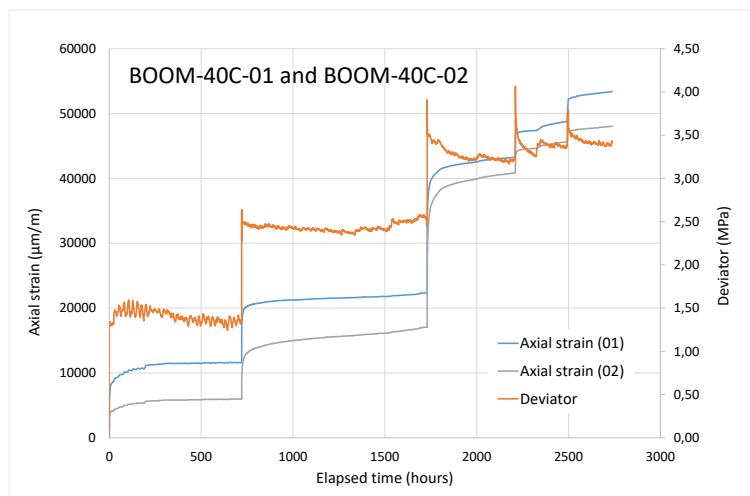


Figure 9 - Successive creep steps realised on samples BOOM-40C-01 and BOOM-40C-02.

3.3.1.1 Creep test at 60°C

Two samples have been prepared and machined. Table 5 gives the main features. The hydration under isotropic confinement ( $p = 4.5 \text{ MPa}$ ) shows an important swelling of the sample (Figure 10). The same behaviour is observed for the two samples.

Table 5 - Features of the Boom Clay samples tested at 60°C.

Name	Diameter (mm)	Height (mm)	Mass (g)	Moisture content (%)	Bulk density
Boom-60C-03 (3711c)	30.98	60.78	93.750	21.38	2.046
Boom-60C-04 (3712c)	31.00	60.72	94.520	21.44	2.062

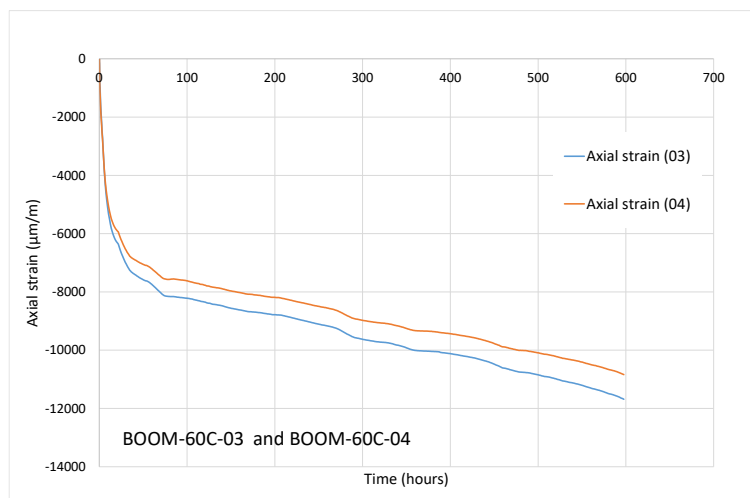


Figure 10 - Swelling of the two samples during hydration under isotropic confinement.

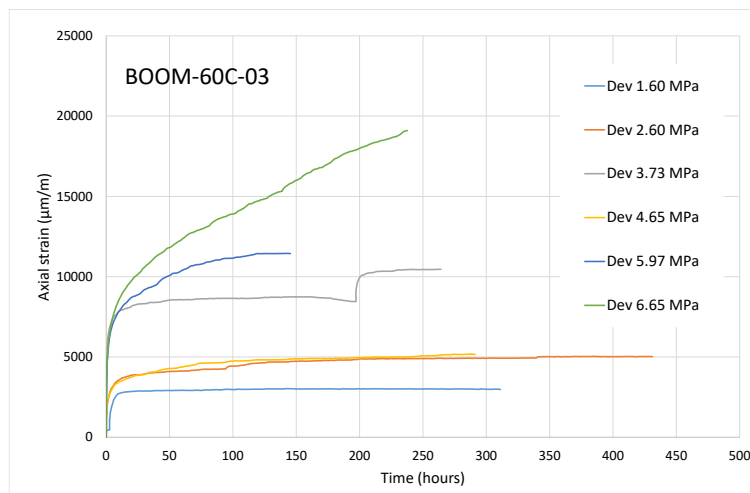


Figure 11 - Comparison of the successive creep steps with sample BOOM-60C-03.

The successive creep steps are shown by Figure 11 to Figure 15. For sample n°03 it was possible to make six creep steps. Under the maximal deviator (6.65 MPa) the strain does not stabilize and the

failure is obtained after 240 hours. For sample n°04 only four creep tests have been realised (maximum deviatoric creep being equal to 4.65 MPa). The next steps have immediately led to the failure of the sample. Nevertheless, the two samples exhibit very similar time-dependent behaviour during the main part of the test (Figure 15).

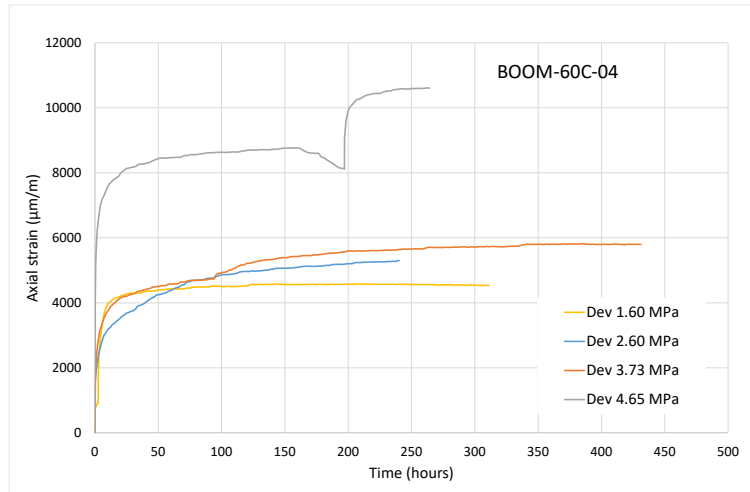


Figure 12 - Comparison of the successive creep steps with sample BOOM-60C-04.

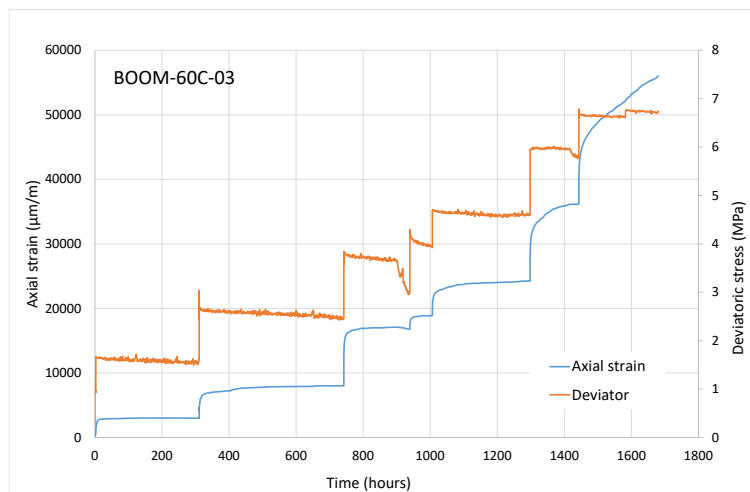


Figure 13 - Successive creep steps with sample BOOM-60C-03.

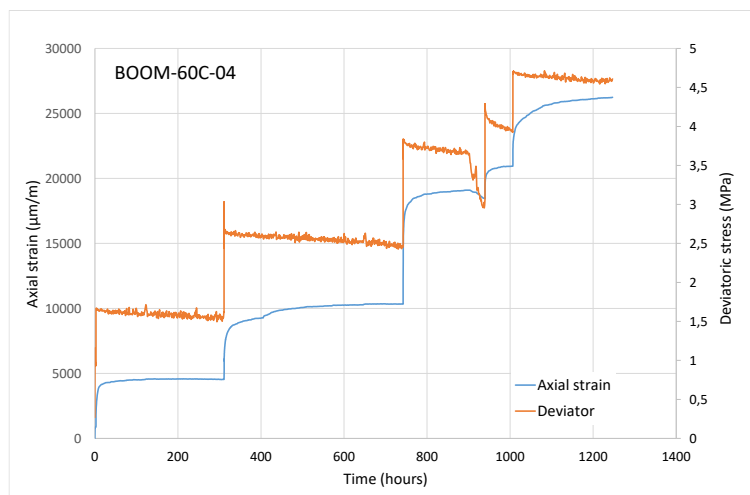


Figure 14 - Successive creep steps with sample BOOM-60C-04.

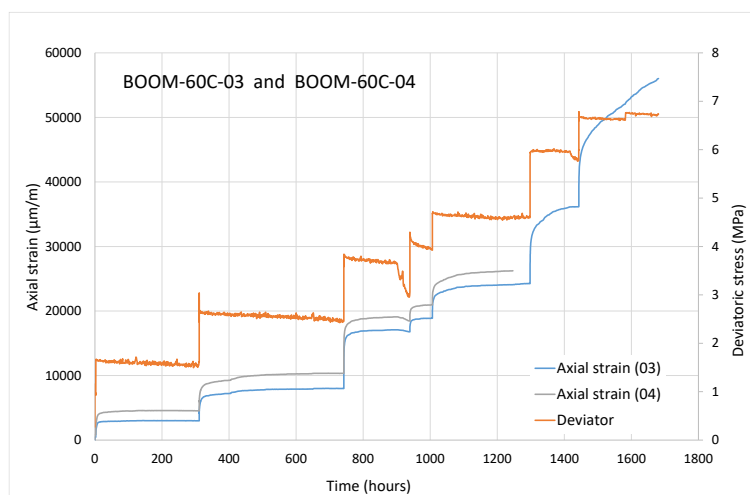


Figure 15 - Comparison of the successive creep steps for the two samples BOOM-60C-03 and BOOM-60C-04.

### 3.3.1.1 Creep test at 80°C

The samples tested under 80°C were submitted to only two creep steps (Figure 16 to Figure 20). Table 5 gives the main features. The two samples exhibit the same time-dependent behaviours from a qualitative point of view, with the same kind of evolution and the same kinetics. But the magnitudes of the axial strains are quite different (Figure 20).

Table 6 - Features of the Boom Clay samples tested at 80°C.

Name	Diameter (mm)	Height (mm)	Mass (g)	Moisture content (%)	Bulk density
Boom-80C-05 (3719c)	31.07	59.70	93.151	21.34	2.058
Boom-80C-06 (3720c)	31.07	58.69	90.030	21.58	2.023

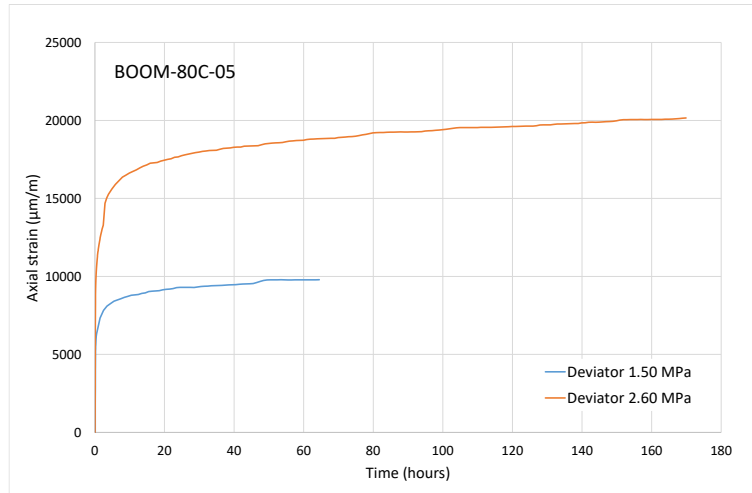


Figure 16 - Successive creep steps for sample BOOM-80C-05.

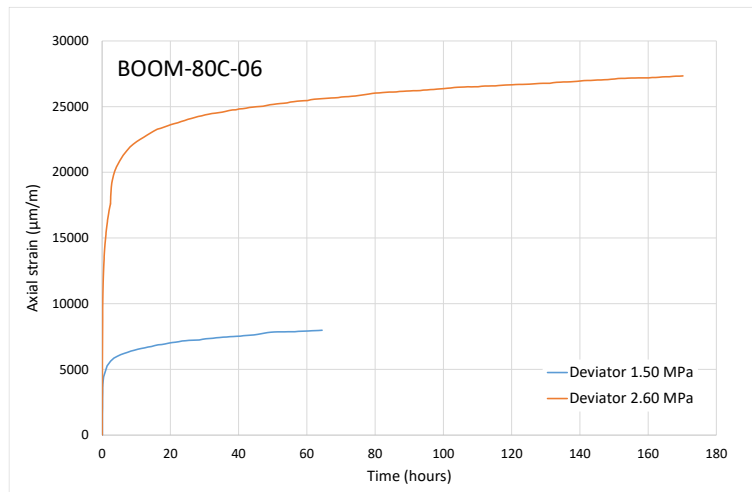


Figure 17 - Successive creep steps for companion sample BOOM-80C-06.

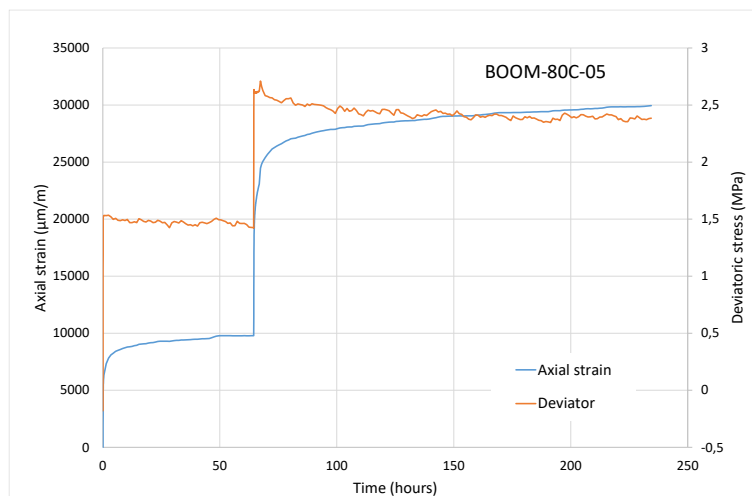


Figure 18 - Successive creep steps for sample BOOM-80C-05.

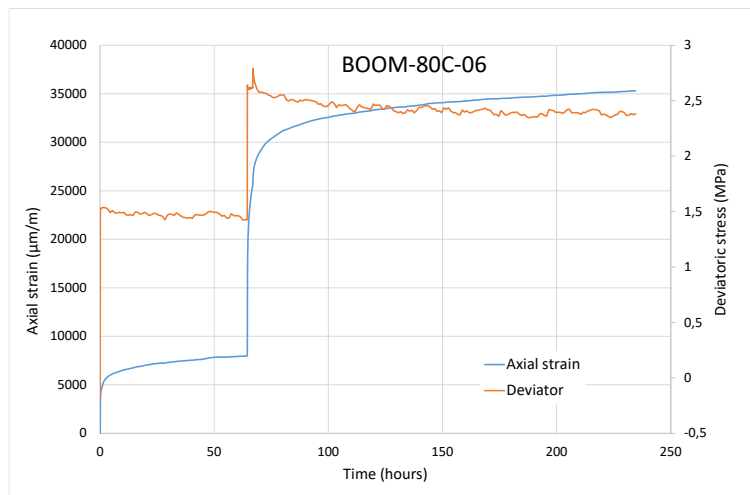


Figure 19 - Successive creep steps for companion sample BOOM-80C-06.

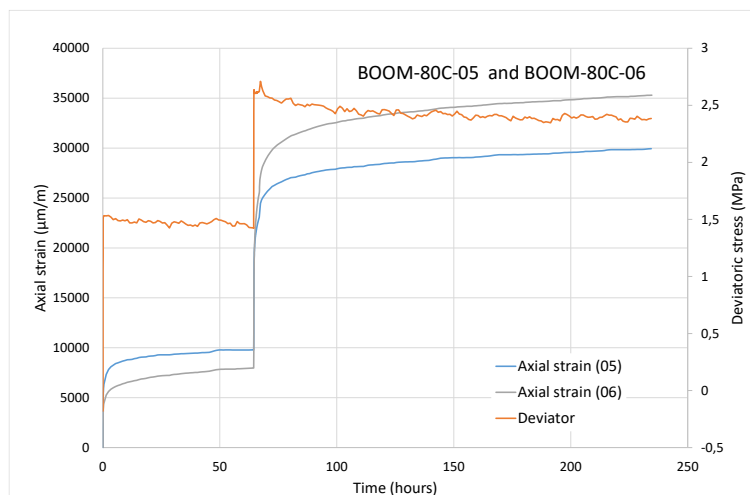


Figure 20 - Successive creep steps for the two samples BOOM-80C-05 and BOOM-80C-06.

### 3.3.2 Creep tests realised with Opalinus Clay

#### 3.3.2.1 Creep test at 40°C

Table 7 - Features of the Opalinus Clay samples tested at 40°C.

Name	Diameter (mm)	Height (mm)	Mass (g)	Moisture content (%)	Bulk density
OPA-40C-01 (3724c)	30.68	65.57	118.432	6.37	2.443
OPA-40C-02 (3725c)	30.72	64.26	116.116	6.37	2,438

Table 7 recalls the main initial features of the samples. The saturation under isotropic confinement ( $\sigma_1 = \sigma_2 = \sigma_3 = p = 6.0$  MPa) has for result an axial swelling of the sample (Figure 21). During this phase, the synthetic water is injected at the bottom face and at the top face of the sample, with an injection

pressure maintained constant ( $P_{inj} = 2.0$  MPa). In accordance with the standard presentation often found in the literature, the swelling is plotted negatively, and the height shortening (for instance due to creep) is plotted positively. After 527 hours the evolution of the axial strain slows down. Due to the confining conditions, the swelling could be considered as isotropic. The maximal swelling strain, due to re-saturation under confinement, is equal to  $8.83 \cdot 10^{-3}$  (OPA-40C-01) or  $7.20 \cdot 10^{-3}$  (OPA-40C-02).

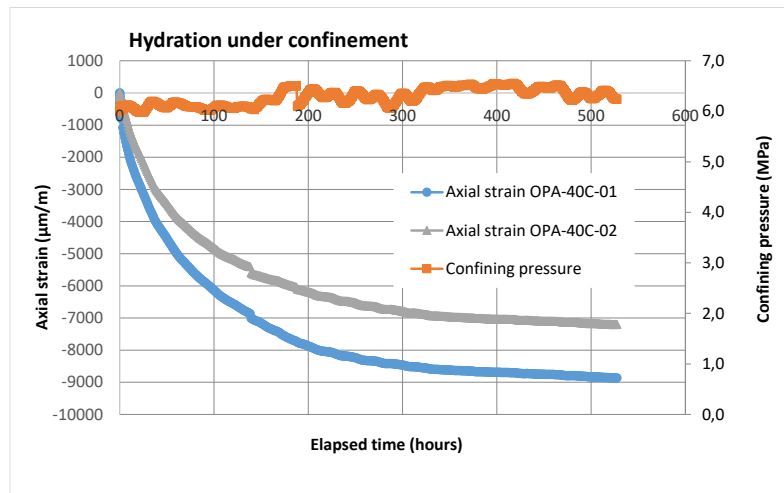


Figure 21 - Strain evolution during the re-saturation phase for the two samples OPA-40C-01 and OPA-40C-02.

The heating phase of the sample is then realised. The resulting axial dilation is equal to  $-1299 \mu\text{m/m}$ . After stabilisation of the sample under constant temperature, during 100 hours, the first step of creep is realised. The successive steps (duration and evolution of the axial strain) are presented on the Figure 22 and the Figure 23. Considering the three first steps, we observe that the magnitude of the strain is increasing when the deviator is higher. For the two other creep steps (7.60 and 10.0 MPa), at the contrary, the magnitude of the creep is slightly decreasing. Figures 24 and Figure 25 give the evolution of the axial strain along the whole series of creep steps, with cumulative axial strain. The time-dependent behaviours of the two samples are very similar regarding the kinetics and the shape of the curve (Figure 26). But the measured strains are different.

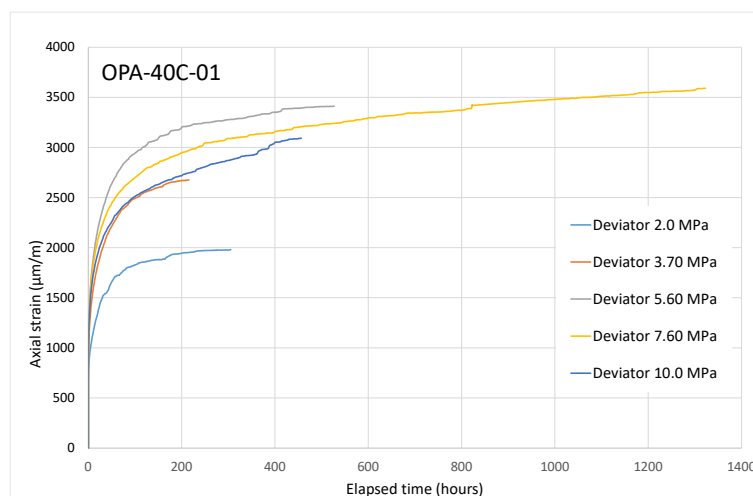


Figure 22 - Comparison of the different creep steps for sample OPA-40C-01.

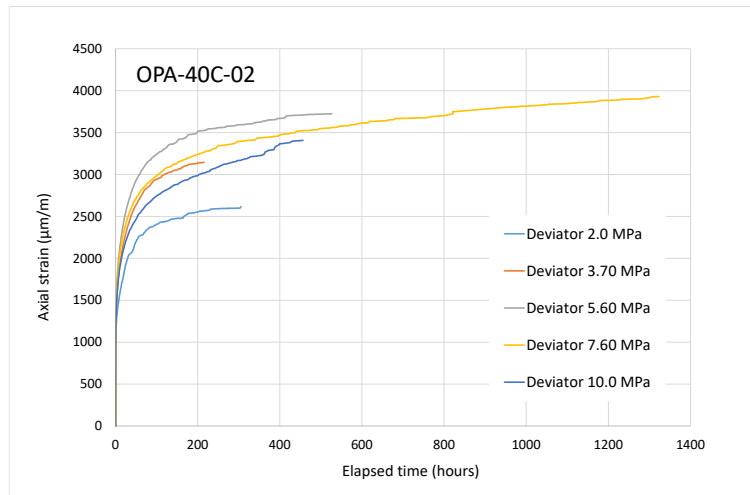


Figure 23 - Comparison of the different creep steps for companion sample OPA-40C-02.

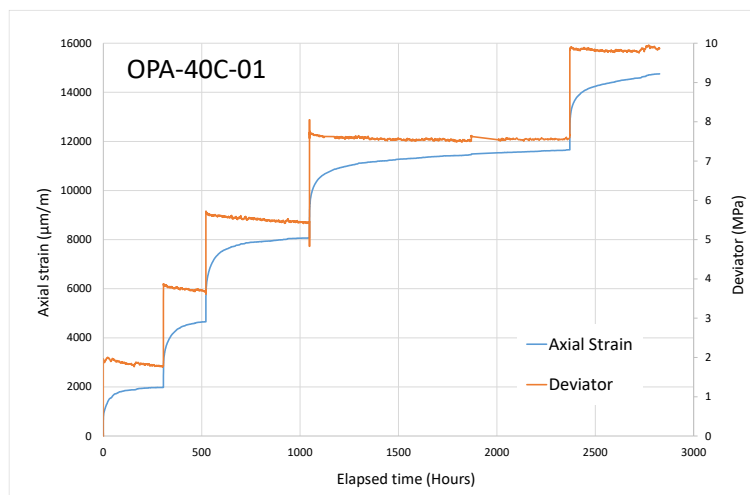


Figure 24 - Comparison of the different creep steps for companion sample OPA-40C-02.

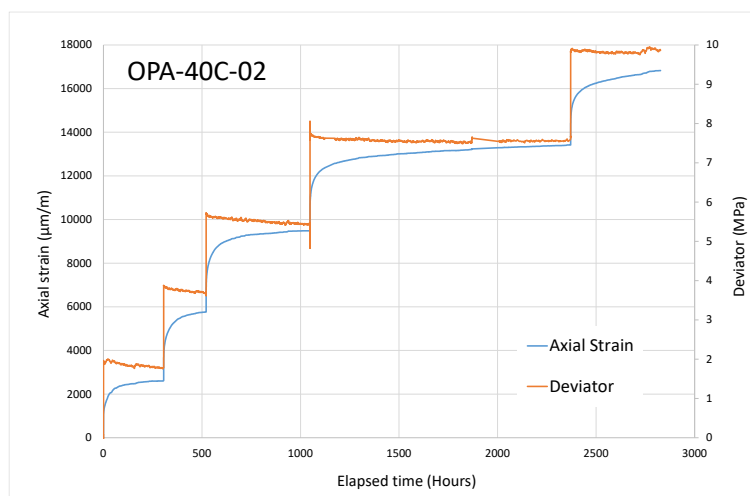


Figure 25 - Comparison of the different creep steps for companion sample OPA-40C-02.

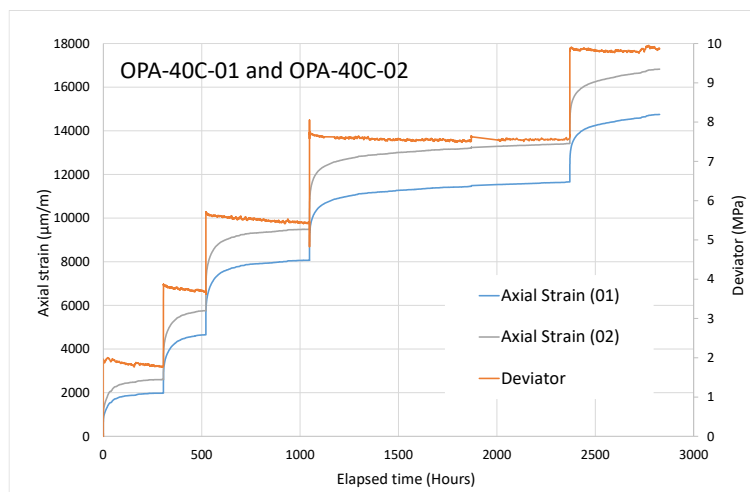


Figure 26 - Successive creep steps for the two samples OPA-40C-01 and OPA-40C-02.

### 3.3.2.1 Creep test at 80°C

Table 8 recalls the main initial features of the samples tested under 80°C. The saturation under isotropic confinement (isostatic pressure =  $p = 6.0$  MPa) has for result an axial swelling of the sample (Figure 27). During this phase, the synthetic water is injected at the bottom face and at the top face of the sample, with an injection pressure maintained constant ( $P_{inj} = 2.0$  MPa). In accordance with the standard presentation often found in the literature, the swelling is plotted negatively, and the height shortening (for instance due to creep) is plotted positively. After 595 hours the evolution of the axial strain slows down. The axial swelling strain due to the hydration is different for the two samples and respectively equal to  $9,146 \cdot 10^{-3}$  (OPA-80C-03) and equal to  $1,115 \cdot 10^{-2}$  (OPA-80C-04).

The heating phase from 25°C to 80°C is then realised. The resulting axial dilation strain is equal to  $-3249 \mu\text{m/m}$  (OPA-80C-03) and equal to  $-3465 \mu\text{m/m}$  (OPA-80C-04). After stabilisation of the sample under constant temperature, during 50 hours, the first step of creep is realised. The successive steps (duration and evolution of the axial strain) are presented on the Figure 28 and the Figure 29.

Having a look at the three first deviatoric steps, we observe that the magnitude of the strain is increasing when the deviator is higher. For the two other creep steps (7.81 MPa and 9.17 MPa), at the contrary, the magnitude of the creep, for the same duration, is decreasing. Note that an unwished drop in the deviatoric stress during the fourth step (deviator 7.81 MPa) has for consequence a drop in the creep strain. Figures 30 and Figure 31 give the evolution of the axial strain along the whole series of creep steps. Figure 32 presents the comparison between the two time-dependent behaviours. The final axial strain is 34% greater for sample OPA-80C-04 compared to that of sample OPA-80C-03.

Table 8 - Features of the Opalinus Clay samples tested at 80°C.

Name	Diameter (mm)	Height (mm)	Mass (g)	Moisture content (%)	Bulk density
OPA-80C-03 (3727c)	30.68	59.60	108847	6.37	2.470
OPA-80C-04 (3728c)	30.56	62.08	113.289	6.37	2.488

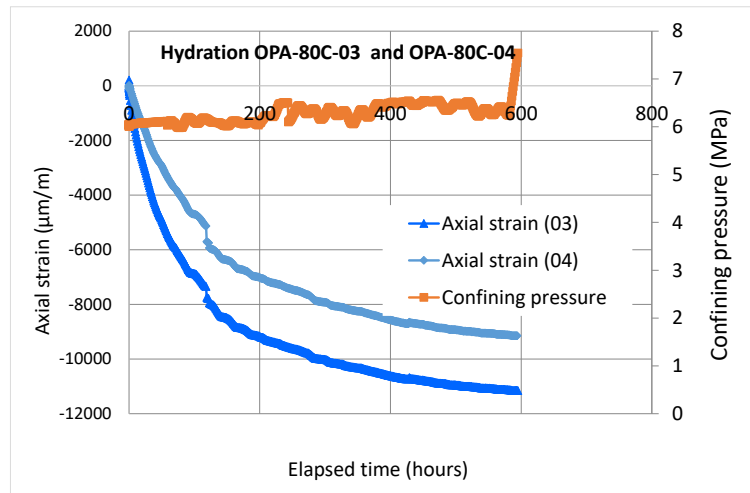


Figure 27 - Strain evolution during the re-saturation phase for the two samples OPA-80C-03 and OPA-80C-04.

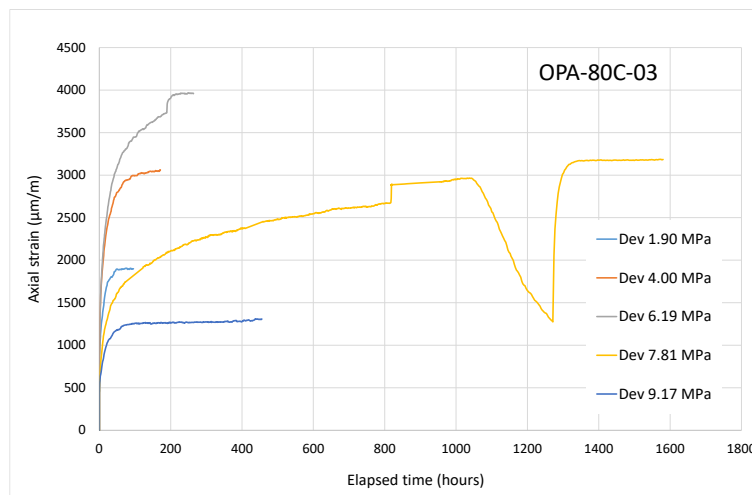


Figure 28 - Comparison of the different creep steps for sample OPA-80C-03.

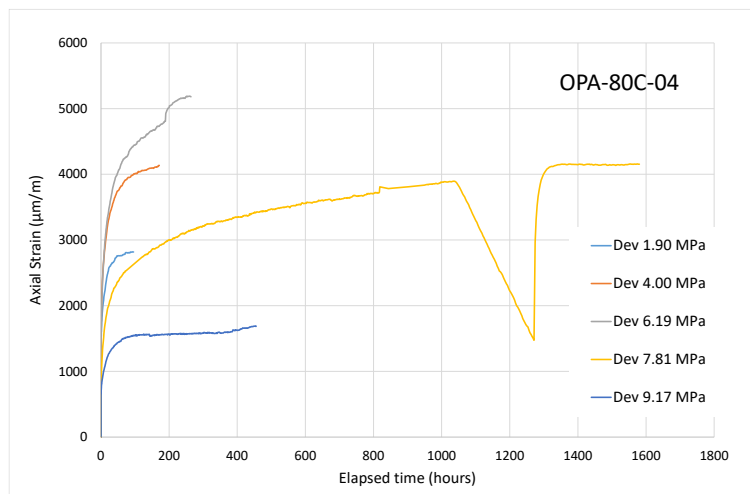


Figure 29 - Comparison of the different creep steps for companion sample OPA-80C-04.

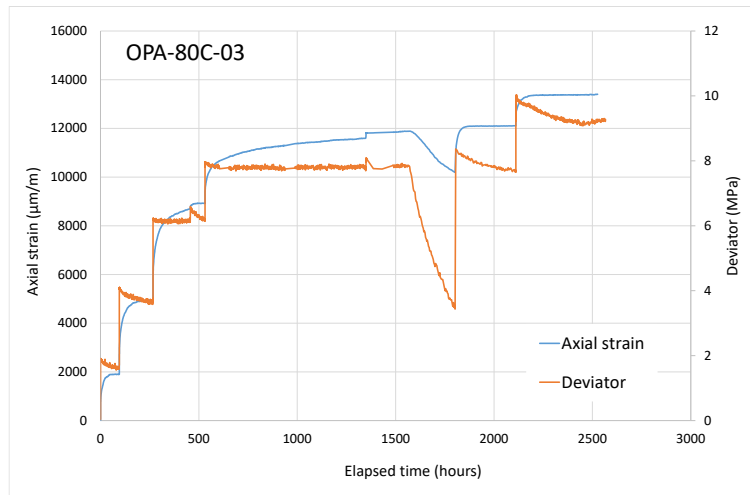


Figure 30 - Successive creep steps for sample OPA-80C-03.

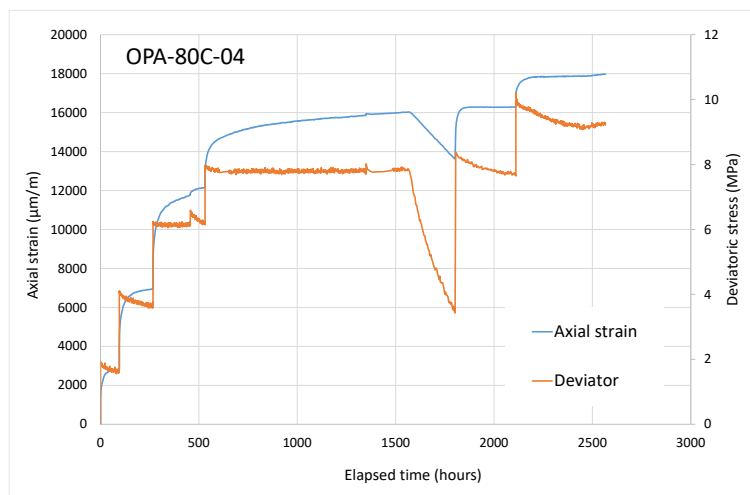


Figure 31 - Successive creep steps for companion sample OPA-80C-04.

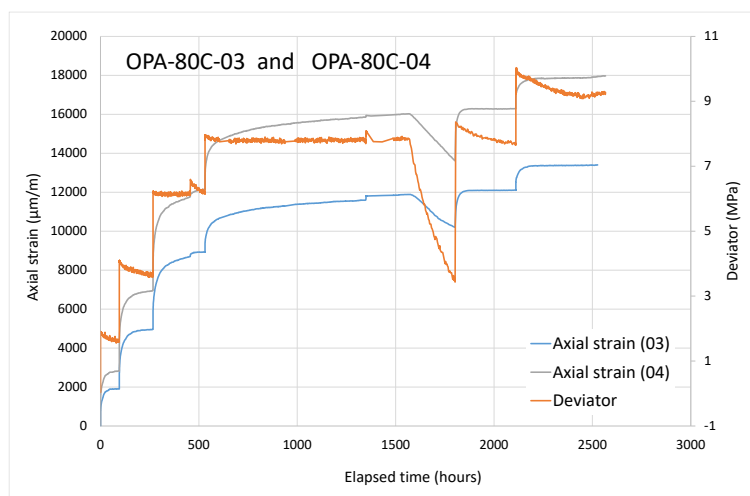


Figure 32 - Successive creep steps for the two samples OPA-80C-03 and OPA-80C-04.

### 3.3.2.1 Comparison

A comparison has been made between one test realised at 40°C and another made at 80°C (Figure 33). For the same level of deviatoric stress, the magnitude of the axial strain is greater at 80°C than at 40°C. Moreover, the strain evolves more rapidly when the temperature is greater.

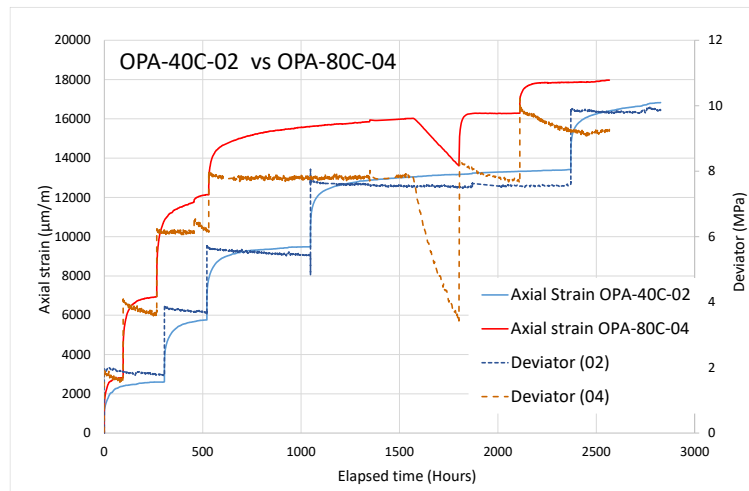


Figure 33 - Comparison between two samples of Opalinus Clay, one tested at 40°C, another tested at 80°C.

## 3.4 Conclusion

Multi-steps creep experiments have been realised, testing two different claystones, namely Boom clay and Opalinus clay. The stress state and the pore pressure conditions applied during the test aim at reproducing, as well as possible, the conditions observed in the geologic site. To do that, a preliminary phase allows to re-saturate the sample under isotropic stress state. During these tests, the temperature is maintained and the deviator is increased thanks to successive steps. The test ends when the sample fails, or when the future developments of the tests are considered as not relevant.

Considering Boom Clay, three to five successive deviatoric steps have been realised. Some samples fail too early, preventing the test on the companion sample to be continued. Probably the natural variability even for two samples over-cored in two very close places in the initial core may explain the difference in the mechanical behaviour. The sample tested at 60°C give a good amount of data, with an extended deviatoric stress range.

Considering Opalinus Clay, five successive creep steps have been realised for two temperature levels. The comparison between the two temperature levels (40°C and 80°C) is enlightening because similar steps have been realised and because the samples did not fail too early. The results show clearly that the magnitude of the strain is greater when the temperature level is higher. Moreover, the kinetics of the strain development is increased when the temperature is higher. The comparison between the behaviours at 40°C and 80°C shows clearly that the strain stabilises easily at 40°C, but evolves a lot at 80°C. But the experimental campaign show that it is very useful to make many experiments in order to:

- better understand the time-dependent behaviour of each claystone, and therefore chose the right values of successive deviatoric stresses to apply during future tests;
- evaluate the effects of the material variability on the time-dependent behaviours; the magnitude of the strain seems to be influenced by the variability, while the kinetics is often the same for two similar samples.

The new knowledge acquired is related to the effect of the temperature level on both the kinetics and the magnitude of the strain.

Remaining knowledge gaps. At this point of the study, it is not possible to establish a link between the temperature level and the deviator that causes the failure of the sample. A better investigation of the effects of the temperature on the magnitude and on the evolution of the strain would need longer creep steps. The time-dependent behaviour under room temperature that was not investigated in the study would be very useful to enlarge the knowledge.

## 4. UKRI- BGS

### 4.1 Introduction

To understand the effects of the heat produced by radioactive waste on the properties of clay-rich materials and the consequences, if any, on their long-term performance, the British Geological Survey (BGS) has performed a series of laboratory-scale tests on samples of candidate repository rocks, which have been subjected to a rapid heating (similar to that following emplacement of a HHGW). In particular, the aim of this study was to examine the influence of heating on (i) the sample's hydraulic conductivity and (ii) the development of internal porewater pressure. Experiments have been undertaken to measure and quantify thermally induced porewater pressures and assess their impact on the thermo-hydro-mechanical (THM) behaviour and their permeability. Samples of clay/mudrock have been tested from ambient (approx. 25°C) to 90°C for orientations both parallel and perpendicular to bedding. Permeability was measured before, during and after thermal loading to quantify any changes in value.

### 4.2 Material and methods

#### 4.2.1 Experimental devices and procedures

A bespoke apparatus was specifically designed and built at the BGS to examine the magnitude of potential over-pressures created by the thermal loading of a mudrock. These parameters are also sensitive to the time-dependent drainage of the sample, and this has also been taken into account in the design of this rig. Samples have been subjected to a K0 stress boundary condition and have been radially constrained but can swell in the axial direction. The BGS custom-designed apparatus has seven components, as shown in Figure 1 and Figure 2: (1) a thick-walled pressure vessel, platens and load frame; (2) an injection pressure system; (3) a backpressure system; (4) six XPC10 zero-volume temperature compensated pressure transducers (accurate to +/-0.25% full scale with a thermal stability of +/-1% of reading/50°C) measuring porewater pressure at different points along the axis of the core; (5) a thermally compensated 75 kN load cell monitoring axial stress; (6) an oven in which the pressure vessel and load frame sit; and (7) a microcomputer-based high-speed data acquisition system. In addition to this instrumentation, thermocouples have been placed inside the oven to record the development of temperature. From test FPR-21-027 onwards, the number of thermocouples was increased from two to five to give additional data. However, as test FPR-20-013 clearly demonstrated, the response of the system does not track a thermocouple and hence, from test FPR-21-027, all recorded temperatures and temperature values presented in the plots and tables are an average of the thermocouple values.

The vessel, platens and LVDT mounts and rods were all manufactured from Alloy 36 (a steel with a low thermal expansion coefficient), pressure-rated to a working pressure of 70 MPa, with the internal surface of the vessel wall hard-chromed to prevent damage.

The configuration of the pressure vessel, sensors and load frame is shown in Figure 1 and a general schematic of the key control/monitoring systems are shown in Figure 2. Table 1 shows the relative positions of the radial filters and the height of each filter referenced to the injection filter. In order to measure changes in porewater pressure, it is necessary for the measurement system (i.e., the radial filters and the void behind them and the pressure sensor) to be water saturated. Although the voidage volume (i.e., the fraction of the total volume not occupied by solids, in this case it represents the volume of the pore space in the filters and measurement system used to measure changes in porewater pressure) was kept to a minimum, this probably has some impact on the measured porewater pressure. This effect has been analysed by using data from the first test (FPR-20-013), see Appendix A. This demonstrated that the thermal compliance from the measurement system and its contribution to the maximum pore pressure value was minor in each sensor. During testing, axial

stress was provided by a hydraulic ram which was connected to an ISCO syringe pump. The axial stress was continuously monitored to maintain a constant boundary stress. Expansion or contraction of the clay during heating/cooling, and while hydraulic testing, was measured by an LVDT on the rear of the vessel (but not visible in Figure 1), providing real-time data on the hydro-mechanical response of the clay. Axial expansion of the pressure vessel has also been measured to correct for apparatus compliance through a second LVDT shown in Figure 1. Unfortunately, this information was not available at the time of writing and will be included in future publications. Pressure and flow rate of test fluids have been controlled using two ISCO, syringe pumps (Figure 2), operated by a central control unit. Movement of each pump piston was controlled by a micro-processor which was continuously monitored and adjusted the rate of rotation of the encoded disc using a DC-motor connected to the piston assembly via a geared worm drive. This has allowed each pump to operate in either constant pressure or constant flow modes. A programme written in LabView™ elicited data from the pump at pre-set time intervals, which has varied depending on the stage of testing. The oven and control pumps have all been located within an air-conditioned laboratory which was maintained at a nominal temperature of around  $20 \pm 1$  °C.

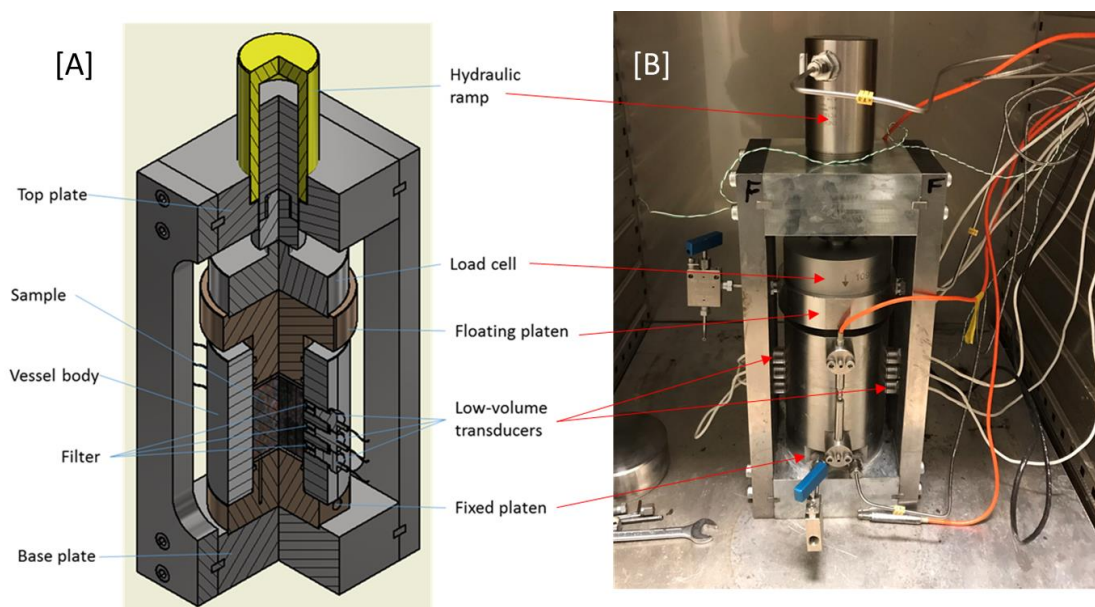


Figure 1 - [A] shows a cut away of the pressure vessel, end-closures, load cells and filters. [B] shows a photograph of the apparatus, assembled and in the oven ready for testing. The radial filters are located at 12.5, 30 and 47.5 mm along the axis of the sample measured from the injection filter. Samples are subject to a  $K_0$  stress boundary condition so are radially constrained but can swell in the axial direction.

All pressure/load sensors and thermocouples were calibrated against laboratory standards by applying incremental steps in pressure/force/temperature from atmospheric to a pre-determined maximum value. This has then been followed by a descending history of pressure steps to quantify hysteresis. The whole process was repeated multiple times before a least-squares fit to the entire data was applied, from which regression parameters were applied to the raw values. Although radial sensors were temperature compensated, minor variations in sensor response due to thermal loading (the largest of which was less than 250 kPa) were observed during calibration. As such, in tests FPR-21-017, FPR-21-027, FPR-21-051, FPR-21-052 and FPR-22-098 additional offsets were applied to ensure sensor and pump pressures matched either at the beginning of the test, or during the first hydration/equilibrium stage. Future examination of the calibration data will be undertaken to develop a more sophisticated approach to allow for variations in sensor response due to temperature. However,

these changes will be relatively minor and will not impact any of the conclusions from this study. For calibration of the thermocouples, the wires have been submerged in fluids contained within the calibrator and subjected to increasing and decreasing steps in temperature, up to a value of 100°C.

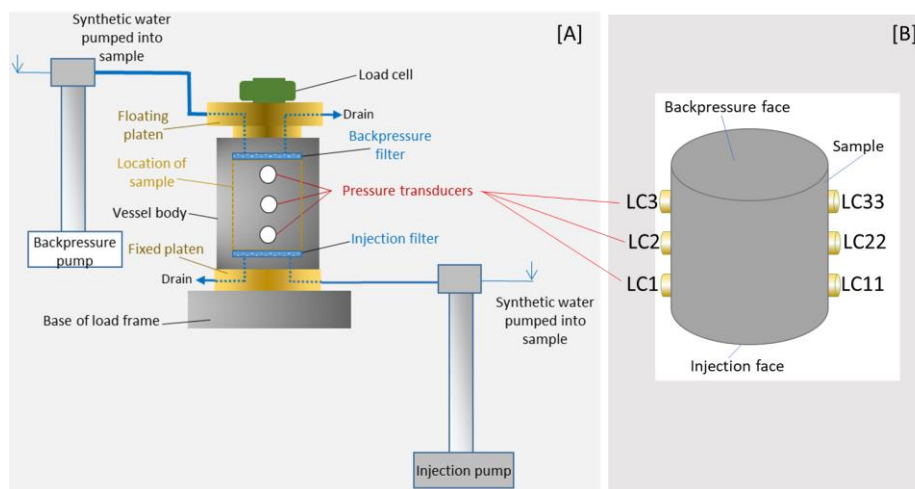


Figure 2 - [A] Schematic showing the layout of the key apparatus components. [B] schematic showing the position of the pore pressure sensors around the periphery of the sample. The movement of fluids into and out of the sample is controlled through high-precision syringe pumps. Samples are radially constrained but free to axially swell.

Table 1 - Location of radial porewater pressure filters which were 8 mm in diameter.

	LC1	LC11	LC2	LC22	LC3	LC33
Height from injection filter to centre of radial filter (mm)	12.5	12.5	30	30	47.5	47.5
Rotation (degrees)	0	180	0	180	0	180

Prior to the sample preparation procedure all samples were kept in vacuum sealed bags and stored in a refrigerator to minimise the potential for moisture loss and microbial growth. Samples were manufactured through a combination of diamond sawing and machine lathing. An X-ray Computed Tomography (CT) image was taken before testing to visualise any potential structures within the sample which may have an impact on the hydro-mechanical results. Once installed, axial load was applied to the sample in one or more ramps simulating the vertical in situ stress. Then, samples have been hydrated, whilst the porewater pressure were continuously monitored. Once hydrated, the intrinsic permeability of the sample was measured by applying an appropriate differential pressure across the core. Axial expansion of the sample was monitored as has the development of porewater pressure along the axial of the core (unfortunately this data requires additional processing which will be done before the end of the project). Following hydraulic testing, the differential porewater pressure was removed and set back to a constant (equal) pressure across the sample. Porewater pressures have then been allowed to equilibrate to the reference pressure.

The temperature designated for a particular test has then been applied to the sample in a single step, simulating the installation of a heat-emitting canister. During this stage, the development of overpressure was monitored along with the thermal expansion of the sample. In this way, sample expansion and over-pressure have been observed in a single test, though the latter was not available for this report. Once hydration was complete, the permeability of the sample was remeasured at the elevated temperature, using the same constant head technique mentioned above. Thereafter, the thermal load on the sample was removed, temperatures were allowed to decay to the ambient value and permeability was then re-measured to determine if thermal loading had a deleterious impact on the hydraulic properties of the clay. Once testing was completed, the sample was removed and, where possible, was reimaged with the CT scanner and sub-divided for post-mortem characterisation.

#### 4.2.2 Permeants

Rehydration of the Callovo-Oxfordian claystone (COx), Boom Clay (BC) and Opalinus Clay (OPA) samples and subsequent permeability measurements, were undertaken using matched ground water samples from the respective formations. The different compositions are presented in Table 2 through Table 4.

The density and viscosity values presented in Table 5 have been applied to the test data to correct for the effects of temperature in the calculation of permeability. These values have been applied as specified in the table and have not been adapted when the temperature of the oven deviated slightly from the tabulated values.

Table 2 - Chemical composition of the synthetic COx solution used to test FPR-20-013.

	NaCl	NaHCO <sub>3</sub>	KCl	CaSO <sub>4</sub> , 2H <sub>2</sub> O	MgSO <sub>4</sub> , 7H <sub>2</sub> O	CaCl <sub>2</sub> , 2H <sub>2</sub> O	Na <sub>2</sub> SO <sub>4</sub>
g/L	1.950	0.130	0.03	0.630	1.020	0.080	0.700

Table 3 - Chemical composition and properties of the synthetic Boom Clay solution used for the natural samples in this study.

	mg/l	mmol/l		mg/l	mmol/l	Property	Unit	Value
Ca	2	0.05	Total	0.77	0.02	pH		8.5
Fe	0.2	0.003	Cl <sup>-</sup>	26	0.7	pCO <sub>2</sub>	Atm	10 <sup>-2.62</sup>
Mg	1.6	0.06	SO <sub>4</sub> <sup>2-</sup>	2.2	0.02	Eh	mV	-274
K	7.2	0.2	HCO <sub>3</sub> <sup>-</sup>	878.9	14.4	Ionic		0.016
Si	3.4	0.1						
Na	359	15.6						
Al	6x10 <sup>-4</sup>	2.4x10 <sup>-5</sup>						

Table 4 - Chemical composition of the synthetic OPA solution (often referred to as Pearson porewater) used for the test of all Opalinus Clay samples.

	Mass in 1 Litre (g)
NaCl	7.598
KCl	0.231
MgCl <sub>2</sub>	0.496
CaCl <sub>2</sub>	0.803
Na <sub>2</sub> SO <sub>4</sub>	1.42
Na <sub>2</sub> CO <sub>3</sub>	0.033

Table 5 - Density and viscosity values used to correct permeability values during heating tests.

Temperature (°C)	Density (kg/m <sup>3</sup> )	Viscosity (Pa.s)
Ambient (20-26)	998.97	0.00100192
50	988.79	0.00054740
70	978.47	0.00040500
90	965.96	0.00031548

#### 4.2.3 Material and sampling

Pre- and post-test sample dimensions are presented in Table 6 along with the standard deviation associated with each measurement. Geotechnical properties are not available as some of the samples have been sectioned for detailed post-mortem analyses including X-ray diffraction and physisorption measurements. This data will be collated and presented in a future publication.

Table 6 - Pre- and post-test sample dimensions. All samples slightly increase in volume, indicating swelling has taken place – a necessity for K0 testing.

Test number	Material	Pre-test dimensions		Post-test dimensions	
		Average diameter (mm)	Average length (mm)	Average diameter (mm)	Average length (mm)
FPR-20-013	COx para	49.90±0.06	59.93±0.05	50.01±0.03	59.99±0.07
FPR-21-017	BC perp	49.90±0.06	59.93±0.05	-	-
FPR-21-024	OPA perp	49.89±0.01	59.90±0.08	50.07±0.03	60.15±0.03
FPR-21-026	OPA para	49.77±0.04	59.92±0.01	50.11±0.06	60.09±0.08
FPR-21-027	OPA para	49.94±0.06	59.98±0.01	50.08±0.05	60.12±0.02
FPR-21-051	OPA para	49.98±0.02	60.08±0.02	50.03±0.02	60.09±0.04
FPR-21-052	OPA para	49.95±0.02	59.98±0.01	50.00±0.02	59.91±0.01
FPR-22-025	OPA perp	49.89±0.02	54.71±0.03	50.04±0.03	54.44±0.05
FPR-22-067	OPA perp	49.90±0.05	60.01±0.02	49.99±0.01	60.34±0.01
FPR-22-098	OPA perp	49.93±0.01	54.80±0.04	-	-

### 4.3 Results and discussion

To date ten tests have been undertaken as outlined in Table 6 and Table 7. Of those tests, six have been successful and yielded data on intrinsic permeability and the development of pore pressure during heating. The other four tests failed for a variety of reasons, as shown in Table 7. The loading path and test stages varied depending on which material was tested. Detailed information describing each test history is presented in Tables 8, 10 through 13, 15 and 16. In all tests, axial stress was gradually applied at a constant rate to each sample, until a value equivalent to the in situ effective stress was reached. Following a short period of equilibration, axial stress and porewater pressure then simultaneously increased at a constant rate, until equivalent in situ conditions were applied to the sample. Thereafter, during each test, intrinsic permeability was measured before and after applying the thermal load to the sample and then re-measured once the temperature had been returned to ambient conditions. Test FPR-21-027 was the exception to this protocol, as the final permeability measurement has not been obtained due to the premature completion of testing caused by an incorrect pump setting.

Test samples have been selected following initial X-ray CT examination of the core material. High quality samples have been machined to exact diameter by lathing excess material from the sides and face of the sample. Following the failure of sample FPR-21-026, additional emphasis was placed on the machining of samples to obtain a close match between sample diameter and the bore of the test vessel. However, this has not always been successful and even very small differences in diameter between the sample and vessel bore, see Section 4.3.4, have resulted in a failed test. Prior to the onset of testing, each sample was photographed and when possible, X-ray CT images obtained to ensure sample quality and identify potential features which may impact testing, Figure 3.

Table 7 - BGS test matrix. Tests FPR-21-017, -024, -026 and 22-067 failed for various reasons listed in the table. Test FPR-21-052 included measurement of pore pressure development and permeability values at multiple temperatures and two stress states. COx = Callovo-Oxfordian Claystone, OPA = Opalinus Clay, BC = Boom Clay. Para = parallel to bedding, perp = perpendicular to bedding.

Test number	Material	Permeability (ambient)	Pore-water pulse	Permeability (temperature)	Permeability (ambient)	Comment
FPR-20-013	COx para	✓	✓	✓ (89°C)	✓	Successful test
FPR-21-017	BC perp	✓	✓	X (~200 °C)	x	Test overheated
FPR-21-024	OPA perp	x	x	x	x	Axial ram failed
FPR-21-026	OPA para	✓	x	x	x	Bypass flow
FPR-21-027	OPA para	✓	✓	✓ (83°C)	x	Partially successful
FPR-21-051	OPA para	✓	✓	✓ (90°C)	✓	Successful test
FPR-21-052	OPA para	✓	✓	✓ (multiple temps)	✓	Successful test
FPR-22-025	OPA perp	✓	✓	✓ (multiple temps)	✓	Successful test
FPR-22-067	OPA perp	x	x	x	x	Bypass flow
FPR-22-098	OPA perp	✓	✓	✓ (multiple temps)	✓	Successful test

#### 4.3.1 Test FPR-20-013 (COx taken from core barrel EST 60812, parallel to bedding)

Figure 3 shows sample FPR-20-013 following manufacture, X-ray CT imaging and during installation into the apparatus. During manufacture small fragments of claystone broke away from the backpressure end of the sample (visible in Figure 3 [F] through[H]). These were placed at the downstream end of the core so as not to impair the measurement of porewater pressure. This test comprises 8 experimental stages, as listed in Table 8. The evolution of water pressure during hydration and reloading, along with the induced changes in porewater pressure within the sample, are shown in Figure 4[A]. All pressure traces exhibit multiple changes in slope, indicating complex resaturation behaviour. Sensors LC11, LC2 and LC33 exhibit abrupt changes in slope at around days 4.7, 4.9 and 5.9 days respectively, indicative of a slow-down in the rate of hydration (and pressure) increase within the sample. At around day 5.4, filters LC1, LC22 and LC3 converge and thereafter approach the reference external water pressure of 4.5 MPa at around day 5.8. These are joined on day 6 by filter LC22 and by LC3 and LC2 on days 7.6 and 8 respectively. Figure 4[B] shows the development of porewater pressure averaged on each plane of measurement along the axis of the core. While some of the localised detail in the development of pressure is lost, the data shows a progressive wetting front moving along the axis of the core. A complex coupling between the rates of hydration at the various planes within the sample also emerges, evidenced, for example, around day 6, when the pressure across plane 3 begins to increase as the rate of pressure change across plane 2

decreases. This is again, suggestive of localised changes in permeability, probably linked to swelling, resulting in increased/decreased changes in the rate of pressure development.

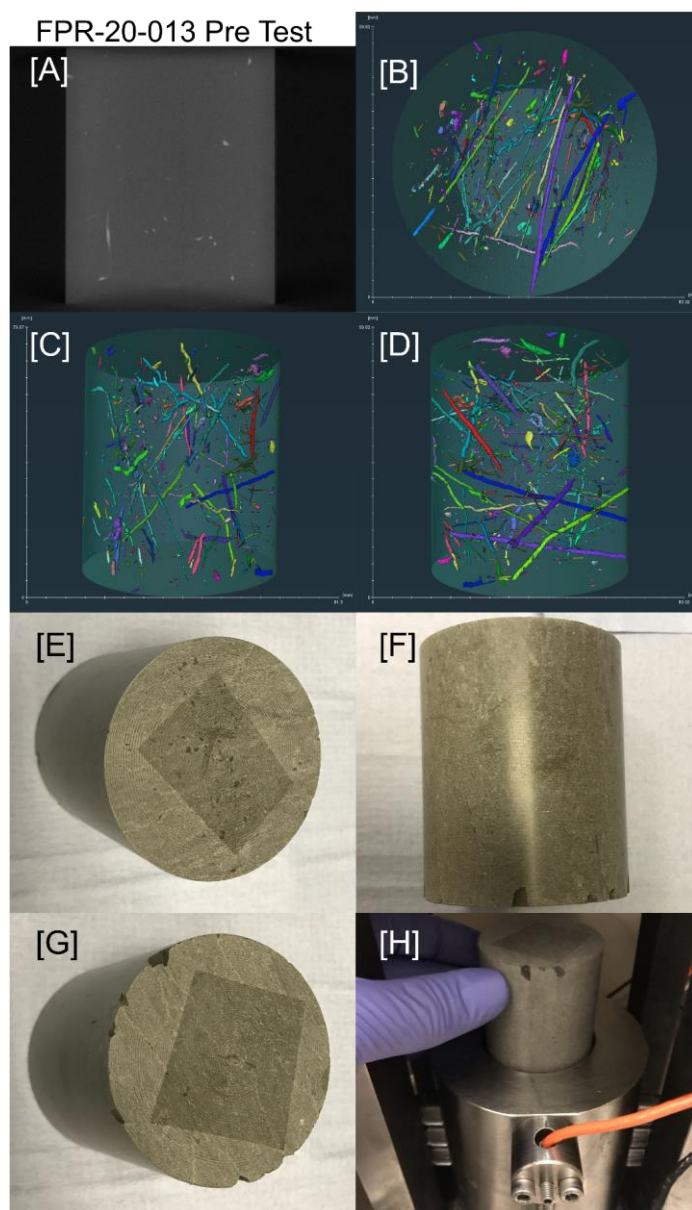


Figure 3 - Pre-test imaging of sample FPR-20-013. [A] Orthogonal CT; [B] CT image of features XY orientation; [C] CT image of features XZ orientation; [D] CT image of features YZ orientation; [E] injection face of sample [F] side view of sample; [G] backpressure face of sample.; [H] sample emplaced in the rig.

In test stage [4] a constant head test was performed to measure the hydraulic permeability (Table 8), yielding a value of  $7.5 \times 10^{-21} \text{ m}^2$ . This value is relatively low for CO<sub>x</sub> orientated parallel to bedding, but is in line with values reported by Harrington et al. (2017). Data in Figure 5 shows a broadly linear distribution in pressure along the sample.

Sensors in plane 1 (LC1 and LC11) exhibit a slight difference in pressure, possibly linked to the higher porewater pressures at this location of the core (nearest its injection end). The distribution of pressure along the subsequent planes (2 and 3) remains equal with no significance differences in value noted.

In test stage [5] porewater pressure was allowed to decay before the temperature was increased to around 88 °C in stage [6]. This resulted in a rapid increase in porewater pressures, Figure 6, which peaked in the mid-plane at a pressure of 20.5 MPa. The development of porewater pressures appear to initially track oven air temperature but this relationship quickly breaks down as pressures continue to increase while the rate of temperature change rapidly slows. Pressure recorded in sensor LC1 is the exception, as it decreases prior to day 19.2. However, it quickly increases again, even when oven air temperature does not change. The true value of temperature driving pore pressure expansion lies somewhere between the air and vessel measured responses, Figure 6. In future studies the inclusion of thermocouples inside the vessel would be advantageous. As temperature increased, porewater pressure initially rose in a uniform manner, suggesting the sample was fully saturated and that the system was probably measuring the response of the clay to heating (see Appendix A). As the porewater pressure around sensor LC1 approached that of the axial stress, it spontaneously began to decrease, suggestive of internal fracturing within the clay. Thereafter pressure around the sensor increased for a second time, but on this occasion peaked at a lower value, showing a more rounded peak than previously observed. This behaviour provides additional confirmation that the transducers are measuring a true material response i.e., if expansion of fluid in the measurement filter drove the increase in pressure, it would not be able to increase once the pressure had been released. The remaining sensors continued to increase, peaking in pressures ranging from 17.1 to 20.5 MPa. Most sensors exhibited some degree of complexity in the shape of each pressure transient, but all began to rapidly decay following peak pressure, such that by day 20 the pressure pulse had fully drained back to the external water pressure of 4.5 MPa.

Accounting for changes in water viscosity and density, the permeability of the core decreases slightly on heating, stage [7], yielding a value of  $4.8 \times 10^{-21} \text{ m}^2$ , Table 9. However, when temperature returns to ambient conditions, stage [8], the permeability of the core remains only depressed slightly at  $6.5 \times 10^{-21} \text{ m}^2$ , suggesting (a) little if any significant change occurs to the hydraulic properties from rapid heating of the core and (b) residual impact on the porosity of the clay from heating exists.

Table 8 - Experimental stages for test FPR-20-013. Stages denoted by EQ = equilibration, CHT = constant head test; TI = temperature increase and TD = temperature decrease.

Stage number	Type	Day	Injection pressure (MPa)	Backpressure (MPa)	Axial stress (MPa)	Oven temperature (°C)
1	EQ	0	0	0	7-9.5	20
2	Ramp	2.0	0-4.5	0-4.5	9.5-14.0	20
3	EQ	2.3	4.5	4.5	14.0	20
4	CHT	11.9	6.0	4.5	14.0	20
5	EQ	15.2	4.5	4.5	14.0	20
6	TI	19.2	4.5	4.5	14.0	88
7	CHT	24.3	6.0	4.5	14.0	90
8	TD, CHT	36.1	6.0	4.5	14.0	20

Table 9 - FPR-20-013. Intrinsic permeability ( $k$ ) data from ambient and elevated temperature testing where  $k_{in}$  = permeability based on inflow,  $k_{out}$  = permeability based on outflow and  $k_{ave}$  = the average permeability based on inflow and outflow values. Inflow data from the around 88 °C was not available due to leakage from the pipework during that phase of testing.

Stage number	Temperature	Intrinsic permeability, $k$ , ( $m^2$ )		
		$k_{in}$ ( $m^2$ )	$k_{out}$ ( $m^2$ )	$k_{ave}$ ( $m^2$ )
4	20 °C	$6.6 \times 10^{-21}$	$8.3 \times 10^{-21}$	$7.5 \times 10^{-21}$
7	88 °C	–	$4.8 \times 10^{-21}$	$4.8 \times 10^{-21}$
8	20 °C	$7.4 \times 10^{-21}$	$5.7 \times 10^{-21}$	$6.5 \times 10^{-21}$

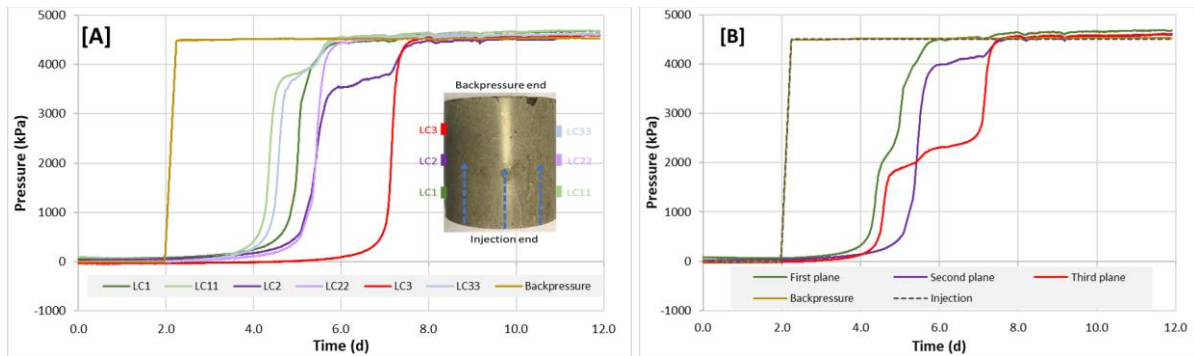


Figure 4 - [A] Time evolution of water pressure during hydration phase in test FPR-20-013. Inset is a schematic image of sample FPR-20-013 showing the direction of flow and relative positions of the radial filters. [B] Time evolution of water pressure during hydration phase (averaging sensors). First plane =  $(LC1 + LC11)/2$ ; second plane =  $(LC2 + LC22)/2$ ; third plane =  $(LC3 + LC33)/2$ .

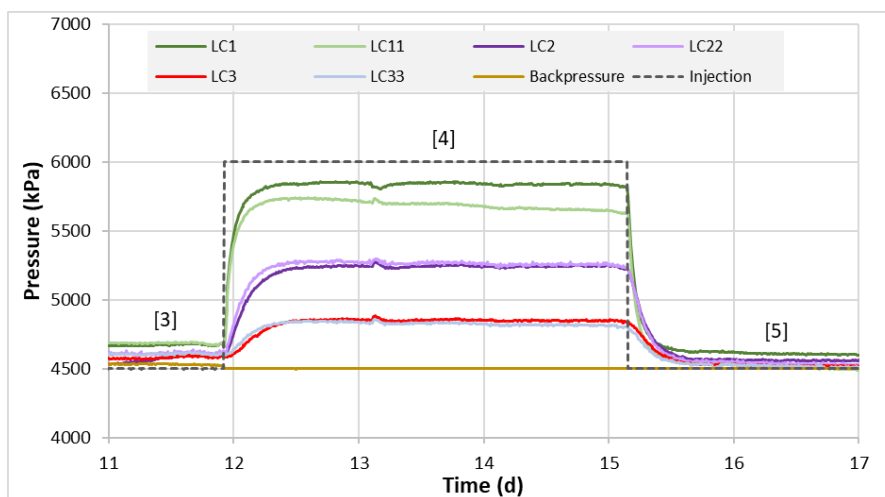


Figure 5 - FPR-20-013. The development of porewater pressure during constant head test, stage [4].

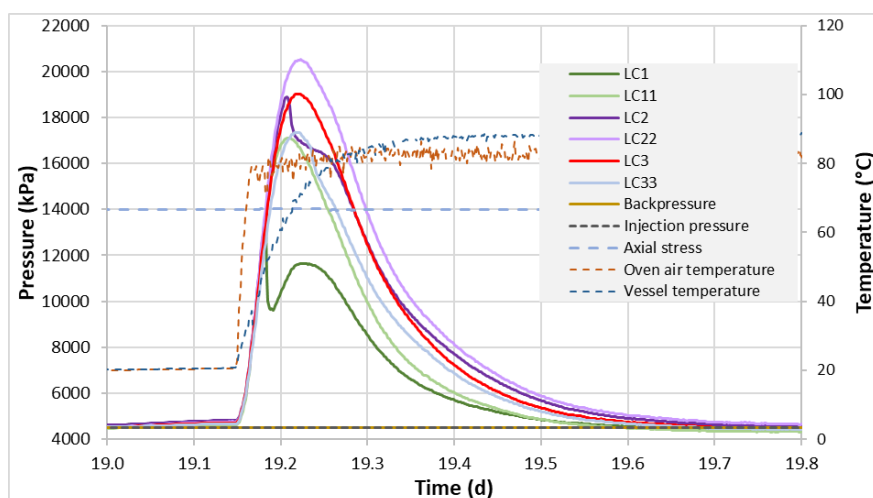


Figure 6 - FPR-20-013. Time evolution of water pressure during heating phase, stage [6]. Abrupt breaks in slope are suggestive of localised fracturing as porewater pressures approach or exceed the axial stress.

4.3.2 Test FPR-21-017 (Boom Clay, taken from core 2.3 76/77D, perpendicular to bedding)

Figure 7 shows sample FPR-21-017 following manufacture and X-ray CT imaging. Results from CT analysis show the high-density features with a particularly large, elongated feature visible in purple in Figure 7[B]. Following restressing and equilibration of the sample, Table 10, a constant head test was undertaken, stage [3], yielding a permeability of  $2.03 \times 10^{-19} \text{ m}^2$ . Porewater pressures were then allowed to decay, stage [4], before temperature was increased. Unfortunately, the oven was accidentally set incorrectly, and temperatures increased, peaking at around 189°C, before the test was terminated.

Table 10 - Experimental stages for test FPR-21-017. Stages denoted by EQ = equilibration, CHT = constant head test; TI = temperature increase and TD = temperature decrease.

Stage number	Type	Day	Injection pressure (MPa)	Backpressure (MPa)	Axial stress (MPa)	Oven temperature (°C)
1	Ramp	0	0-2.2	0-2.2	0-4.4	25
2	EQ	0.2	2.2	2.2	4.4	25
3	CHT	4.0	2.35	2.2	4.4	25
4	EQ	14.3	2.2	2.2	4.4	25
5	TI	18.2	2.2	2.2	4.4	189

4.3.3 Test FPR-21-024 (OPA perpendicular to bedding)

Upon manufacture, sample FPR-21-024 was placed in the test apparatus and restressed to the target effective stress. However, the seals on the axial ram failed, the sample was depressurised, and the test aborted.

#### 4.3.4 Test FPR-21-026 (OPA taken from core barrel BH4 (4.1), parallel to bedding)

In test FPR-21-026, the sample was gradually loaded to the target values (axial stress 6.0 MPa, porewater pressure 2.0 MPa). Axial stress and porewater pressure were then held constant for nearly 13 days before hydraulic testing began. Very quickly it became apparent that water was moving around the outside of the sample, bypassing the clay matrix, making it impossible to measure a realistic permeability. The difference in sample diameter between test FPR-20-013 and FPR-21-026 was 0.13mm, highlighting an issue with using K0 geometries to test relatively slow, low swelling lithified clays such as OPA. These issues were further explored in test FPR-22-067.

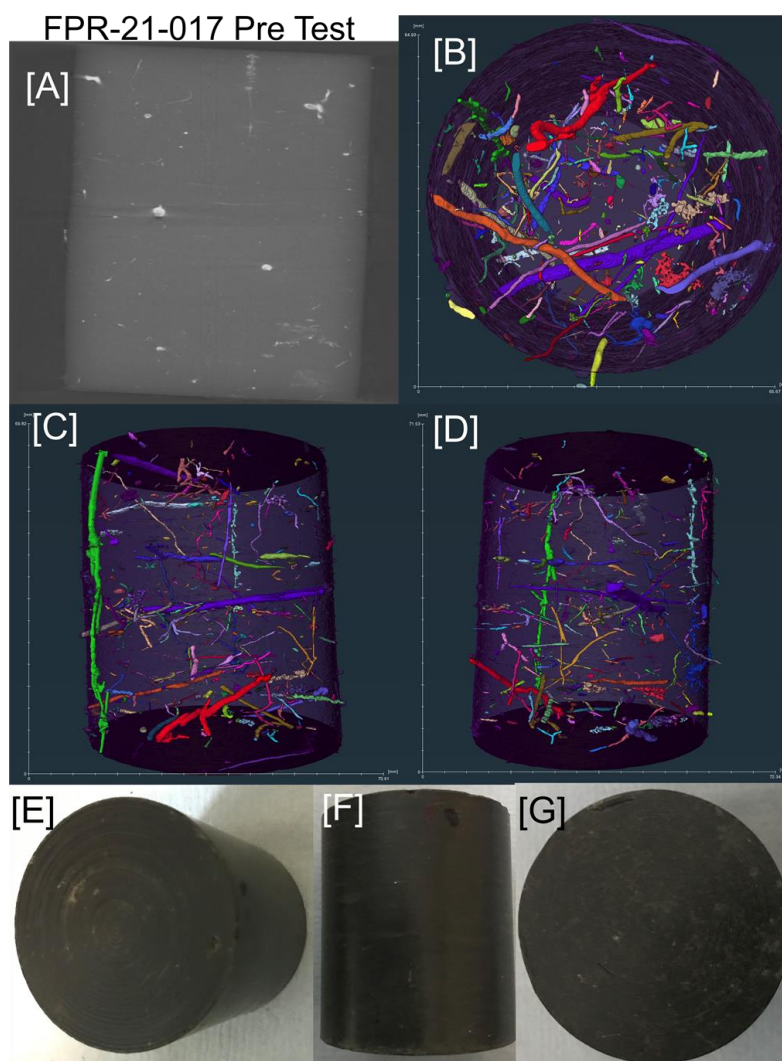


Figure 7 - Pre-test imaging of sample FPR-21-017. [A] Orthogonal CT; [B] CT image of features XY orientation; [C] CT image of features XZ orientation; [D] CT image of features YZ orientation; [E] injection face of sample [F] side view of sample; [G] backpressure face of sample.

#### 4.3.5 Test FPR-21-027 (OPA taken from core barrel BF1-4 (4.3), parallel to bedding)

This test comprised 8 experimental stages as described in Table 11. Following careful reloading and hydration of the sample, test stages [1] and [2], the intrinsic permeability was determined using a constant head test with two different injection pressures. Results from hydraulic testing are presented in Table 12. Data show a consistent intrinsic permeability of  $1.15 \times 10^{-19} \text{ m}^2$  at a nominal temperature of 21°C. These values are relatively high in comparison to previously measured values of the OPA and

probably reflect the damage (micro-fracturing) seen in Figure 8[E]. While sidewall flow cannot be eliminated, it seems unlikely this was the only cause as the difference in sample diameter between FPR-21-027 and FPR-20-013 was less than 0.03 mm. At the time of writing this report, no other possible causes for this behaviour could be identified. Following heating of the sample to around 83°C, test stage [8], intrinsic permeability was observed to decline significantly, yielding a value of  $4.86 \times 10^{-19} \text{ m}^2$ .

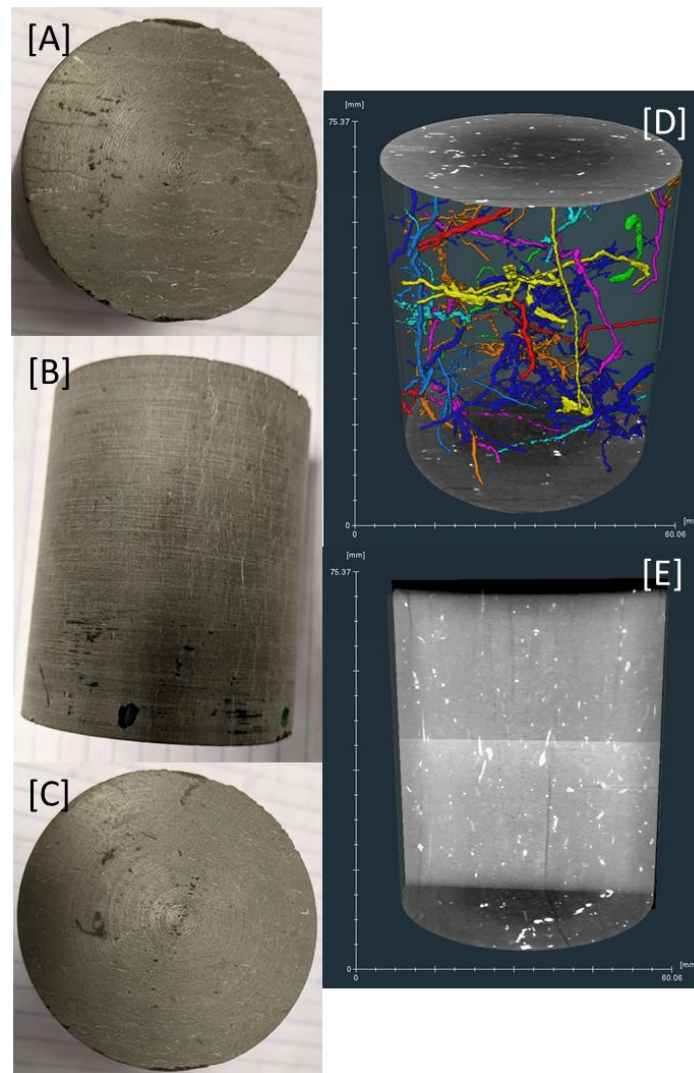


Figure 8 - Sample FPR-21-027 prior to testing. [A] to [C] backpressure, side view and injection end-face images of sample. [D] 3D macro x-ray CT image of sample showing mineralised bioturbation features (different colours represent connected features). [E] 2D x-ray image showing bedding plane fractures propagating into the sample.

Table 11 - Test FPR-21-027 – showing the type of experimental stage and boundary conditions for the test. Note Ramp = an increase in stress and/or porewater pressure; EQ = equilibration stage; CHT = constant head test and TI = temperature increase.

Stage no.	Type	Day	Injection pressure (MPa)	Backpressure (MPa)	Axial stress (MPa)	Average oven temperature (°C)
1	Ramp	0	0	0	0-2.0	21
2	Ramp	0.1	2.0	2.0	2-6.1	21
3	EQ	0.25	2.0	2.0	6.1	21
4	CHT	10.3	2.40	2.0	6.1	21
5	CHT	11.1	2.20	2.0	6.1	21
6	EQ	12.1	2.0	2.0	6.1	21
7	TI	12.2	2.0	2.0	6.1	83
8	CHT	17.1	2.21	2.0	6.1	83

Table 12 - Test FPR-21-027. Intrinsic permeability ( $k$ ) data from ambient and elevated temperature testing where  $k_{in}$  = permeability based on inflow,  $k_{out}$  = permeability based on outflow and  $k_{ave}$  = the average permeability based on inflow and outflow values.

Stage no.	Type	Day	Injection pressure (MPa)	Backpressure (MPa)	Axial stress (MPa)	Average oven temperature (°C)
1	Ramp	0	0	0	0-2.0	21
2	Ramp	0.1	2.0	2.0	2-6.1	21
3	EQ	0.25	2.0	2.0	6.1	21
4	CHT	10.3	2.40	2.0	6.1	21
5	CHT	11.1	2.20	2.0	6.1	21
6	EQ	12.1	2.0	2.0	6.1	21
7	TI	12.2	2.0	2.0	6.1	83
8	CHT	17.1	2.21	2.0	6.1	83

In test stage [7], oven temperature increased to around 83°C resulting in a rapid increase in porewater pressure measured along the cylindrical axis of the core, Figure 9. Unsurprisingly the highest pore pressures were observed at the mid-plane of the sample, peaking in pressure before the oven air temperature and thermocouple on the body of the vessel had thermally equilibrated. There is also considerable anisotropy in the remaining pressure traces which will likely relate to the fractured nature of the sample. While less pronounced, this anisotropy is visible when data is averaged across each plane of measurement, Figure 9[B]. Unfortunately, the orientation of the sample bedding in comparison to the pore pressure measurement plane was not recorded during the test and may therefore contribute to the asymmetry in pressure noted along the axis of the core. However, this unlikely to explain the difference in pressure observed at the same cross-sectional plane of the sample

(unless the sample was drilled at an angle i.e., inclined with respect to the bedding planes). More likely, damage, similar to the fractures seen in Figure 8[E] could explain such variation.

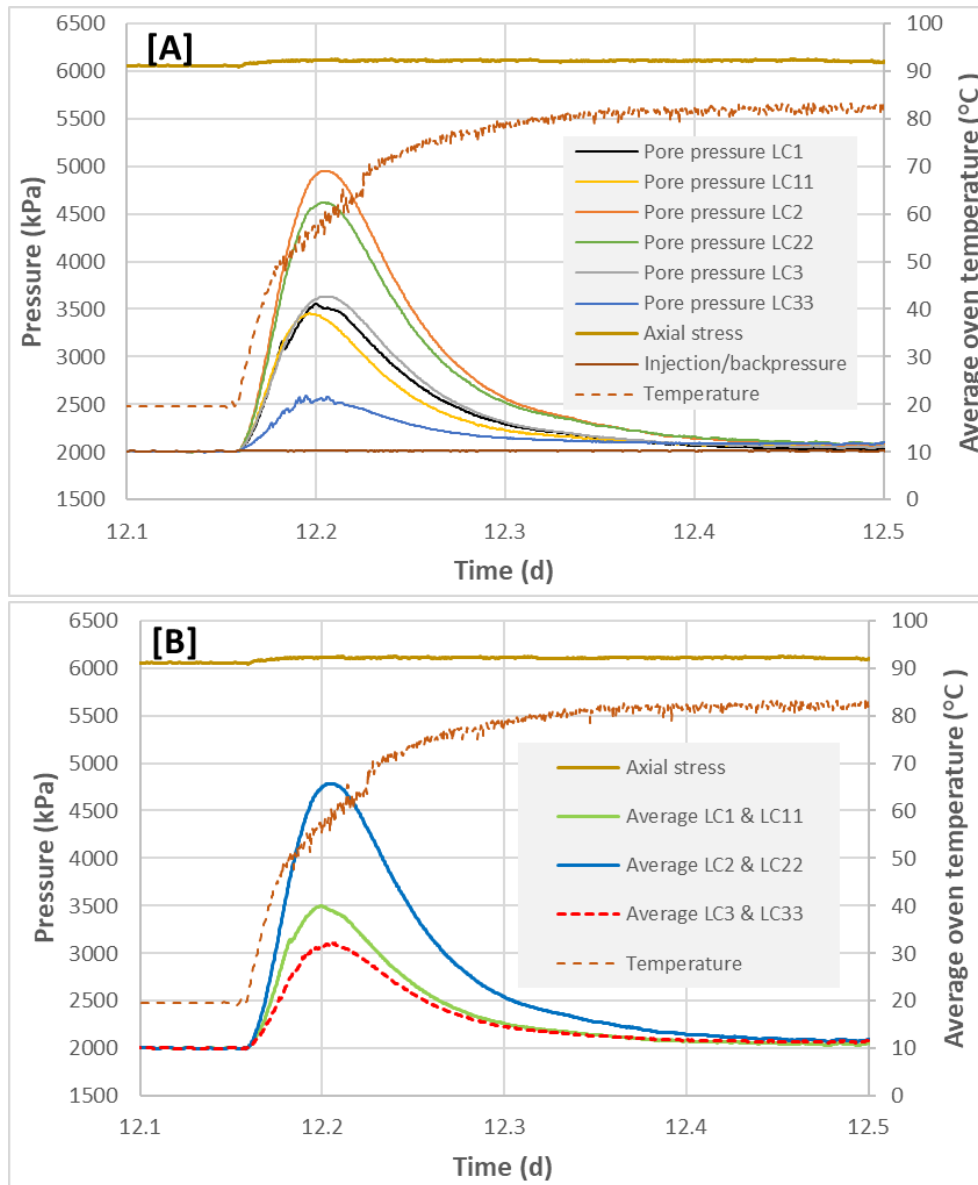


Figure 9 - Sample FPR-21-027: [[A] pore pressure development during heating to 90°C, test stage [7]. [B] average pore pressure values for test stage [7].

#### 4.3.6 Test FPR-21-051 (OPA taken from core barrel BF1-4 (5.7), parallel to bedding)

Figure 10 shows sample FPR-21-051 following manufacture, X-ray CT imaging and during installation into the apparatus. The dark lines indicate the bedding orientation, which means the pore pressure sensors are aligned parallel to the bedding direction. Apart from a thin section missing on the backpressure end of the sample, it appeared intact. This test comprised 14 experimental stages, Table 13. Following careful reloading and hydration of the sample, test stages [1] through [4], intrinsic permeability was determined using a constant head test in stages [5] and [7]. Results from hydraulic testing are presented in Table 14. As before, data yield a consistent intrinsic permeability with an average value of around  $5.31 \times 10^{-20} \text{ m}^2$  at a nominal temperature of 26°C. This value is much closer to expected intrinsic permeability values for OPA suggesting FPR-21-051 is a high-quality test sample

free from micro fracturing (as observed in test FPR-21-027). This is supported by the CT imaging results. In test stage [9], temperature was increased to around 88°C, like that in tests FPR-21-027 and FPR-20-013. As with previous tests, intrinsic permeability was remeasured, stage [10], this time yielding a value of  $3.41 \times 10^{-20} \text{ m}^2$ . This represents a small but significantly reduction in permeability. Upon completion of stage [10] and the subsequent re-equilibration stage [11], the temperature was returned to 26°C, test stage [12]. Permeability was measured for a fourth time, test stage [13], yielding a value of  $5.3 \times 10^{-20} \text{ m}^2$ , almost identical to the value obtained prior to heating.

Table 13 - Test FPR-21-051 showing the type of experimental stage and boundary conditions for the test. Note Ramp = an increase in stress and/or porewater pressure; EQ = equilibration stage; CHT = constant head test; TI = temperature increase and TD = temperature decrease.

Stage no.	Type	Day	Injection pressure (MPa)	Backpressure (MPa)	Axial stress (MPa)	Ave. oven temperature (°C)
1	Ramp	0	0	0	0-2	27
2	EQ	0.1	0	0	2	27
3	Ramp	1.0	0-2	0-2.0	2-6	27
4	EQ	1.9	2.0	2.0	6	26
5	CHT	11.9	2.25	2.0	6	26
6	EQ	14.9	2.0	2.0	6	26
7	CHT	17.8	2.25	2.0	6	26
8	EQ	21.2	2.0	2.0	6	26
9	TI	21.8	2.0	2.0	6	88
10	CHT	22.8	2.25	2.0	6	88
11	EQ	23.8	2.0	2.0	6	88
12	TD	24.1	2.0	2.0	6	26
13	CHT	27.0	2.25	2.0	6	26
14	EQ	27.9	2.0	2.0	6	26

Table 14 - Test FPR-21-051. Intrinsic permeability (k) data from ambient and elevated temperature testing where  $k_{in}$  = permeability based on inflow,  $k_{out}$  = permeability based on outflow and  $k_{ave}$  = the average permeability based on inflow and outflow values.

Test stage	Ave. oven temperature (°C)	Intrinsic permeability, k, (m <sup>2</sup> )		
		$k_{in}$ (m <sup>2</sup> )	$k_{out}$ (m <sup>2</sup> )	$k_{ave}$ (m <sup>2</sup> )
5	26	$5.85 \times 10^{-20}$	$4.82 \times 10^{-20}$	$5.34 \times 10^{-20}$
7	26	$5.71 \times 10^{-20}$	$4.84 \times 10^{-20}$	$5.28 \times 10^{-20}$
10	88	$3.51 \times 10^{-20}$	$3.30 \times 10^{-20}$	$3.41 \times 10^{-20}$
13	26	$5.64 \times 10^{-20}$	$4.86 \times 10^{-20}$	$5.25 \times 10^{-20}$

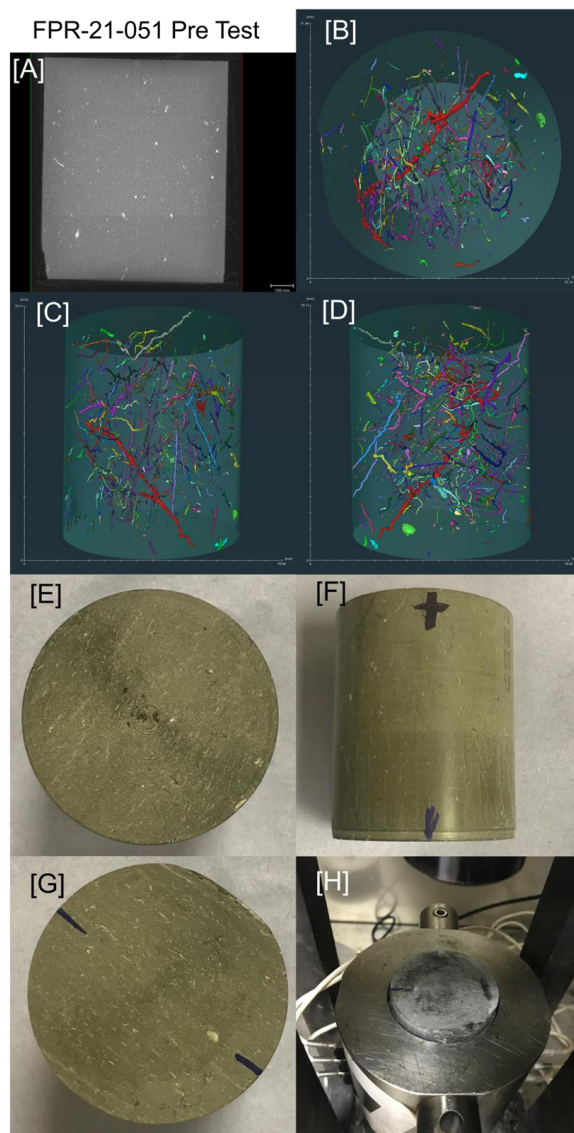


Figure 10 - Sample FPR-21-051 prior to testing. [A] Orthogonal CT; [B] CT image of features XY orientation; [C] CT image of features XZ orientation; [D] CT image of features YZ orientation; [E] injection face of sample [F] side view of sample; [G] backpressure face of sample; [H] an image of the sample installed in the confining vessel with sample bedding aligned to the apparatus measurement plane (denoted by the black line).

Figure 11[A] shows the pore pressure response for sample FPR-21-051 as temperature was increased from 26 to 88°C, test stage [9] Table 13. As in Figure 9, porewater pressures rapidly increase and peak in pressure before the peak temperature is applied. Again, the development of porewater pressure exhibits significant anisotropy when viewed on the scale of each sensor and this remains when values are averaged across each measurement plane, Figure 11[B]. Like before, highest porewater pressure is observed at the mid-plane of the sample at LC22, with highest pressures focussed on the side of the sample closest to LC11, LC22 and LC33. As the sample bedding was orientated in the same vertical plane as the pressure sensors on the apparatus, it is unclear why pressure is preferentially higher on one side of the sample. The anisotropy in sensor output is clear in Figure 11[A].

Unlike test FPR-21-027, porewater pressure at LC22 and LC33 significantly exceed the axial confining stress applied to the sample. Again, this reflects the test geometry which prevents radial expansion of the sample. However, it would be impossible to measure the distribution and development of thermally induced porewater pressure in any other type of readily available apparatus.

Clearly, under representative in situ conditions, the rapid generation of porewater pressure from thermal expansion of porewater is capped by the sum of the total stress and tensile strength of the host rock. As the tensile strength of most mudrocks is relatively low, these experiments suggest thermally induced fracturing of the host rock is possible if subjected to rapid loading.

Similarly, to test FPR-21-027, the duration of the thermally induced porewater pressure pulse is relatively short, with pressure returning to the reference value (of 2.0 MPa) within 0.5 days. The fact that there is no sign of hydraulic damage when permeability was remeasured in test stage [13], could again reflect the boundary conditions of the test, i.e., the same radial constraint which prevents sample swelling during heating, also prevents mode 1 or mode 2 fracturing from occurring.

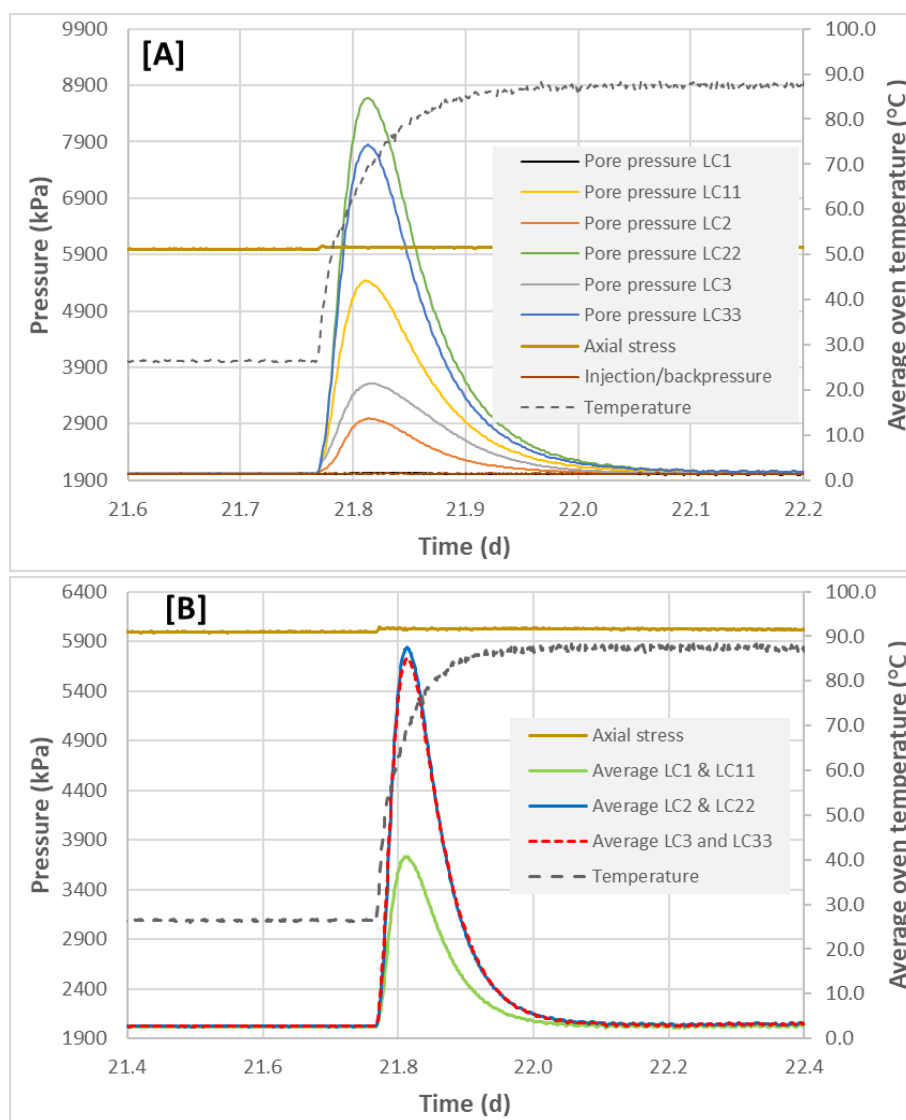


Figure 11 - Sample FPR-21-051: [A] pore pressure development during heating to 88°C, test stage [9]. [B] average pore pressure values for test stage [9].

4.3.7 Test FPR-21-052 (OPA taken from core barrel BF1-4 (5.8), parallel to bedding)

Figure 12 shows photographic and X-ray CT images of sample FPR-21-052 following manufacture and installation into the apparatus. While the bedding planes are clearly visible, the sample appears to be in good condition. Again, this test is being carried out on a sample with the bedding orientated parallel to the axis of the core.

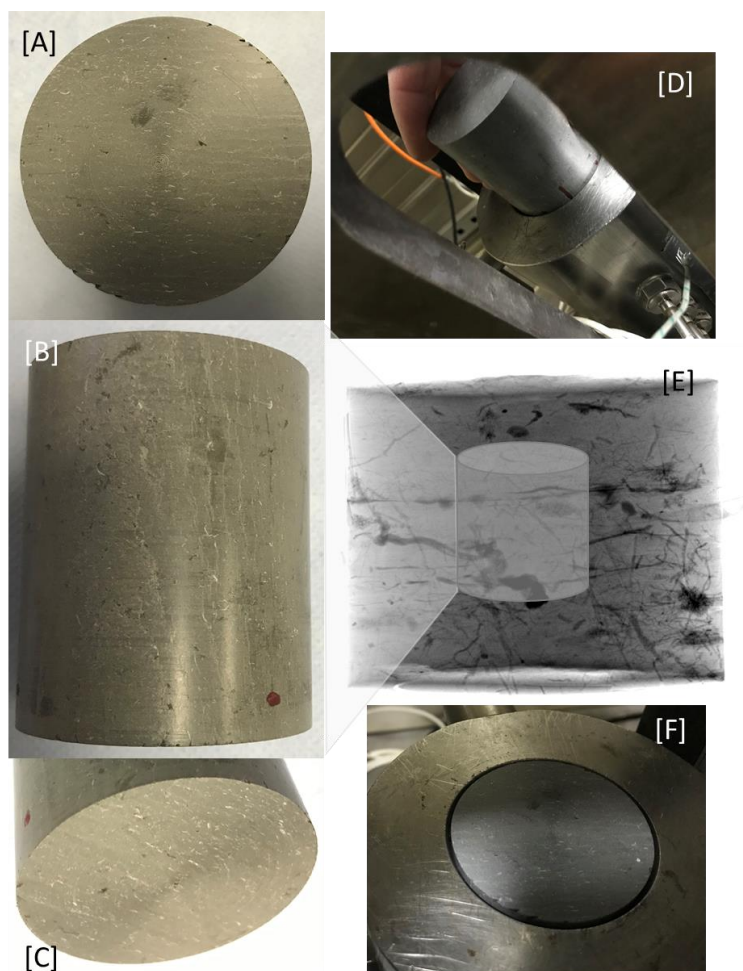


Figure 12 - Sample FPR-21-052 prior to testing. [A], [B] and [C] are optical images of the pre-test sample (the red dot marks the injection end of the core). [D] is an image of the sample partly installed in the confining vessel with sample bedding aligned to the apparatus measurement plane (denoted by the black line). [E] is an X-ray CT image of the entire core from which the test sample originated (location is for illustrative purposes only). [F] is an image of the sample fully installed into the confining vessel.

The test comprised 45 experimental stages, as shown in Table 15 and Table 16. Following careful reloading and hydration of the sample, test stages [1] through [4], intrinsic permeability was determined using a constant head test in stage [5]. Results from hydraulic testing are presented in Table 17, with an initial intrinsic permeability of  $5.27 \times 10^{-20} \text{ m}^2$  measured at a nominal temperature of 26°C. This value is remarkably similar to that of test FPR-21-051 and is also in line with expected values for the OPA. The data also suggests sample FPR-21-052 is free of damage.

Table 15 - Test FPR-21-052 (stages 1 to 30) showing the type of experimental stage and boundary conditions for the test. Note Ramp = an increase in stress and/or porewater pressure; EQ = equilibration stage; CHT = constant head test; TI = temperature increase and TD = temperature decrease. Test remains on-going.

Stage number	Type	Day	Injection pressure (MPa)	Backpressure (MPa)	Axial stress (MPa)	Average oven temperature (°C)
1	Ramp	0	0	0	0-4.0	26
2	EQ	0.5	0	0	4.0	26
3	Ramp	1.0	0-2.0	0-2	4.0-6.0	26
4	EQ	1.1	2.0	2.0	6.0	26
5	CHT	10.1	2.24	2.0	6.0	26
6	EQ	13.0	2.0	2.0	6.0	26
7	TI	14.1	2.0	2.0	6.0	90
8	CHT	15.2	2.24	2.0	6.0	90
9	EQ	16.3	2.0	2.0	6.0	90
10	TD	17.0	2.0	2.0	6.0	26
11	CHT	21.2	2.24	2.0	6.0	26
12	EQ	24.1	2.0	2.0	6.0	26
13	TI	25.0	2.0	2.0	6.0	71
14	CHT	26.1	2.24	2.0	6.0	71
15	EQ	28.2	2.0	2.0	6.0	71
16	TD	29.2	2.0	2.0	6.0	26
17	CHT	31.0	2.24	2.0	6.0	26
18	EQ	32.0	2.0	2.0	6.0	26
19	TI	35.1	2.0	2.0	6.0	51
20	CHT	36.3	2.24	2.0	6.0	51
21	EQ	37.1	2.0	2.0	6.0	51
22	TD	37.2	2.0	2.0	6.0	26
23	CHT	42.3	2.24	2.0	6.0	26
24	EQ	44.0	2.0	2.0	6.0	26
25	Ramp	46.1	2.0	2.0	14.0	26
26	CHT	50.1	2.24	2.0	14.0	26
27	EQ	51.3	2.0	2.0	14.0	26
28	TI	52.0	2.0	2.0	14.0	90
29	CHT	56.0	2.22	2.0	14.0	90
30	EQ	58.2	2.0	2.0	14.0	90

Following heating to 90°C, test stage [7], intrinsic permeability was remeasured, stage [8], this time yielding a value of  $3.62 \times 10^{-20} \text{ m}^2$ . Similar to previous tests, permeability was observed to decrease on heating, Table 15. Upon completion of stage [8] and the subsequent re-equilibration stage [9], the temperature was returned to 26°C, test stage [10]. Permeability was measured for a fourth time, test stage [11], yielding a value of  $5.73 \times 10^{-20} \text{ m}^2$ , and as shown in previous tests the permeability was very similar to that measured prior to heating.

This recovery of the pre-heating permeability indicates that no significant damage occurred to the samples due to heating. Therefore, it was decided to delineate permeability as a function of temperature following the same careful methodical approach embodied in the initial characterisation of permeability. This has the added advantage that all data can be directly compared.

In this way, permeability was measured at approximately 71°C and 51°C, test stages [14] and [20] respectively, as well as at 26°C between each test, stages [17] and [23]. When the data is plotted, Table 15, a systematic trend of decreasing permeability is observed as temperature increases. While there is a small amount of dispersion, the data clearly shows that on reducing temperature to 26°C, similar values of permeability are obtained. As such, data indicates no obvious sign of hydraulic damage occurred during heating of the OPA samples to 90°C.

Table 16 - Test FPR-21-052 (stages 30 to 45) showing the type of experimental stage and boundary conditions for the test. Note Ramp = an increase in stress and/or porewater pressure; EQ = equilibration stage; CHT = constant head test; TI = temperature increase and TD = temperature decrease. Test remains on-going.

Stage number	Type	Day	Injection pressure (MPa)	Backpressure (MPa)	Axial stress (MPa)	Average oven temperature (°C)
31	TD	59.1	2.0	2.0	14.0	90
32	CHT	63.0	2.24	2.0	14.0	26
33	EQ	64.1	2.0	2.0	14.0	26
34	TI	65.0	2.0	2.0	14.0	71
35	CHT	66.4	2.24	2.0	14.0	71
36	EQ	67.0	2.0	2.0	14.0	71
37	TD	73.1	2.0	2.0	14.0	26
38	CHT	71.4	2.24	2.0	14.0	26
39	EQ	76.2	2.0	2.0	14.0	26
40	TI	77.0	2.0	2.0	14.0	51
41	CHT	79.3	2.24	2.0	14.0	51
42	EQ	84.2	2.0	2.0	14.0	51
43	TD	85.1	2.0	2.0	14.0	26
44	CHT	88.3	2.24	2.0	14.0	26
45	EQ	90.0	2.0	2.0	14.0	26

Table 17 - Test FPR-21-052 – Intrinsic permeability ( $k$ ) data from ambient and elevated temperature testing where  $k_{in}$  = permeability based on inflow,  $k_{out}$  = permeability based on outflow and  $k_{ave}$  = the average permeability based on inflow and outflow values. Inflow data from stage [5] was not available due to a leakage from the pipework during that phase of testing.

Stage number	Temperature (°C)	Intrinsic permeability, $k$ , ( $m^2$ )		
		$k_{in}$ ( $m^2$ )	$k_{out}$ ( $m^2$ )	$k_{ave}$ ( $m^2$ )
5	26	-	$5.27 \times 10^{-20}$	$5.27 \times 10^{-20}$
8	90	$4.00 \times 10^{-20}$	$3.24 \times 10^{-20}$	$3.62 \times 10^{-20}$
11	26	$6.92 \times 10^{-20}$	$4.54 \times 10^{-20}$	$5.73 \times 10^{-20}$
14	71	$4.39 \times 10^{-20}$	$3.53 \times 10^{-20}$	$3.96 \times 10^{-20}$
17	26	$8.11 \times 10^{-20}$	$3.59 \times 10^{-20}$	$5.85 \times 10^{-20}$
20	51	$4.09 \times 10^{-20}$	$4.94 \times 10^{-20}$	$4.51 \times 10^{-20}$
23	26	$5.69 \times 10^{-20}$	$5.04 \times 10^{-20}$	$5.37 \times 10^{-20}$
26	26	$4.74 \times 10^{-20}$	$5.82 \times 10^{-20}$	$5.28 \times 10^{-20}$
29	90	$3.40 \times 10^{-20}$	$3.36 \times 10^{-20}$	$3.38 \times 10^{-20}$
32	26	$6.16 \times 10^{-20}$	$4.69 \times 10^{-20}$	$5.43 \times 10^{-20}$
35	71	$3.90 \times 10^{-20}$	$3.89 \times 10^{-20}$	$3.89 \times 10^{-20}$
38	26	$6.60 \times 10^{-20}$	$5.48 \times 10^{-20}$	$6.04 \times 10^{-20}$
41	51	$5.17 \times 10^{-20}$	$3.28 \times 10^{-20}$	$4.22 \times 10^{-20}$
44	26	$7.08 \times 10^{-20}$	$5.00 \times 10^{-20}$	$6.04 \times 10^{-20}$

In test stage [25], axial stress was slowly increased from 6.0 MPa to 14.0 MPa while the backpressure was held constant. Thus, the effective stress on the sample increased from 4 MPa to 12 MPa. Intrinsic permeability was then remeasured at this higher effective stress, stage [26], yielding a value of  $5.28 \times 10^{-20} m^2$ . While fractionally smaller than the previous average value for 26°C, it is very similar, suggesting only a minor reduction in permeability occurred due to the increase in effective stress. This is not surprising given the indurated and over consolidated nature of the material. As before, the sample was then subjected to the same thermal history as that undertaken at the lower effective stress, and permeability remeasured, with the data presented in Table 17.

Data for 90°C, 71°C and 51°C, i.e., test stages [29], [35] and [41] respectively, for the higher effective stress have been plotted with data for the lower effective stress, Figure 13. Examination of the data suggests a small offset in values between those measured at 4 MPa effective stress and those at 12 MPa effective stress. However, the difference is small, and the trend is impacted by the larger range in values when permeability is repeatedly remeasured at 26°C.

During each thermal loading/unloading stage, the change in porewater pressure along the axis of the sample was measured. Example data for steps [7], [13] and [19] are presented in Figure 14[A], [B] and [C]. As with previous tests, porewater pressures rapidly increase and, similar to results from tests FPR-21-027 and FPR-21-051, peak in pressure before the maximum average oven temperature is applied. Again, the development of porewater pressure exhibits significant anisotropy when viewed on the scale of each sensor. Like before, highest porewater pressures are observed at the mid-plane of the sample.

However, when sensor outputs across each plane of measurement are averaged, Figure 14[D], [E] and [F], a clear picture emerges with pressures either side of the sample mid-plane approximately equal, indicating hydraulic symmetry and little if any significant anisotropy when viewed at the length-scale of the sample. Not only were average pressures between measurement planes LC1 and LC3 approximately equal, but the shape of the pressure transient was also almost identical, again suggesting hydraulic homogeneity on the scale of the sample was observed.

Examination of the data in Figure 15[A] shows that at temperatures below 60°C the rapid application of temperature does not result in the generation of porewater pressure values (at the mid-plane of the sample) which are higher than the applied axial stress. However, when the sample heating approaches 71°C (and beyond), porewater pressures at the mid-plane increases above the axial stress. As stated before, under true in situ conditions, the rapid generation of pore pressure from thermal expansion of porewater would be capped by the sum of the total stress and tensile strength of the host rock. However, as also stated, the tensile strength of most mudrocks is low, indicating thermally induced fracturing of the host rock could be possible if subject to rapid loading to temperatures around 71°C and above.

Following the increase in axial stress from 6 to 14 MPa in test stage [25] and the re-heating of the sample to 90°C in stage [28] and then 51°C stage [34], all porewater pressures were observed to increase, Figure 15[B]. However, this time peak pressure values remained significantly below that of the new axial stress, indicating a subtle (and probably complex) coupling between the thermal expansion of porewater, the creation of over-pressures and the applied axial stress.

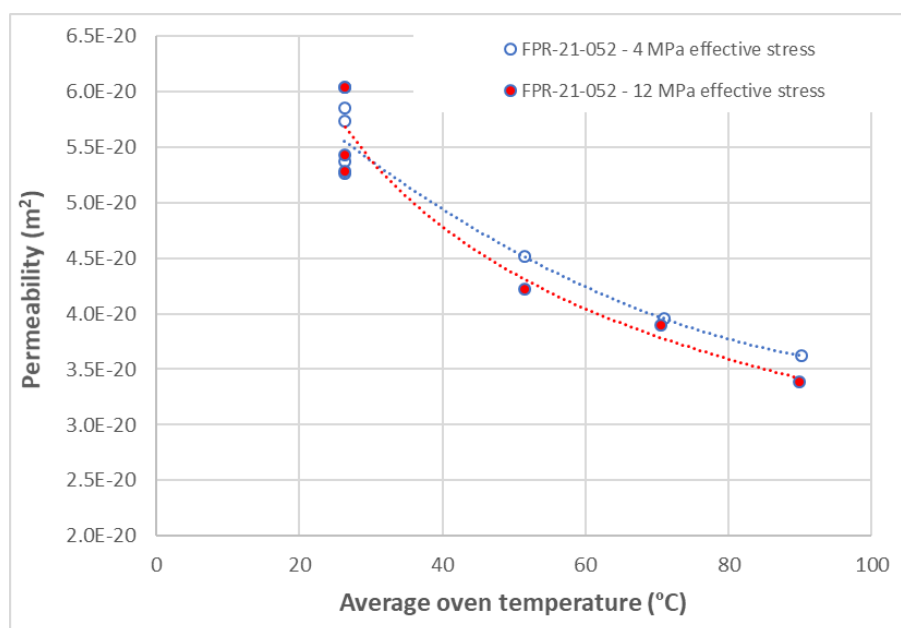


Figure 13 - Permeability versus temperature for sample FPR-21-052 at effective stresses of 4 MPa (blue circles) and 12 MPa (red dots).

The comparison of peak porewater pressures at differing temperatures measured under two values of axial load, Figure 15[C], illustrates the impact of axial stress on peak porewater pressures. As axial load increases, so does the peak porewater pressure observed at each measuring plane along the sample. At temperatures of 70°C and upwards, the difference in the peak values becomes more pronounced and continues to increase as temperature rises. When viewed from a repository context, the data indicates the development of thermally induced porewater pressures will increase with depth. Hence constructing a repository at a depth where peak thermally induced porewater pressures remain below in situ stress, would ensure host rock integrity.

As with all tests analysis of axial deformation data remains ongoing and therefore cannot be included in this summary report. Also excluded is the analysis of the porewater pressure data for decrements in temperature. However, all this information and analyses will be included in a future publication.

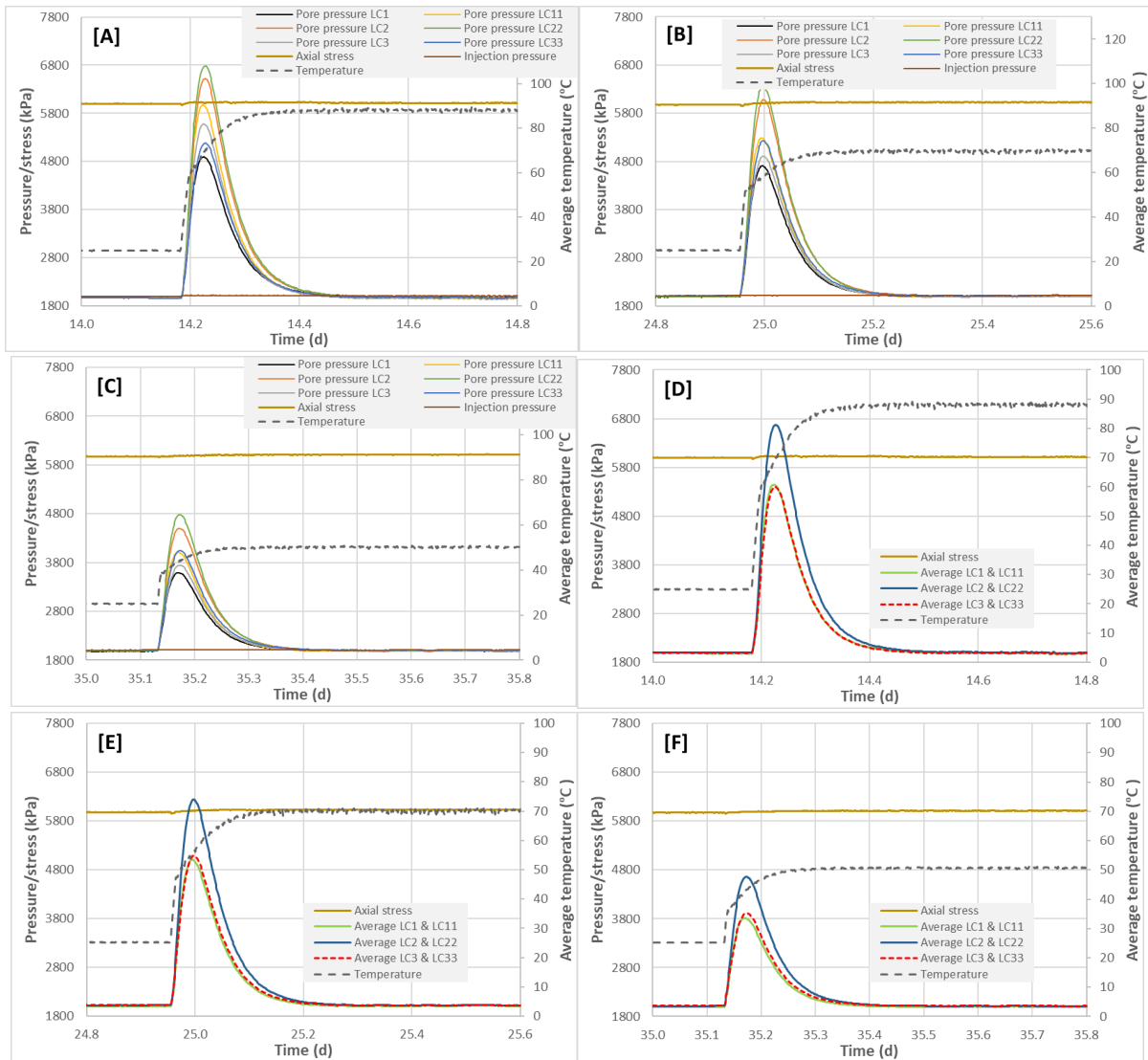


Figure 14 - Sample FPR-21-052: pore pressure development during heating. [A], [B] and [C] show individual sensor values on heating to 89°C, test stage [7], 69°C, test stage [13] and 50°C, test stage [17] respectively. [D], [E] and [F] show average pressure data across each plane of measurement.

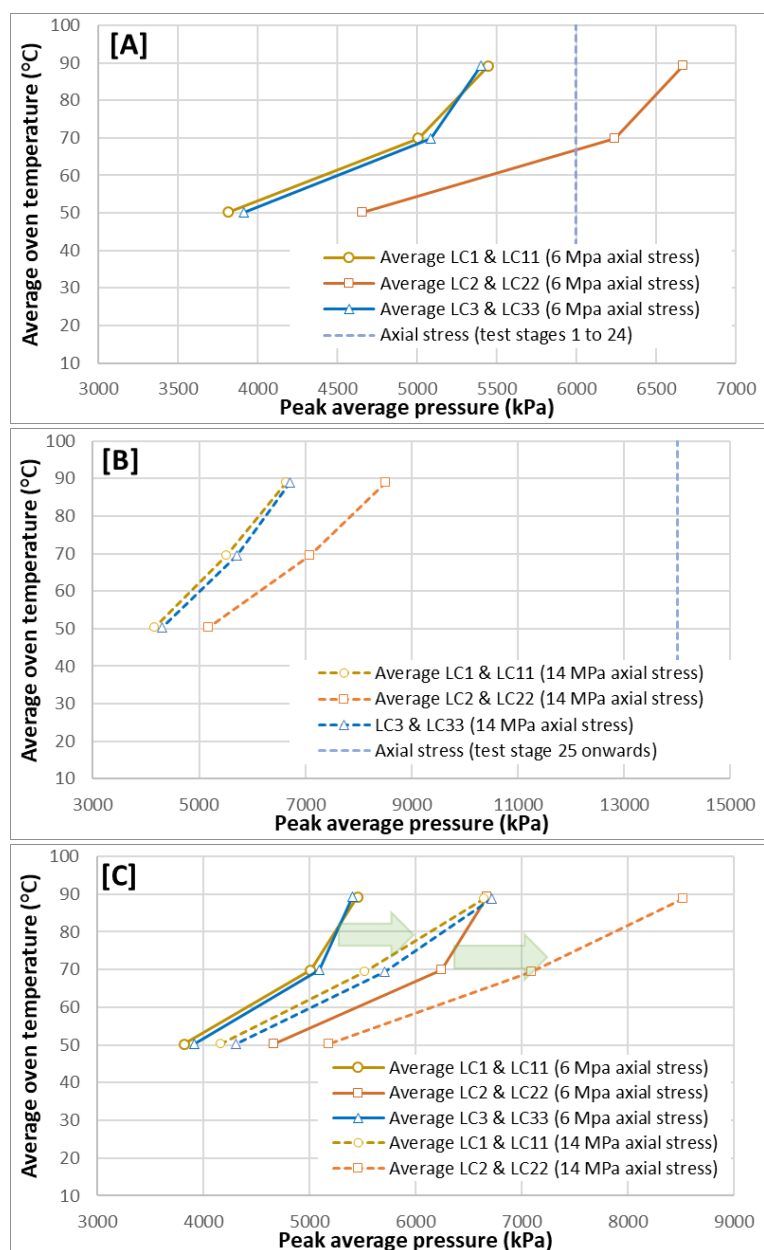


Figure 15 - Sample FPR-21-052: [A] average peak pressure data for test stages [7], [13] and [17] under an axial stress of 6 MPa. [B] average peak pressures for test stages [28], [34] and [40] following the increase in axial stress to 14 MPa. [C] comparing data from graphs [A] and [B] illustrates the impact of increasing axial stress on peak pressures, showing the difference becomes more pronounced at temperature increases.

#### 4.3.8 Test FPR-22-025 (OPA taken from core barrel BF1-3 (8.4), perpendicular to bedding)

Figure 16 shows sample FPR-22-025 following manufacture, X-ray CT imaging and during installation into the apparatus. Test FPR-22-025 was cut perpendicular to bedding and comprised 25 stages. As shown in Table 18 the main measurement phase was performed at an elevated axial stress of 14.4 MPa. However, following installation of the sample into the apparatus, stage [1], axial load was initially increased to 9.9 MPa, stage [2]. This was followed by a short equilibration period, stage [3], before axial stress and porewater pressure were increased, stage [4], to 14.4 MPa and 2.0 MPa respectively. However, during stage [5] an accidental pulse of porewater pressure was applied to the sample, peaking at 9.0 MPa before declining to 0.1 MPa, which lasted in total less than 4 hours,

Figure 17. Given no obvious damage had been caused to previous samples when exposed to high porewater pressures were generated during heating, it was fair to assume sample FPR-22-025 was undamaged, and the test could continue. Porewater pressure was increased in a single step, stage [7], to 2.0 MPa, reestablishing the boundary conditions for the test.

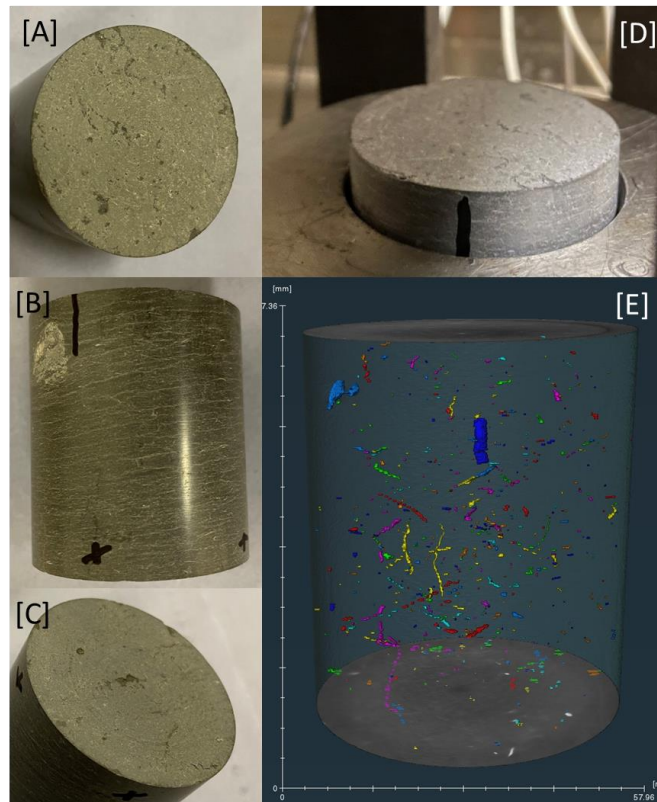


Figure 16 - Sample FPR-22-025 prior to testing. [A], [B] and [C] are optical images of the pre-test sample (the black cross marks the injection end of the core). [D] is an image of the sample partly installed in the confining vessel with black line aligned to the apparatus measurement plane. [E] is an X-ray CT image of the sample highlighting some of the higher density features.

The initial permeability of the sample was measured in test stage [8] yielding a value of  $2.1 \times 10^{-20} \text{ m}^2$ , Table 19. This is very similar to that of test FPR-21-027, Table 12, and supports the data presented in Figure 13 which indicates the permeability of OPA exhibits only a minor sensitive to confining stress across for the range in stresses tested within this study. Following a period of equilibration, stage [9], the temperature in the oven was increased to  $84^\circ\text{C}$ , stage [10]. Permeability was remeasured, stage [11], and was observed to decrease slightly yielding a value  $1.0 \times 10^{-20} \text{ m}^2$ . Following another period of equilibration to allow porewater pressures to dissipate, stage [12], temperature in the oven was decreased back to the start value of  $26^\circ\text{C}$ .

Sample FPR-22-025 was then subjected to two further temperature cycles of  $66^\circ\text{C}$  and  $49^\circ\text{C}$ , test stages [16] and [22] respectively, with permeability measured before (stages [14] and [20]), during (stages [17] and [23]) and after (stage [20]) each thermal stage. Unfortunately, the test was prematurely finished before a final permeability measurement could be made following test stage [25]. Permeability values are presented in Table 19. Examination of the data suggests a systematic trend of decreasing permeability with increasing temperature. While there is also some dispersion in the permeability values measured at  $26^\circ\text{C}$ , the cause for this is unclear. However, if the values from stages [8], [14] and [20] are averaged and plotted with the data from the constant head tests

performed at elevated temperature, (stages [11], [17] and [23]), then the trend in permeability as a function of temperature becomes clear, Figure 19.

Table 18 - Test FPR-22-025 showing the type of experimental stage and boundary conditions for the test. Note Ramp = an increase in stress and/or porewater pressure; EQ = equilibration stage; CHT = constant head test; TI = temperature increase and TD = temperature decrease. Test remains on-going.

Stage number	Type	Day	Injection pressure (MPa)	Backpressure (MPa)	Axial stress (MPa)	Average oven temperature (°C)
1	EQ	0	0	0	0	26
2	Ramp	1.1	0	0	9.9	26
3	EQ	1.2	0	0	9.9	26
4	Ramp	2.9	0-2.0	0-2.0	14.4	26
5	EQ	3.1	2.0	2.0	14.4	26
6	EQ	3.1	Accidental	Accidental	14.4	26
7	Step	7.8	2.0	2.0	14.4	26
8	CHT	10.8	2.25	2.0	14.4	26
9	EQ	27.8	2.0	2.0	14.4	26
10	TI	29.1	2.0	2.0	14.4	84
11	CHT	34.9	2.25	2.0	14.4	84
12	EQ	49.1	2.0	2.0	14.4	84
13	TD	50.9	2.0	2.0	14.4	26
14	CHT	58.9	2.25	2.0	14.4	26
15	EQ	62.8	2.0	2.0	14.4	26
16	TI	64.9	2.0	2.0	14.4	66
17	CHT	67.0	2.25	2.0	14.4	66
18	EQ	69.9	2.0	2.0	14.4	66
19	TD	71.0	2.0	2.0	14.4	26
20	CHT	80.9	2.25	2.0	14.4	26
21	EQ	83.9	2.0	2.0	14.4	26
22	TI	85.8	2.0	2.0	14.4	49
23	CHT	93.8	2.15	1.85	14.4	49
24	EQ	100.0	2.0	2.0	14.4	49
25	TD	100.9	2.0	2.0	14.4	26

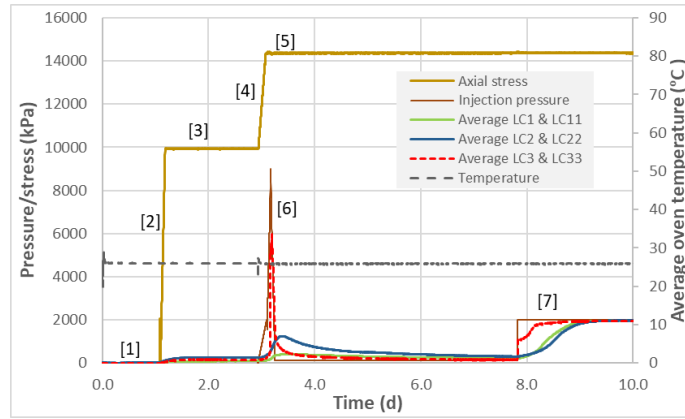


Figure 17 - Sample FPR-22-025 showing loading of the sample, the application of an accidental porewater pressure pulse and the subsequent step in porewater pressure. Values in paratheses represent test stage numbers.

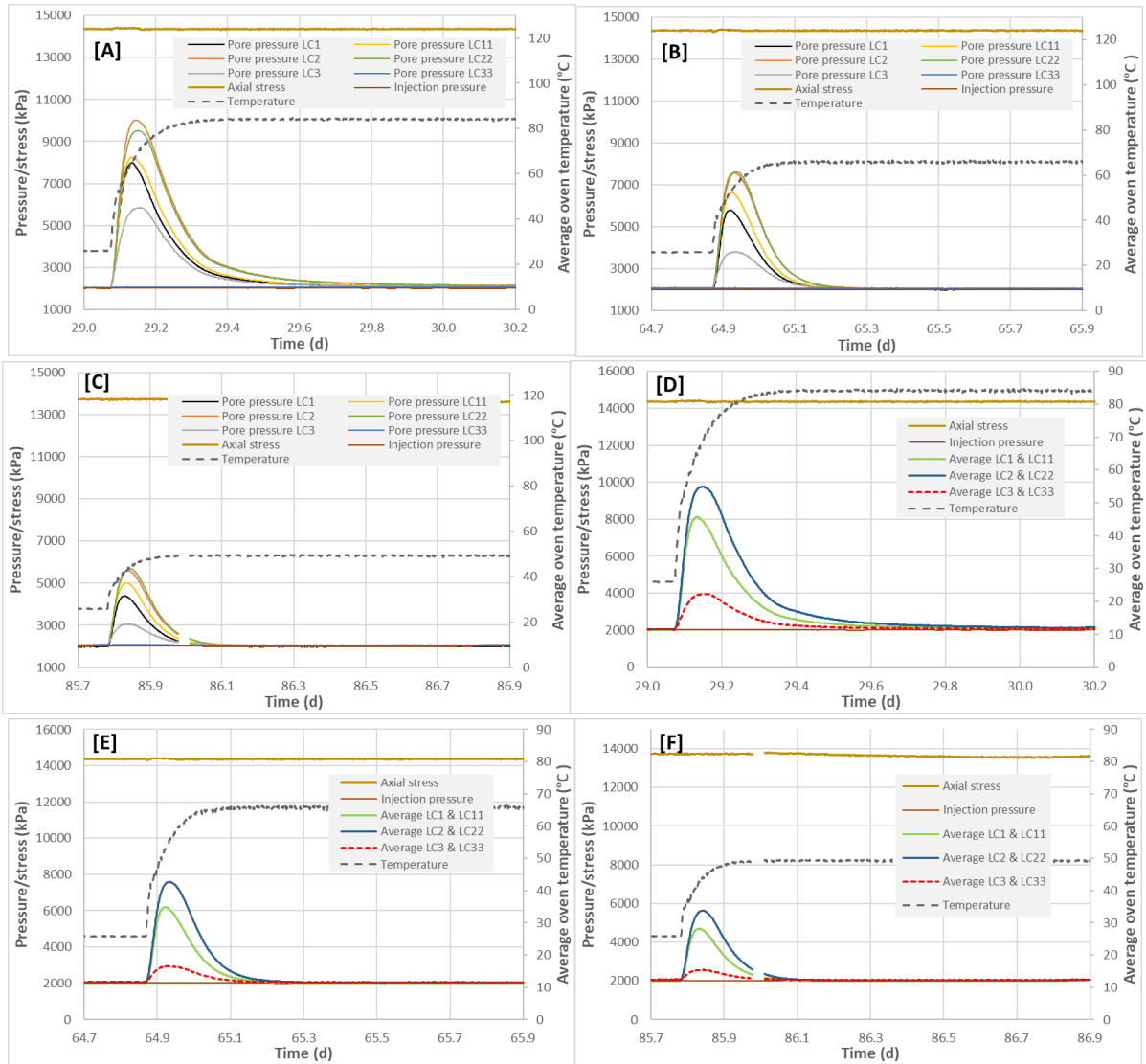


Figure 18 - Sample FPR-22-25: pore pressure development during heating. [A], [B] and [C] show individual sensor values on heating to 84°C, test stage [10], 66°C, test stage [16] and 49°C, test stage [22] respectively. [D], [E] and [F] show average pressure data across each plane of measurement.

Examination of the data in Figure 18[A], [B] and [C] shows that peak porewater pressures caused by heating of the sample remain substantially lower than the applied axial stress. This is similar in response to test FPR-21-052 when subject to similar axial stresses. The fact that thermally induced porewater pressures consistently remain below the total stress in all samples where axial loads are high, indicates it would be possible, knowing the heat output of the waste, to calculate a repository depth below which thermally induced porewater pressures would always remain lower than the in-situ stress. This has obvious advantages for the management of porewater pressures, the integrity of the host rock and ultimately, safety assessment.

The average porewater pressures induced during heating are presented in Figure 18[D], [E] and [F]. Inspection of the data shows that the magnitude and duration of the peak pressures increases with increasing temperature. The data also suggests significant anisotropy in the development and distribution of pressure. This may relate to the slight dip of the bedding planes with respect to the cylindrical axis of the core visible in Figure 16[B]. But, without more instrumentation on the pressure vessel to better quantify the distribution of porewater pressure, it is difficult to explain, with certainty, the cause for this behaviour.

Table 19 - Test FPR-22-025. Intrinsic permeability (k) data from ambient and elevated temperature testing where  $k_{in}$  = permeability based on inflow,  $k_{out}$  = permeability based on outflow and  $k_{ave}$  = the average permeability based on inflow and outflow values.

Stage number	Average oven temperature (°C)	Intrinsic permeability, k, (m <sup>2</sup> )		
		$k_{in}$ (m <sup>2</sup> )	$k_{out}$ (m <sup>2</sup> )	$k_{ave}$ (m <sup>2</sup> )
8	26	2.05x10 <sup>-20</sup>	2.04x10 <sup>-20</sup>	2.04x10 <sup>-20</sup>
11	84	1.06x10 <sup>-20</sup>	1.00x10 <sup>-20</sup>	1.03x10 <sup>-20</sup>
14	26	3.84x10 <sup>-20</sup>	2.74x10 <sup>-20</sup>	3.29x10 <sup>-20</sup>
17	66	1.56x10 <sup>-20</sup>	1.51x10 <sup>-20</sup>	1.54x10 <sup>-20</sup>
20	26	2.46x10 <sup>-20</sup>	2.31x10 <sup>-20</sup>	2.39x10 <sup>-20</sup>
23	49	2.27x10 <sup>-20</sup>	1.67x10 <sup>-20</sup>	1.97x10 <sup>-20</sup>

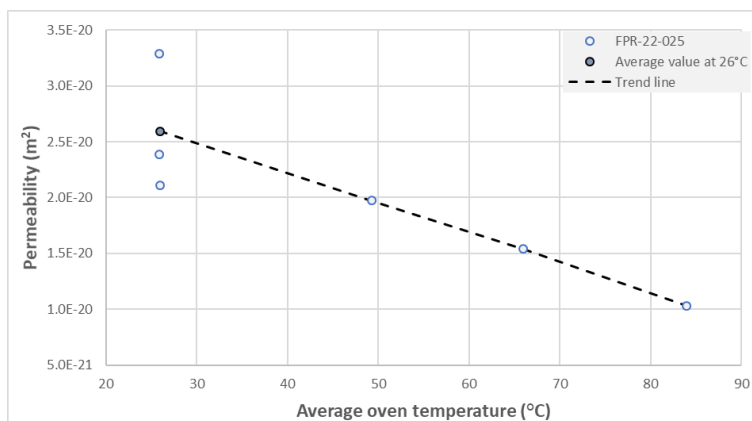


Figure 19 - Sample FPR-22-025: permeability as a function of temperature.

4.3.9 Test FPR-22-067 (OPA taken from core barrel BF1-3 (4.3), perpendicular to bedding)

Figure 20 shows X-ray CT images [A] through [D] after testing of sample FPR-22-067 and optical images [E] through [G] prior to testing. The CT data indicate higher density features are generally concentrated in a single horizon visible in Figure 20[C] and [D]. As with previous tests, sample FPR-22-067 was initially stressed, stage [1], to apply an effective stress of 3.9 MPa. Following an equilibration period, the axial stress and porewater pressure were increased to the initial test conditions of 5.8 and 2.0 MPa respectively. Examination of the data, Figure 21, immediately shows during test stage [3] that bypass flow was occurring, as radial pressures in each array increased at the same rate as the injection and backpressure systems. To allow the sample to swell and hopefully eliminate sidewall flow, the sample was allowed to equilibrate until day 10.8 when a constant head test was undertaken, stage [5]. The test yielded a permeability value of  $6.70 \times 10^{-18} \text{ m}^2$  confirming bypass flow was occurring. To seal the clay against the vessel wall, the sample was allowed to equilibrate until day 33 when a second constant head test was performed. This yielded a modest reduction in permeability resulting in a value of  $3.97 \times 10^{-18} \text{ m}^2$ . A further period of equilibration ensued, stage [8], before a third constant head test, stage [9], was undertaken yielding a value of  $2.18 \times 10^{-18} \text{ m}^2$ .

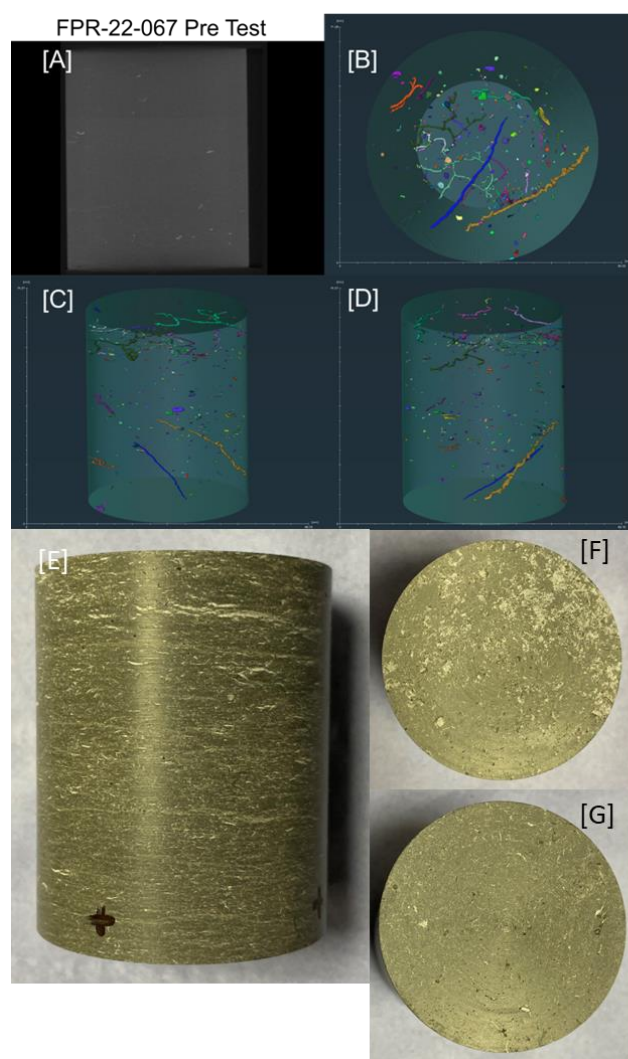


Figure 20 - Post-test imaging of sample FPR-22-067. [A] Orthogonal CT; [B] CT image of features XY orientation; [C] CT image of features XZ orientation; [D] CT image of features YZ orientation. [E], [F] and [G] pre-test optical images of sample showing side view (with injection end marked with a cross), backpressure face and injection face respectively.

Table 20 - Test FPR-22-067 showing the type of experimental stage and boundary conditions for the test. Note Ramp = an increase in stress and/or porewater pressure; EQ = equilibration stage; CHT = constant head test; TI = temperature increase and TD = temperature decrease.

Stage number	Type	Day	Injection pressure (MPa)	Backpressure (MPa)	Axial stress (MPa)	Average oven temperature (°C)
1	Ramp	0	0.0	0.0	0-3.9	28
2	EQ	0.1	0.0	0.0	3.9	28
3	Ramp	4.0	0.0-2.0	0.0-2.0	3.9-5.8	28
4	EQ	4.1	2.0	2.0	2.0	28
5	CHT	10.8	2.25	2.0	5.8	28
6	EQ	13.8	2.0	2.0	5.8	28
7	CHT	33.0	2.25	2.0	5.8	28
8	EQ	33.1	2.0	2.0	5.8	28
9	CHT	58.2	2.25	2.0	5.8	27
10	EQ	53.0	2.0	2.0	5.8	28

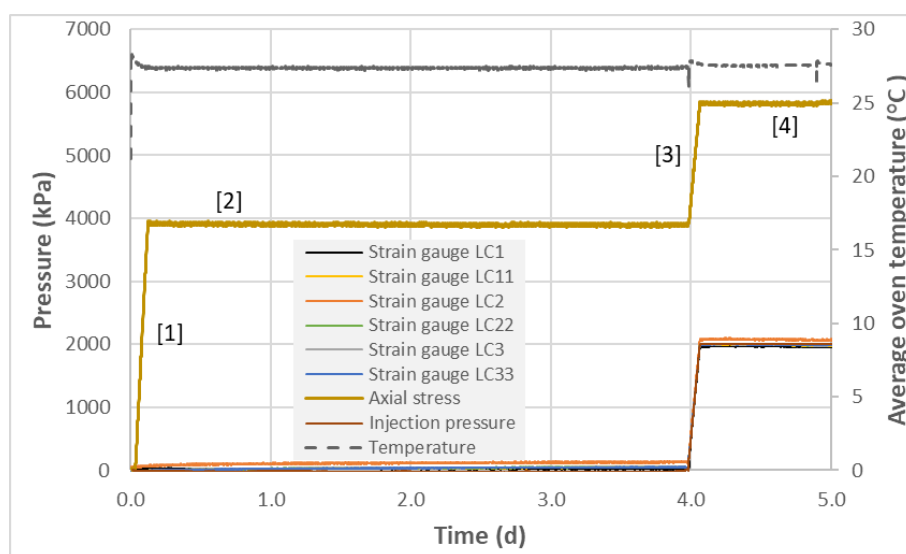


Figure 21 - FPR-22-067 showing the initial loading and hydration of the sample. The fact radial porewater pressures match that of the injection/backpressure systems indicates sideways flow.

In Figure 22, the permeability decreases as the OPA swells within the bore of the vessel. However, the relatively low clay content and indurated nature of the test material means that swelling in the presence of Pearson water is relatively slow. Figure 22 suggests it would take a protracted time to get anywhere close to in situ permeability in the low  $10^{-20} \text{ m}^2$ . It is worth noting that the difference in diameter between this, and a successful test such as FPR-21-052, is only around 0.05 mm. Obviously, ovality of the sample also impacts sealing, but as the values presented in Table 6 demonstrate, only minor differences in diameter can result in a compromised test.

This highlights an inherent weakness with the K0 geometry when used to test indurated material. Data suggests the tolerance between a ‘good’ and ‘bad’ sample is extremely small, and unless the material

is exposed to a fluid chemistry which promotes rapid swelling, obtaining an adequate seal may take a long time. Test FPR-22-067 was therefore terminated and the sample preserved in case it could be of use in the future.

Table 21 - Test FPR-22-067. Intrinsic permeability ( $k$ ) data from ambient and elevated temperature testing where  $k_{in}$  = permeability based on inflow,  $k_{out}$  = permeability based on outflow and  $k_{ave}$  = the average permeability based on inflow and outflow values.

Stage number	Average oven temperature (°C)	Intrinsic permeability, $k$ , (m <sup>2</sup> )		
		$k_{in}$ (m <sup>2</sup> )	$k_{out}$ (m <sup>2</sup> )	$k_{ave}$ (m <sup>2</sup> )
5	28	6.74x10 <sup>-18</sup>	6.66 x10 <sup>-18</sup>	6.70x10 <sup>-18</sup>
7	28	3.94x10 <sup>-18</sup>	3.99 x10 <sup>-18</sup>	3.97x10 <sup>-18</sup>
9	27	2.24x10 <sup>-18</sup>	2.13 x10 <sup>-18</sup>	2.18x10 <sup>-18</sup>

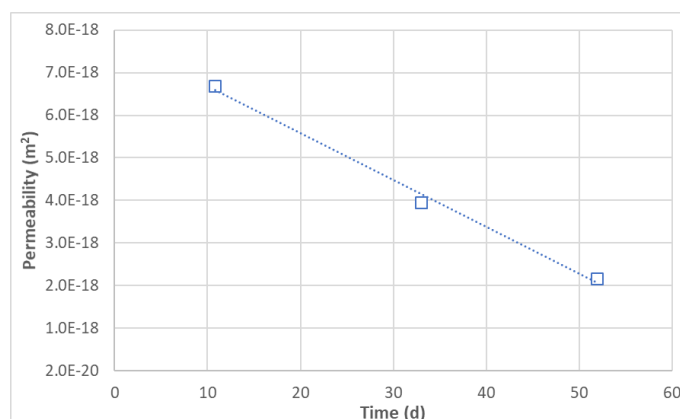


Figure 22 - FPR-22-067. Plot of permeability against test duration. Data shows that swelling on OPA (subject to Pearson water) under oedometric testing is very slow and bypass flow can continue for many days.

#### 4.3.10 Test FPR-22-098 (OPA taken from core barrel BF1-3 (4.3), perpendicular to bedding)

Test FPR-22-098 represented the last test to be undertaken as part of this study. Figure 23 shows optical and X-ray CT images of the sample prior to testing. The CT data suggests the sample has one of the lowest overall feature volumes (i.e., the volume of features >0.5 mm<sup>3</sup>). The pre-test dimensions of the sample, Table 6, also compare favorably with other successful tests where the sealing between the vessel wall and sample were achieved. However, it quickly became apparent that either bypass flow was occurring, or the sample was damaged in some way. Upon application of porewater pressure in stage [3], Table 22, and later the constant head test, stage [5], porewater pressures immediately responded to changes in the injection pressure. In contrast, the average pressure on the LC3 plane remained unaffected by changes in the injection pressure. It therefore seems likely that filter pressures on this plane were in direct communication with the backpressure pump. For these reasons peak radial pressures observed during heating to 81°C stage [7], 66°C stage [13] and 50°C stage [20], are not presented in this report.

Unlike previous tests, a differential transducer was added to the test system to allow accurate measurement of the difference in pressure, and therefore the head gradient driving water flow,

between the injection and backpressure pumps. This data was used to calculate permeability values. Data from the first constant head test, stage [5], yielded an average permeability value of  $9.92 \times 10^{-20}$  m<sup>2</sup>. While there were clear problems with the measurement of radial pressures, the sample still exhibited a low permeability value. On this basis it was decided to continue testing to quantify the relationship between temperature and permeability for this ‘damaged/compromised’ sample.

Constant head tests were performed before, during and after each thermal cycle, Table 22, with the results presented in Table 23. Inspection of the data indicates a similar trend in behavior to that of previous tests with permeability reducing as temperature increases. As with test FPR-22-025 there is some scatter around the values measured at low temperature stages, i.e., 27-28°C, which exhibit a general reduction in value as the duration of the test increases. It seems likely that this relates to swelling and closure of permeability pathways.

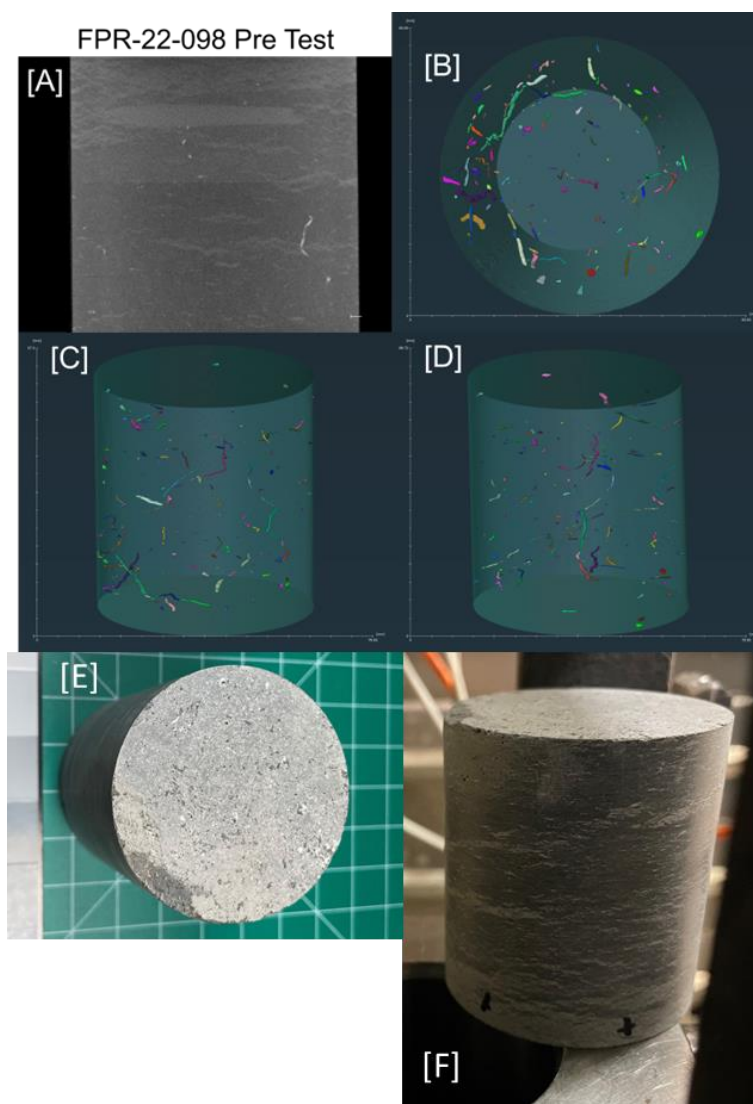


Figure 23 - Post-test imaging of sample FPR-22-098. [A] Orthogonal CT, with evidence of lens features; [B] CT image of features XY orientation; [C] CT image of features XZ orientation; [D] CT image of features YZ orientation; [E] photo of backpressure end of core showing chip missing from the sample; [F] side view of core (black crosses mark injection end) adjacent to the vessel bore.

Table 22 - Test FPR-22-098 showing the type of experimental stage and boundary conditions for the test. Note Ramp = an increase in stress and/or porewater pressure; EQ = equilibration stage; CHT = constant head test; TI = temperature increase and TD = temperature decrease. Test remains on-going.

Stage number	Type	Day	Injection pressure (MPa)	Backpressure (MPa)	Axial stress (MPa)	Average oven temperature (°C)
1	Ramp	0	0.0	0.0	0.0-3.9	27
2	EQ	0.2	0.0	0.0	3.9	27
3	Ramp	4.1	0-2.0	0-2.0	3.9-5.9	27
4	EQ	4.2	2.0	2.0	5.9	27
5	CHT	20.9	2.26	2.0	6.0	27
6	EQ	24.7	2.0	2.0	6.0	28
7	TI	26.0	2.0	2.0	6.1	81
8	CHT	30.9	2.3	2.0	6.0	83
9	EQ	38.0	2.0	2.0	6.1	84
10	TD	40.7	2.1	2.0	6.0	28
11	CHT	44.8	2.26	2.0	6.1	28
12	EQ	48.9	2.0	2.0	6.1	28
13	TI	52.8	2.0	2.0	6.0	66
14	EQ	53.0	2.0	2.0	6.1	67
15	CHT	55.9	2.26	2.0	6.1	67
16	EQ	62.8	2.0	2.0	6.1	67
17	TD	66.0	2.0	2.0	6.1	28
18	CHT	88.7	2.26	2.0	6.1	28
19	EQ	93.7	2.0	2.0	6.1	28
20	TI	96.9	2.0	2.0	6.0	50
21	EQ	97.0	2.0	2.0	6.0	51
22	CHT	104.0	2.26	2.0	6.1	51
23	EQ	110.0	2.0	2.0	6.1	51
24	TD	111.8	2.0	2.0	6.1	28
25	CHT	117.7	2.26	2.0	6.1	28
26	EQ	121.6	2.0	2.0	6.1	28
27	CHT	125.8	2.26	2.0	6.1	28
28	EQ	130.7	2.0	2.0	6.1	28

Table 23 - Test FPR-22-067. Intrinsic permeability ( $k$ ) data from ambient and elevated temperature testing where  $k_{in}$  = permeability based on inflow,  $k_{out}$  = permeability based on outflow and  $k_{ave}$  = the average permeability based on inflow and outflow values.

Test stage	Average oven temperature (°C)	Intrinsic permeability, $k$ , (m <sup>2</sup> )		
		$k_{in}$ (m <sup>2</sup> )	$k_{out}$ (m <sup>2</sup> )	$k_{ave}$ (m <sup>2</sup> )
5	27	1.13x10 <sup>-19</sup>	8.50x10 <sup>-20</sup>	9.92x10 <sup>-20</sup>
8	83	1.71x10 <sup>-20</sup>	2.12x10 <sup>-20</sup>	1.92x10 <sup>-20</sup>
11	28	8.80x10 <sup>-20</sup>	8.96x10 <sup>-20</sup>	8.88x10 <sup>-20</sup>
15	67	2.33x10 <sup>-20</sup>	2.52x10 <sup>-20</sup>	2.43x10 <sup>-20</sup>
18	28	-	7.09x10 <sup>-20</sup>	7.09x10 <sup>-20</sup>
22	51	5.32x10 <sup>-20</sup>	4.17x10 <sup>-20</sup>	4.17x10 <sup>-20</sup>
25	28	1.39x10 <sup>-19</sup>	8.00x10 <sup>-20</sup>	8.00x10 <sup>-20</sup>
27	28	1.08x10 <sup>-19</sup>	8.30x10 <sup>-20</sup>	8.30x10 <sup>-20</sup>

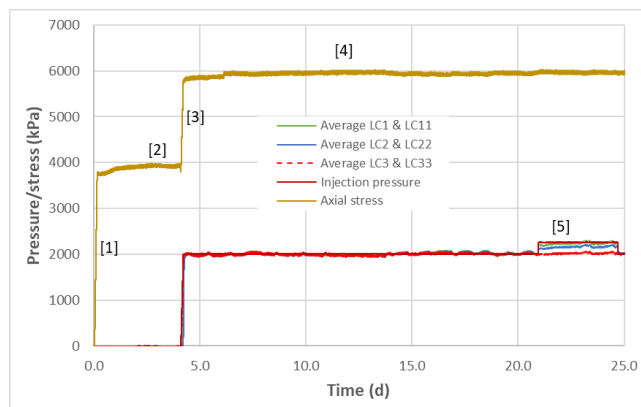


Figure 24 - FPR-22-098 showing the initial loading of the sample, stages [1] and [3], hydration, stage [4], and constant head testing, stage [5]. The fact radial porewater pressures match that of the injection/backpressure systems indicates sideways flow. Also apparent is that the radial sensors, even after an offset was applied to each device, begin to drift as the test progresses.

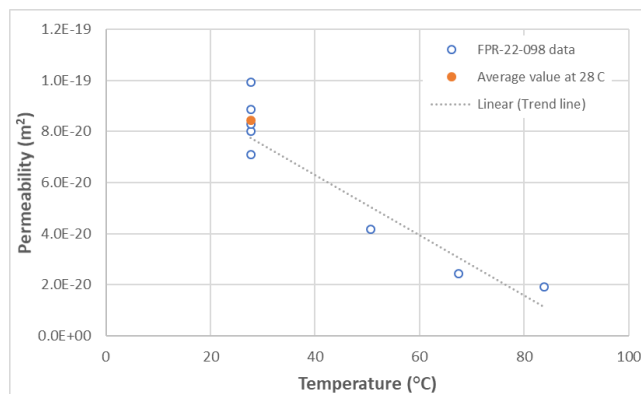


Figure 25 - FPR-22-098. Plot of permeability against temperature. As with previous tests, sample FPR-22-098 exhibits a general trend of decreasing permeability with increasing temperature.

## 4.4 Conclusion

### 4.4.1 New knowledge acquired

Six successful and two partially successful tests have been completed as part of this study examining the development of over pressure caused by the thermal expansion of porewater, and its subsequent impact on the evolution of intrinsic permeability. Results demonstrate that in all cases the permeability of COx and OPA was observed to decrease on heating, with the rate of change linked to the initial permeability of the sample. In OPA, heating of material to around 70°C resulted in the development of local porewater pressures exceeding the axial stress, Figure 11 and Figure 14, with peak pressure increasing with temperature. While porewater pressures exhibited some degree of local anisotropy, and when averaged across each measurement plane, they rarely exhibited hydraulic symmetry, indicating some heterogeneity on the length-scale of the tests.

The permeability of COx was shown to be considerably lower than that of OPA, Figure 26. Commensurately, peak porewater pressures were also much higher than those in the OPA for similar degrees of heating, with possible evidence of localised mechanical failure at high porewater overpressures.

In tests FPR-21-052 and FPR-22-025 the relationship between peak porewater pressure and confining stress was explored for samples prepared both parallel and perpendicular to bedding. While testing the samples at a higher axial stress resulted in an increase in the magnitude of the peak porewater pressures, values remained well below the axial stress, for samples both parallel and perpendicular to bedding. This can be explained by the indurated and over consolidated nature of the OPA, where permeability change is relatively minor as the clay moves along its rebound-reconsolidation line (Horseman et al., 2005). This was also shown by the data in Figure 13, which exhibited only a minor drop in permeability for approximately a 3-fold increase in axial effective stress.

It is worth noting that at temperatures of 70°C and upwards, the difference in the peak porewater pressure values as a function of applied axial stress, becomes more pronounced and continues to increase as temperature rises. When viewed from a repository context, the data indicates the development of thermally induced porewater pressures will increase with depth. Hence, constructing a repository at a depth where peak thermally induced porewater pressures remain below in situ stress, would ensure host rock integrity. The fact that thermally induced porewater pressures consistently remain below the total stress in the samples where axial loads are higher, indicates it would be possible, knowing the heat output of the waste, to calculate a repository depth below which thermally induced porewater pressures could be managed and would always remain lower than the in-situ stress.

In all tests, the pulse in porewater pressures caused by heating of the sample was short-lived (<24 h), reflecting the stiffness of the materials and the small amounts of water moved due to thermal expansion/contraction. When heat was removed and each sample returned to ambient conditions and the permeability re-tested, no obvious signs of hydraulic damage were observed in any test samples. This is an important message from a safety assessment point of view.

Clearly, under true in-situ conditions, the rapid generation of porewater pressure from thermal expansion of porewater would be capped by the sum of the total stress and tensile strength of the host rock. As the tensile strength of most mudrocks is relatively low, these experiments suggest thermally induced fracturing of the host rock would be possible if subject to sufficient heat and rapid loading. The fact that there was no sign of hydraulic damage when permeability was remeasured, could reflect the boundary conditions of the test, i.e., the same radial constraint which prevents sample swelling during heating, can also prevent mode 1 or mode 2 fracturing from occurring. Follow-up work should be performed under triaxial or isotropic boundary conditions to confirm these results before their use in repository safety assessment.

The role of bedding anisotropy was explored in tests FPR-21-051 and 21-052 (both parallel to bedding) and test FPR-22-025 (undertaken perpendicular to bedding), Figure 26. Examination of the data leads to an average ratio of permeability to parallel bedding against permeability perpendicular to bedding of around 2.9 for the range of temperatures tested. This indicates hydraulic anisotropy is present.

The data in Figure 26 shows COx has a significantly lower permeability than OPA and exhibits only a minor sensitivity to increases in temperature. In contrast, data from tests performed on OPA all show a higher degree of sensitivity of permeability to changes in temperature, especially the ‘damaged’ samples highlighted by the green triangles.

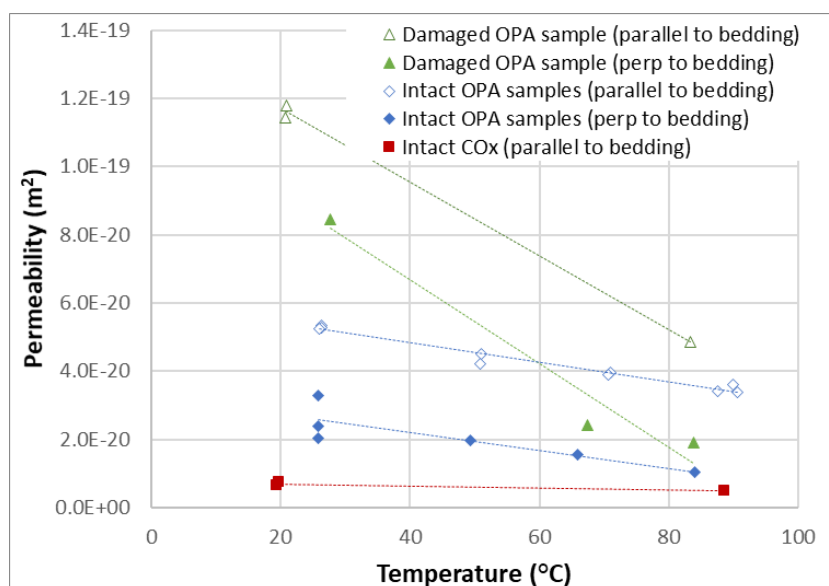


Figure 26 - Summary of permeability against temperature data for tests undertaken in this study.

The permeability of sample FPR-21-051 is fractionally lower than that of FPR-21-052 which may contribute to the higher porewater pressures observed on heating, Figure 11 and Figure 14. While data is limited, a cross-plot of values taken from tests FPR-21-027, FPR-21-051, FPR-21-052 and FPR-22-025 tests when temperature was initially increased to 90°C, Figure 27, appears to confirm this hypothesis. In this figure, permeability is plotted against the peak porewater pressure observed, which is always across the mid-plane of the sample. As samples were approximately the same dimension, drainage times due to changes in sample length are assumed equal. Data suggests a trend in behaviour where peak porewater pressures are linked to the permeability of the sample, rather than just the axial stress, a finding borne out by the data presented in Figure 15.

However, it should be noted that the zero-strain radial constraint imposed by the pressure vessel (but necessary to facilitate pressure measurement), prevented radial expansion of the sample. This conservative boundary condition, along with the rapid heating of the clay, means that the porewater pressures observed can be considered as an almost ‘worse-case scenario’. Clearly, as more data becomes available the relationships identified in this study may change, but currently this study provides new insight into the factors affecting the development of overpressure in indurated clays near heat emitting waste.

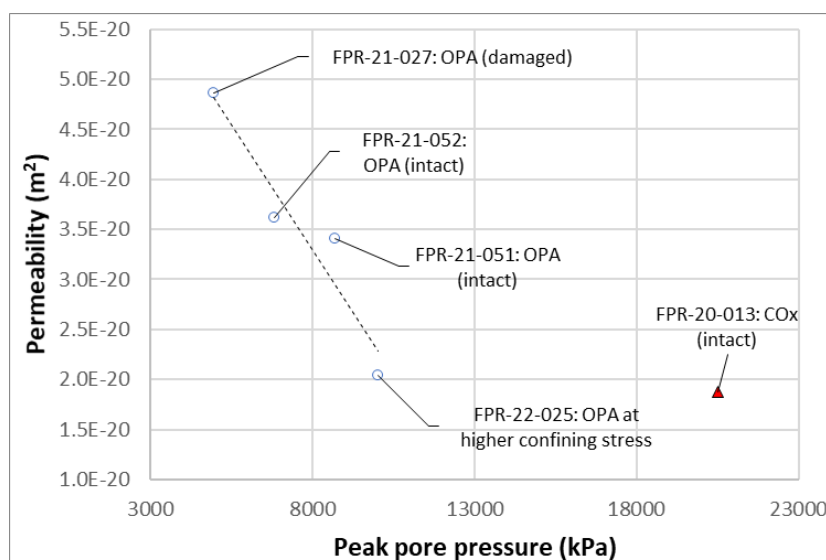


Figure 27 - Cross-plot of values taken from all four tests when temperature was initially increased to 90°C. While limited data is available, a crude trend between peak porewater pressure and permeability emerges.

#### 4.4.2 Impact of acquired knowledge

This study has identified important hydro-mechanical couplings between the development of porewater over pressure and the exposure of COx and OPA to heat. The most important of which is that thermally induced porewater pressures can exceed total stress. Evidence for localised failure of the rock was noted in the COx experiment, probably linked to its lower permeability. In all experiments no evidence for the degradation of hydraulic properties was observed once temperatures had dissipated. Correlations between permeability and peak porewater pressure have been highlighted, along with correlations between permeability and temperature as well as confining stress and the magnitude of porewater pressures generated during rapid heating. Data from this study indicates that, with a knowledge of the heat emissions of the waste, it would be possible to manage the development of thermally induced porewater over pressures by selecting a suitable repository depth.

#### 4.4.3 Remaining knowledge gaps

This study has identified potential correlations between the development of porewater overpressures generated during rapid and their coupling to permeability and confining stress. However, there are relatively few data points which means all such relationships are indicative. Moreover, the impact of boundary conditions should be explored as the radial constraint imposed by the K<sub>0</sub> geometry used in this study, may limit some failure mechanisms, such as mode 1 and 2 fracture development. This may impact both the form and nature of the correlations proposed. In addition, the mechanisms driving the reduction in permeability when heated needs further consideration.

#### 4.4.4 Recommendations for the future

This report has highlighted a number of important hydro-mechanical couplings which require additional data, to add confidence and reduce uncertainty, before they can be applied in safety assessment. These include the role of the boundary stress and any volumetric constraints, delineating the link between permeability and overpressure and understanding the coupling between burial history, the magnitude of heat induced overpressure and their coupling to temperature.

While there are considerable benefits, this study has also highlighted inherent weaknesses with the  $K_0$  geometry when used to test indurated material. Sample ovality and sealing against the vessel walls is a real issue, as swelling is slow when samples are exposed to synthetic porewater (data shows it can take a long time to close even small voids/gaps). Closure is further hampered by the low permeability of these materials, which limit water inflow rates further, retarding swelling potential. Caution should therefore be employed when interpreting  $K_0$  data. Future measurements should be accompanied by complimentary isotropic and/or triaxial testing. While the latter will struggle to measure thermally induced overpressures, they would be able to track permeability as a function of temperature and stress. Future studies should include additional  $K_0$  and supportive/complementary isotropic/triaxial measurements.

## 4.5 Appendix

### 4.5.1 Drainage system's influence on the thermally induced pressure response

The influence of the drainage system on the measurement of the thermally induced pressure response is examined here, as similarly done in Ghabezloo and Sulem, 2010).

In a perfect undrained THM test carried out in an elastic porous material, the pore pressure increase is given by

$$\Delta u = B\Delta\sigma + \Lambda\Delta T \quad (1)$$

where  $\Delta\sigma$  and  $\Delta T$  are the changes in isotropic stress and temperature, respectively. The Skempton coefficient  $B$  and the thermal pressurization coefficient  $\Lambda$  can be defined as

$$B = \frac{c_d - c_s}{(c_d - c_s) + \phi(c_f - c_\phi)} \quad (2)$$

$$\Lambda = \frac{\phi(\alpha_f - \alpha_\phi)}{(c_d - c_s) + \phi(c_f - c_\phi)} \quad (3)$$

where  $\phi$  is the sample's porosity,  $\alpha_f$  is the thermal expansion coefficient of the pore-fluid,  $\alpha_\phi$  is the thermal expansion coefficient of the porous medium,  $c_d$  is the drained compressibility of the saturated rock,  $c_f$  is the compressibility of the liquid phase,  $c_s$  is the compressibility of the solid phase and  $c_\phi$  is the compressibility of the porous medium.

When the effects of the drainage system are taken into account, Eq. (1) leads to

$$\Delta u = B_{mes}\Delta\sigma + \Lambda_{mes}\Delta T \quad (4)$$

with

$$B_{mes} = \frac{(c_d - c_s) + \frac{V_L \rho_{fL}}{V \rho_f} \kappa_L}{(c_d - c_s) + \phi(c_f - c_\phi) + \frac{V_L \rho_{fL}}{V \rho_f} (c_{fL} + c_L)} \quad (5)$$

$$\Lambda_{mes} = \frac{\phi(\alpha_f - \alpha_\phi) + \beta \frac{V_L \rho_{fL}}{V \rho_f} (\alpha_{fL} - \alpha_L)}{(c_d - c_s) + \phi(c_f - c_\phi) + \frac{V_L \rho_{fL}}{V \rho_f} (c_{fL} + c_L)} \quad (6)$$

in which  $V$  is the sample volume,  $V_L$  is the volume of the drainage system,  $\rho_f$  is the pore-fluid density,  $\rho_{fL}$  is the density of the water in the drainage system,  $\kappa_L$  is an isothermal compressibility,  $\beta$  is the temperature ratio (between the drainage system and the sample),  $\alpha_{fL}$  is the thermal expansion coefficient for the water in the drainage system,  $\alpha_L$  is the thermal expansion coefficient of the drainage system,  $c_{fL}$  is the compressibility of the water in the drainage system and  $c_L$  is the compressibility of the drainage system.

In other words, the measured Skempton and thermal pressurization coefficients have to be corrected as

$$B_{cor} = \frac{B_{mes}}{1 + \frac{V_L \rho_{fL}}{V \rho_f (c_d - c_s)} [k_L - B_{mes} (c_{fL} + c_L)]} \quad (7)$$

$$\Lambda_{cor} = \frac{\Lambda_{mes}}{1 + \frac{V_L \rho_{fL}}{V \rho_f \phi (\alpha_f - \alpha_\phi)} [\beta (\alpha_{fL} - \alpha_L) - \Lambda_{mes} (c_{fL} + c_L)]} \quad (8)$$

The experimental evaluation of these parameters is a difficult task since the thermal effects need to be taken into account and thus, the following assumptions/parameters are made:

- **Assumption 1 (needed to derive  $\Lambda_{mes}$  from experimental data):** from day 19.15 to 19.45, the effect of stress change is neglected compared with thermal effects (increase in temperature of 70°C in 0.30 days, i.e., 7.2 hours, see Figure 28). Thus, in such a case, Eq. (4) leads to a linear relationship between  $\Delta u$  and  $\Delta T$  and the slope of the measured pore pressure curve versus the temperature gives the measured thermal pressurization coefficient  $\Lambda_{mes}$ . Figure 29 shows the pressure evolution as a function of temperature. As seen, sensor LC1 is not representative of the theoretical behaviour and hence, it will not be employed for the forthcoming analysis. The rest of sensors show a (i) linear relationship between temperature and pressure until  $T=70^\circ\text{C}$ , followed by a (ii) pressure decreasing (see section 8.1.2 for a detailed analysis of this behaviour change). In these sensors and applying standard procedures, the measured thermal pressurisation coefficients of Table 24 are obtained.
- **Assumption 2 (needed to analytically derive  $\Lambda_{cor}$  from  $\Lambda_{mes}$ ):** corrected thermal pressurisation coefficients are computed by assuming the following parameters
  - o  $V_L = 2.42 \times 10^{-7} \text{ m}^3$ . Contributions of the filter ( $1.51 \times 10^{-7} \text{ m}^3$ ) the pipe ( $1.24 \times 10^{-8} \text{ m}^3$ ) and the transducer ( $7.85 \times 10^{-8} \text{ m}^3$ ) are considered.
  - o  $V = 1.17 \times 10^{-4} \text{ m}^3$ .
  - o  $\rho_f = \rho_{fL} = 988.25 \text{ kg/m}^3$ . Density of water (both for the sample and the drainage system) is considered to be a function of temperature. Thus, the average value between the density at 20°C and 90°C is assumed. Same densities for the sample and the drainage system are considered.
  - o  $\phi = 0.145$  (measured).
  - o  $\alpha_f = \alpha_{fL} = 4.37 \times 10^{-4} \text{ }^\circ\text{C}^{-1}$ . As done with the water density, the thermal expansion coefficient of water is considered to be a function of temperature. Thus, the average value between the density at 20°C and 90°C is assumed. The sample and the drainage system are considered to have the same temperature and hence, same thermal expansion coefficients are assumed.
  - o  $\alpha_\phi = \alpha_L = 1.4 \times 10^{-5} \text{ }^\circ\text{C}^{-1}$ , see [6]
  - o  $\beta = 1$ , since the sample and the drainage system are considered to be at the same temperature.
  - o  $c_{fL} = c_L = 4.7 \times 10^{-10} \text{ Pa}^{-1}$ , approximated value taken from [7].

These assumptions allow the computation of corrected maximum pore pressures, see Table 25. As seen, the thermal compliance from the measurement system to the maximum pore pressure value is minor in each sensor (<2%).

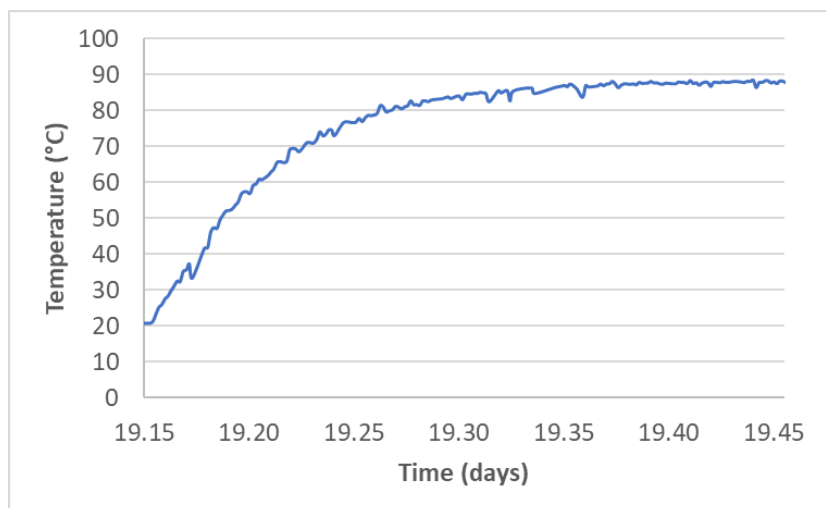


Figure 28 - Cross-plot of values taken from all four tests when temperature was initially increased to 90°C. While limited data is available, a crude trend between peak porewater pressure and permeability emerges.

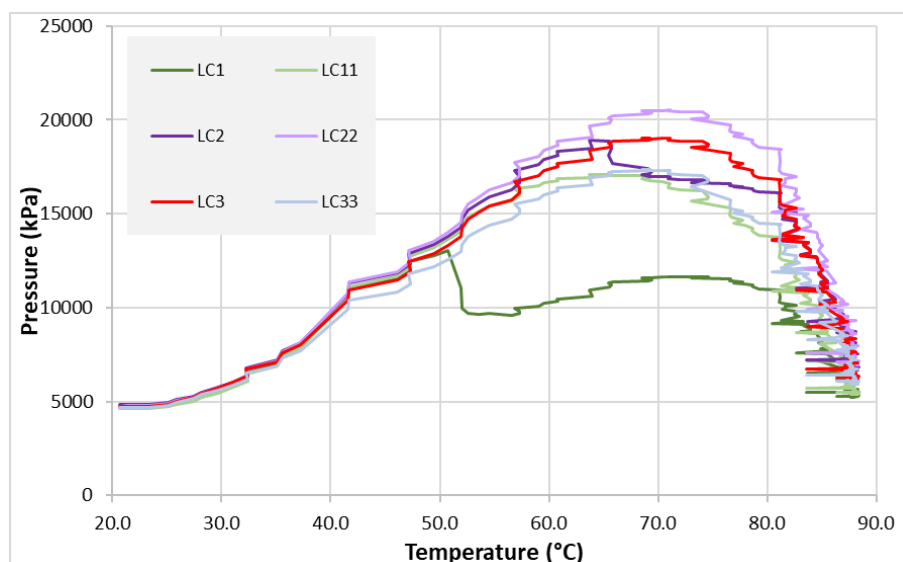


Figure 29 - Pressure evolution as a function of temperature in each sensor (corresponding to day 19.15 to 19.45).

Table 24 - Measured thermal pressurisation coefficients.

	Sensor	$\Lambda_{mes}$
First plane	LC1	-
	LC11	348.19
Second plane	LC2	357.20
	LC22	374.24
Third plane	LC3	343.17
	LC33	296.16

Table 25 - Corrected thermal pressurisation values and their effect on maximum pressured observed in each sensor.

	Sensor	$\Lambda_{mes}$	$\Lambda_{cor}$	Temp. at which maximum P is observed (°C)	Maximum measured P (kPa)	Maximum corrected P (kPa)	%
First plane	LC1	-	-	-	-	-	-
	LC11	324.68	320.13	65.51	17103.18	16821.30	98.35
Second plane	LC2	357.20	352.20	63.70	18909.11	18587.84	98.30
	LC22	374.24	369.00	71.13	20523.22	20176.58	98.31
Third plane	LC3	343.17	338.37	70.43	19008.52	18693.78	98.34
	LC33	296.16	292.01	69.27	17354.84	17079.27	98.41

In order to understand the impact of the assumed values of the before-mentioned parameters on the maximum measured pressures, a sensitivity analysis of the main parameters has been performed. The following parameters have been analysed:

- Volume of the drainage system ( $V_L$ ): values ranging from  $1.4 \times 10^{-7} \text{ m}^3$  to  $3.5 \times 10^{-7} \text{ m}^3$  have been considered.
- Density of water both for the sample and the drainage system ( $\rho_f, \rho_{fL}$ ): values ranging from  $1007.35 \text{ kg/m}^3$  to  $969.15 \text{ kg/m}^3$  (corresponding to  $T=20 \text{ °C}$  and  $T=90 \text{ °C}$  respectively) have been considered. Note that as long as the assumption  $\rho_f = \rho_{fL}$  is valid, no effect on corrected pressures was found, see Eq. (9).
- Thermal expansion coefficient of water for both the sample and the drainage system ( $\alpha_f, \alpha_{fL}$ ): values ranging from  $2.07 \times 10^{-4} \text{ °C}^{-1}$  to  $6.66 \times 10^{-4} \text{ °C}^{-1}$  (corresponding to  $T=20 \text{ °C}$  and  $T=90 \text{ °C}$  respectively) have been considered.
- Compressibility of water in the drainage system and compressibility of the drainage system ( $c_{fL}, c_L$ ): values ranging from  $4.1 \times 10^{-10} \text{ Pa}^{-1}$  to  $4.9 \times 10^{-10} \text{ Pa}^{-1}$  ([7]) have been considered.

As seen in Figure 30, the variability range of almost all the parameters is small and thus, their effect when correcting the maximum measured pressure is negligible. Only the volume of the drainage system might vary significantly and hence, its effect on the maximum corrected pressure.

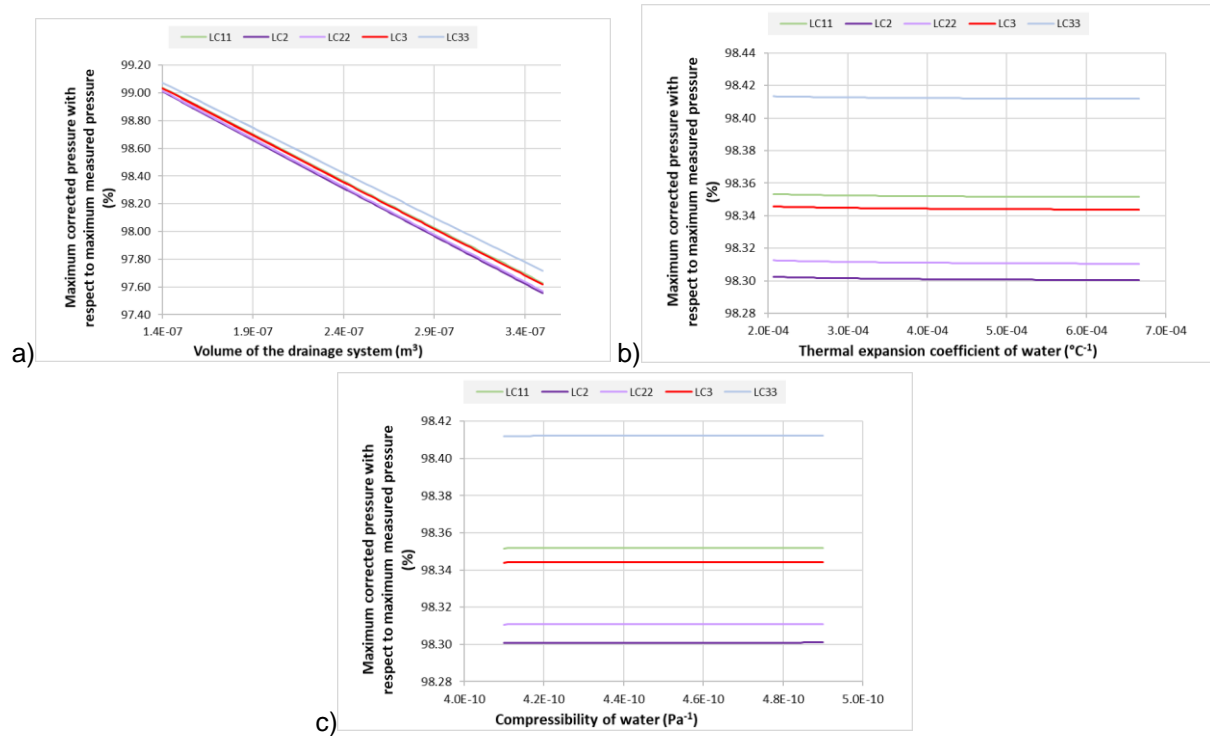


Figure 30 - Sensitivity analysis of the change (in %) of the maximum corrected pressure with respect to the maximum measured pressure when varying [a] the volume of the drainage system, [b] the thermal expansion coefficient of water for both the sample and the drainage system and [c] the compressibility of water in the drainage system and the compressibility of the drainage system.

#### 4.5.2 Drainage system’s influence on the thermally induced pressure response

The assumed linear relationship between  $\Delta u$  and  $\Delta T$  is only valid up to a point, see Figure 29 and Table 26. In order to understand this change in behaviour, (i) the net change in length due to temperature gradient (i.e. the difference between the change in sample length and the change at the top of the vessel) and (ii) the corresponding longitudinal strain (i.e. the ratio between this net change in length and the original length) are computed, see Figure 31 and Figure 32.

Table 26 - Time (in days) and temperature (in °C) at which the linear relationship between  $\Delta u$  and  $\Delta T$  is no longer valid.

	Sensor	Temperature (in °C)	Time (days)
First plane	LC1		-
	LC11	65.51	19.22
Second plane	LC2	63.70	19.21
	LC22	71.13	19.21
Third plane	LC3	70.43	19.22
	LC33	69.27	19.22
Average		68.01	19.22

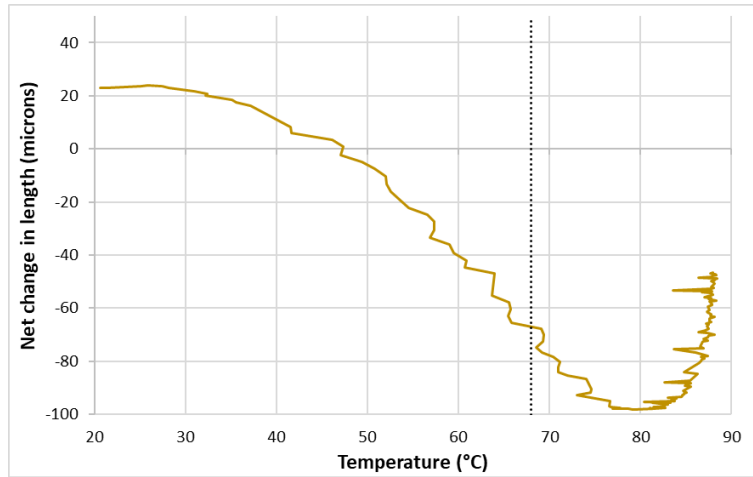


Figure 31 - Net change in length as a function of temperature for days 19.15 to 19.45. Black-dotted line represents the temperature at which peak pressures are observed (in average).

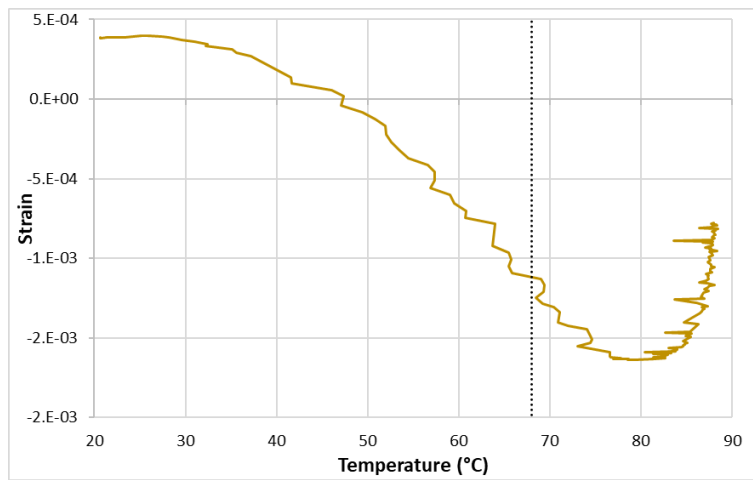


Figure 32 - Axial strain as a function of temperature.

## 5. General conclusions

The present report - D7.5 - Technical report on effect of temperature on far field properties - is the final deliverable for subtask 2.2. Laboratory experiments were performed on candidate clay host rocks to provide answers about the effects of increased temperature on the short and long-term mechanical behaviours (deformations, elastic properties, failure strength) and on the evolution of damage and intrinsic permeability due to porewater overpressures. Different testing cells (triaxial, oedometric) have been used by the different partners to achieve these goals. The tested clay host rocks were: Callovo Oxfordian claystone (COx), Opalinus clay (OPA) and Boom clay.

During the initial heating before the short-term compression tests on the COx, transitory pore water overpressure (due to thermal expansion) was shown to induce microcracks parallel to the bedding planes. Temperature has globally a negative impact on the peak strength of the COx claystone until 100 °C for both parallel and perpendicular sample orientations due to this initial thermo-hydro-mechanical damage. The decrease in the peak strength with temperature is the most significant for the parallel to bedding samples under uniaxial test conditions, because confining pressure (4 and 12 MPa) reduced the initial thermo-induced microcracks. These microcracks were also closed when the axial stress was increased during the compression tests performed perpendicular to bedding. There was no noticeable impact of temperature up to 100 °C on the evolutions of the elastic coefficients. For all orientations and confining pressures, there is a significant increase in the peak strength for the highest temperature (150 °C), which can be explained by pore water vaporization and the development of a very significant capillary suction.

Long-term behaviour of the three candidate clay host rocks has been studied with multi-step triaxial creep tests. The tests on Boom clay and Opalinus clay were performed under saturated conditions. As temperature was increased, the measured strain also increased which then stabilized when the temperature was higher. At this point of the study, it is not possible to establish a link between the temperature level and the deviator that causes the failure of the sample. A better investigation of the effects of the temperature on the creep behaviour of the Boom clay and Opalinus clay requires more data and longer duration creep tests. Concerning the COx claystone, tests were performed under unsaturated condition (saturation degree = 90-95%). So far, only multi-step creep tests at  $T = 20$  °C and  $P_c = 2$  and 12 MPa, and at  $T = 80$  °C and  $P_c = 12$  MPa, for both parallel and perpendicular samples, were performed on the COx claystone (the remaining multi-step creep tests are in progress). These first results showed that creep deformations are larger at higher temperature (80 °C) and that long-term strength seems to decrease with temperature. This conclusion has obviously to be confirmed when all the creep tests at different temperatures will be finished.

The development of over pressure caused by the thermal expansion of porewater, and its subsequent impact on the evolution of intrinsic permeability, was analysed on both COx and OPA. In all cases the permeability was observed to decrease on heating. Heating samples above circa 70 °C resulted in the development of local porewater pressures which exceeded the axial stress. The size of this overpressure was related to the initial permeability of the sample. In the COx sample tested this may have resulted in the development of thermally induced microcracking. However, in all experiments, including that performed on COx, no evidence for the degradation of hydraulic properties was observed once temperatures had dissipated.

In-situ, there is a competition between the excess pore pressure due to the thermal loading induced by the radioactive waste and the drainage due to the increase in pore pressure gradient. With its lower permeability, it seems likely that in a repository context thermally induced overpressure between disposal cells will occur under quasi-undrained conditions. In this scenario, a knowledge of the impact of temperature and induced pore water overpressure on the mechanical properties of the COx claystone is important. According to the experimental results obtained in laboratory tests within the subtask 2.2, temperature has a likely negative impact on the short-term resistance to failure of the COx claystone. But if this thermo-hydro-mechanical damage is induced, it would probably be limited to the very near field of the excavation damaged zone, where the confining pressure is the lowest.

## Acknowledgements

The experiments presented by CNRS(ULorraine) were carried out with the experimental devices available in the HGM experimental platform (Université de Lorraine-CNRS – <http://georessources.univ-lorraine.fr/fr/content/hydrogeomecanique>).

The authors of UKRI-BGS would like to thank Humphrey Wallis, Wayne Leman and the members of the BGS Research and Development workshops for design and manufacture of the apparatus. The authors would also like to thank the Core Scanning Facility (CSF) at the British Geological Survey (BGS) for providing access to the CT core scanner and their technical support and expertise, Mr Cameron Fletcher for undertaking analysis of the CT data and Mr Andrew Wiseall for his help in sample preparation and support in the laboratory.

## References

- Abou-Chakra Guéry, A., Cormery, F., Shao, J.-F. & Kondo, D., 2008. A Micromechanical Model of Elastoplastic and Damage Behavior of a Cohesive Geomaterial. *International Journal of Solids and Structures*, 45 (5): 1406-29.
- Agboli, M., Grgic, D., Moumni, M. & Giraud, A., 2023. Study under X-ray tomography of the impact of self-sealing process on the permeability of the Callovo-Oxfordian claystone. *Rock Mechanics and Rock Engineering*, doi: 10.1007/s00603-023-03350-y.
- Armand, G., Bumbieler, F., Conil, N., de la Vaissière, R., Bosgiraud, J.-M. & Vu, M.-N., 2017a. Main outcomes from in situ thermo-hydro-mechanical experiments programme to demonstrate feasibility of radioactive high-level waste disposal in the Callovo-Oxfordian claystone. *Journal of Rock Mechanics and Geotechnical Engineering*, 9(3): 415-427.
- Armand, G., Conil, N., Talandier, J., Seyedi, D.M., 2017b. Fundamental aspects of the hydromechanical behaviour of Callovo-Oxfordian claystone: From experimental studies to model calibration and validation. *Comput Geotech*, 85:277-286.
- Auvray, C., Arnold, G. & Armand, G., 2015. Experimental Study of Elastic Properties of Different Constituents of Partially Saturated Argillite Using Nano-Indentation Tests. *Engineering Geology*, 191: 61-70.
- Bauer-Plaindoux, C., Tessier, D. & Ghoreychi, M., 1998. Propriétés mécaniques des roches argileuses carbonatées : Importance de la relation calcite-argile. *Comptes Rendus de l'Académie des Sciences - Series IIA - Earth and Planetary Science*, 326 (4) : 231-37.
- Belmokhtar, M., Delage, P., Ghabezloo, S., Tang, A.-M., Menaceur, H. & Conil, N., 2016. Poroelasticity of the Callovo–Oxfordian Claystone. *Rock Mechanics and Rock Engineering*, 50: 871–889.
- Bemer, E., Longuemare, P. & Vincké, O., 2004. Poroelastic Parameters of Meuse/Haute Marne Argillites: Effect of Loading and Saturation States. *Applied Clay Science*, 26 (1): 359-66.
- Beucher, S. and Meyer, F., 2018. The morphological approach to segmentation: the watershed transformation. In *Mathematical morphology in image processing* (pp. 433-481). CRC Press.
- Blaise, T., Barbarand, J., Kars, M., Ploquin, F., Aubourg, C., Brigaud, B., Cathelineau, M., El Albani, A., Gautheron, C., Izart, A., Janots, D., Michels, R., Pagel, M., Pozzi, J.-P., Boiron, M.-C., Landrein, P., 2014. Reconstruction of low temperature (< 100 °C) burial in sedimentary basins: A comparison of geothermometer in the intracontinental Paris Basin. *Marine and Petroleum Geology*, 53: 71-87.
- Cheng, A.H.D., 2016. *Poroelasticity*, Springer.
- Chiarelli, A.S., Shao, J. & Hoteit, N., 2003. Modeling of Elastoplastic Damage Behavior of a Claystone. *International Journal of Plasticity*, 19 (1): 23-45.

Conil, N., Talandier, J, Djizanne, H., de La Vaissière, R., Righini-Waz, C., Auvray, C., Morlot, C. and Armand, G., 2018. How rock samples can be representative of in situ condition: A case study of Callovo-Oxfordian claystones. *Journal of Rock Mechanics and Geotechnical Engineering*, 10: 613-623.

Coussy, O., 2004. *Poromechanics*, John Wiley and Sons.

Davy, C.A., Skoczylas, F., Barnichon, J.-D. & Lebon, P., 2007. Permeability of Macro-Cracked Argillite under Confinement: Gas and Water Testing. *Physics and Chemistry of the Earth, Parts A/B/C, Clay in natural and engineered barriers for radioactive waste confinement - Part 2*, 32 (8): 667-80.

Escoffier, S., 2002. *Caractérisation expérimentale du comportement hydromécanique des argilites de Meuse/Haute-Marne*. PhD Thesis, INPL, Nancy (France).

Escoffier, S., Homand, F., Giraud, A., Hoteit, N. & Su, K., 2005. Under stress permeability determination of the Meuse/Haute-Marne argillite. *Eng. Geol.*, 81(3):329–340.

Esteban, L., 2006. *Anisotropies magnétique et de porosité des argilites du Callovo-Oxfordien du laboratoire souterrain de l'Andra (Meuse/Haute-Marne, Bassin de Paris)* », Phd Thesis, Toulouse (France).

Feldkamp, L.A., Davis, L.C., and Kress, J.W., 1984. Practical cone-beam algorithm. *Josa a*, 1(6), pp.612-619.

Gasc-Barbier, M., 2002. *Étude des mécanismes de déformation de roches argileuses profondes : apport de la microstructure et des analyses pétrophysiques*. Phd Thesis, Paris (France).

Geotek, 2023. RXCT: ROTATING X-RAY CT SYSTEM. Available at: <https://www.geotek.co.uk/x-ray-ct-system/geotek-rxct/> (accessed 12 September 2023).

Ghabezloo, S and Sulem, J. 2009. Stress dependent thermal pressurization of a fluid-saturated rock. *Rock Mechanics and Rock Engineering*, 42, 1-24. DOI: 10.1007/s00603-008-0165-z

Ghabezloo, S., and Sulem, J. 2010. Effect of the volume of the drainage system on the measurement of undrained thermo-poro-elastic parameters. *International Journal of Rock Mechanics and Mining Sciences*, 47, 60-68. DOI: 10.1016/j.ijrmms.2009.03.001.

Giot, R., Auvray, C. & Talandier, J., 2019. Self-sealing of claystone under X-ray nanotomography. *Geol Soc London Special Publ*, 482(1):213–223.

Grgic, D., Giot, R., Homand, F. & Giraud, A., 2005. Effect of suction on the mechanical behaviour of iron ore rock. *International Journal for Numerical and Analytical Methods in Geomechanics*, Vol. 29: 789-827.

Grgic, D., Giraud, A. & Schoumacker, L., 2019. Dynamic anisotropic elastic properties of a claystone under variable loading direction and saturation. *Geophysical Journal International*, Vol. 216: 148-163.

Grgic, D., Moumni, M., Giraud, A. de La Vaissière, R. & Talandier, J., 2023. Water permeability measurements by steady state and pulse decay methods on the Callovo-Oxfordian claystone and impact on mechanical properties. *Rock Mechanics and Rock Engineering*, doi: 10.1007/s00603-023-03340-0.

Hawkins AB, McConnell BJ., 1992. Sensitivity of sandstone strength and deformability to changes in moisture content. *Quarterly Journal of Engineering Geology*, 25:115–130.

Homand, F., Giraud, A., Escoffier, S., Koriche, A., & et Hoxha, D., 2004. Permeability Determination of a Deep Argillite in Saturated and Partially Saturated Conditions. *International Journal of Heat and Mass Transfer*, 47 (14): 3517-31.

Horseman, S.T., Harrington, J.F., Birchall, D.J., Noy, D.J. and Cuss, R.J., 2005. Consolidation and rebound behaviour of Opalinus Clay: a long-term, fully-drained test. *British Geological Survey Technical report No. CR/05/128*.

- Liu, Z., Shao, J., Xie, S., Conil, N. & Talandier, J., 2019. Mechanical Behavior of Claystone in Lateral Decompression Test and Thermal Effect. *Rock Mechanics and Rock Engineering*, 52 (2): 321-34.
- Liu, Z., Shao, J. & Xu., Y., 2017. Water Saturation Induced Strength Degradation of Callovo-Oxfordian Claystone. In *Bifurcation and Degradation of Geomaterials with Engineering Applications*, edited by Euripides Papamichos, Panos Papanastasiou, Elena Pasternak, et Arcady Dyskin, 11-17. Springer Series in Geomechanics and Geoengineering. Cham: Springer International Publishing.
- Masri, M., Sibai, M., Shao, J.-F. & Mainguy, M., 2014. Experimental Investigation of the Effect of Temperature on the Mechanical Behavior of Tournemire Shale. *International Journal of Rock Mechanics and Mining Sciences*, 70: 185-91.
- M’Jahad, S., 2012. Impact de la fissuration sur les propriétés de rétention d’eau et de transport de gaz des géomatériaux : Application au stockage géologique des déchets radioactifs ». Phd Thesis, Ecole Centrale de Lille (France).
- Menaceur, H., Delage, P., Tang, A.-M., Conil, N., 2015. The thermomechanical behaviour of the Callovo-Oxfordian claystone. *Int. J. Rock. Mech. Min. Sci.*, 78:290–303.
- Mohajerani, M., Delage, P., Sulem, J., Monfared, M., Tang, A. M. & Gatmiri, B., 2013. The Thermal Volume Changes of the Callovo–Oxfordian Claystone. *Rock Mechanics and Rock Engineering*, 47(1): 131-142.
- Mohajerani, M., 2011. Etude expérimentale du comportement thermo-hydro-mécanique de l’argillite du Callovo-Oxfordien. Phd Thesis, Université Paris-Est (France).
- Mohajerani, M., Delage, P., Sulem, J., Monfared, M., Tang, A. M. & Gatmiri, B., 2012. A laboratory investigation of thermally induced pore pressures in the Callovo-Oxfordian Claystone. *International Journal of Rock Mechanics and Mining Science & Geomechanics Abstracts*, 52: 112-21.
- Montes, H. G., Duplay, J., Martinez, L., Escoffier, S. & Rousset, D., 2004. Structural Modifications of Callovo-Oxfordian Argillite under Hydration/Dehydration Conditions. *Applied Clay Science*, 25 (3): 187-94.
- Pham, Q.T., Vales, F., Malinsky, L., Nguyen Minh, D., Gharbi, H., 2007. Effects of desaturation–resaturation on mudstone. *Phys Chem Earth*, 32:646–655.
- Revil, A., & Glover, P.W.J, 1998. Nature of Surface Electrical Conductivity in Natural Sands, Sandstones, and Clays. *Geophysical Research Letters*, 25 (5): 691-94.
- Robinet, J.C., Sardini, P., Siitara-Kauppi, M., Prêt, D., Yven, B., 2015. Upscaling the porosity of the Callovo-Oxfordian mudstone from the pore scale to the formation scale; insights from the 3H-PMMA autoradiography technique and SEM BSE imaging. *Sediment Geol* 321:1–10.
- Song, Yang., 2014. Water retention and fine microstructure of Bure argillite. Phd Thesis, Ecole Centrale de Lille (France).
- Valès, F., Nguyen Minh, D., Gharbi, H. & Rejeb, A., 2004. Experimental Study of the Influence of the Degree of Saturation on Physical and Mechanical Properties in Tournemire Shale (France). *Applied Clay Science, Clays in Natural and Engineered Barriers for Radioactive Waste Confinement*, 26 (1): 197-207.
- Wang, C., Gay, N., Talandier, J. & Skoczylas, F., 2022. Poroelastic experiments on COx claystone: Insight from the Biot’s coefficient measurement with water. *Engineering Geology*, 300.
- West G., 1994. Effect of suction on the strength of rock. *Quarterly Journal of Engineering Geology*. 27:51–56.
- Wright, Hervé, 2001. Rôle de la minéralogie, de la texture et de la structure dans la déformation et la rupture des argillites de l’Est, Phd Thesis, ENPC (France).

- Yang, D., Chanchole, S., Valli, P. & Chen, L., 2013. Study of the Anisotropic Properties of Argillite Under Moisture and Mechanical Loads. *Rock Mechanics and Rock Engineering*, 46: 247-57.
- Yven, B., Sammartino, S. Géraud, Y., Homand, F. & Villiéras, F., 2007. Mineralogy, texture and porosity of Callovo-Oxfordian argillites of the Meuse/Haute-Marne region (eastern Paris Basin). *Bulletin de la Société Géologique de France, Mém. Soc. géol. France*: 73-90.
- Zhang, C. L., & Rothfuchs, T., 2004. Experimental Study of the Hydro Mechanical Behaviour of the Callovo-Oxfordian Argillite. *Applied Clay Science*, 26 (1–4): 325-336.
- Zhang, C.-L., 2015. Deformation of Clay Rock under THM Conditions. *Geomechanics and Tunnelling*, 8 (5): 426-35.
- Zhang, C.-L., 2017. Examination of Effective Stress in Clay Rock. *Journal of Rock Mechanics and Geotechnical Engineering*, 9 (3): 479-89.
- Zhang, C.-L., Conil, N. & Armand, G., 2017. Thermal Effects on Clay Rocks for Deep Disposal of High-Level Radioactive Waste. *Journal of Rock Mechanics and Geotechnical Engineering*, 9 (3): 463-478.
- Zhang, C.-L., Rothfuchs, T. & Su, K., 2013. Laboratory Experiments on Thermal Effects on Clay Rocks. In book: *Thermo-Hydromechanical and Chemical Coupling in Geomaterials and Applications: Proceedings of the 3rd International Symposium GeoProc'2008*.
- Zhang, C.-L., Rothfuchs, T., Su, K. & Hoteit, N., 2007. Experimental study of the thermo-hydro-mechanical behaviour of indurated clays. *Physics and Chemistry of the Earth*, 32: 957–965.
- Zhang, W., 2021. Contribution à l'étude expérimentale du comportement mécanique des argilites du Callovo-Oxfordien : effets du chemin de chargement et de la température. PhD Thesis, Université de Lille (France).

